Brain

LRRK2 G2019S kinase activity triggers neurotoxic NSF aggregation

Journal:	*Brain*
Manuscript ID	BRAIN-2020-01856.R1
Manuscript Type:	Original Article
Date Submitted by the Author:	n/a
Complete List of Authors:	Pischedda, Francesca; Università degli Studi di Trento, Laboratory of Biology of Synapse. Center for Integrative Biology (CIBIO) Cirnaru, Daniela; Icahn School of Medicine at Mount Sinai Ponzoni, Luisa; CNR di Milano Sandre, Michele; University of Padova Department of Biomedical Sciences Biosa, Alice; University of Padova Department of Biology Perez Carrion, Maria; Universidad CEU San Pablo Facultad de Farmacia Marin, Oriano; University of Padova Department of Biomedical Sciences Morari, Michele; University of Ferrara, Department of Biomedical and Specialty Surgical Sciences Pan, Lifeng; Shanghai Institute of Organic Chemistry Greggio, Elisa; University of Padova Department of Biology Bandopadhyay, Rina; University College London Institute of Neurology Sala, Mariaelvina; CNR di Milano Piccoli, Giovanni; Università degli Studi di Trento, Laboratory of Biology of Synapse. Center for Integrative Biology (CIBIO)
Methodology:	NEUROBIOLOGY OF DISEASE
Subject area:	Neurodegeneration – cellular and molecular, MOVEMENT DISORDERS

LRRK2 G2019S kinase activity triggers neurotoxic NSF aggregation

Francesca Pischedda[1]*, Maria Daniela Cirnaru[2]*, Luisa Ponzoni[3], Michele Sandre[4], Alice Biosa[5], Maria Perez Carrion[1,6], Oriano Marin[4], Michele Morari[7], Lifeng Pan[8], Elisa Greggio[5], Rina Bandopadhyay[9], Mariaelvina Sala[3] and Giovanni Piccoli[1]#

1 CIBIO, Università degli Studi di Trento, Trento, Italy & Dulbecco Telethon Institute
2 Icahn School of Medicine at Mount Sinai, New York, USA
3 CNR, Institute of Neuroscience, Milan, Italy
4 Department of Biomedical Sciences (DSB), University of Padova, Italy
5 Department of Biology, University of Padova, Italy
6 Facultad de Farmacia, Universidad CEU San Pablo, Madrid, Spain
7 Department of Biomedical and Specialty Surgical Sciences, University of Ferrara, Italy
8 Shanghai Institute of Organic Chemistry, Shangai, China
9 Reta Lila Weston Institute of Neurological Studies and Department of Clinical and Movement Neuroscience, UCL Queen Square Institute of Neurology, London, UK

*equal contribution
corresponding author

Summary (max 150 words)

Parkinson’s disease (PD) is characterized by the progressive degeneration of dopaminergic neurons within the substantia nigra pars compacta and the presence of protein aggregates in surviving neurons. LRRK2 G2019S mutation is one of the major determinants of familial PD cases and leads to late-onset PD with pleomorphic pathology, including alpha-synuclein accumulation and deposition of protein inclusions. We demonstrated that LRRK2 phosphorylates N-ethylmaleimide sensitive factor (NSF). We observed aggregates containing NSF in basal ganglia specimens from G2019S carrier PD patients and in cellular and animal models expressing the LRRK2 G2019S variant. We found that LRRK2 G2019S kinase activity induces the accumulation of NSF in toxic aggregates. Noteworthy, the induction of autophagy cleared NSF aggregation and rescued motor and cognitive impairment observed in aged hG2019S BAC mice. We suggest that LRRK2 G2019S pathological phosphorylation impacts on NSF biochemical properties, thus causing the formation of cytotoxic protein inclusions.

Highlights

- LRRK2 phosphorylates NSF *in vivo*
- NSF aggregates in complementary LRRK2 G2019S models
- LRRK2 G2019S kinase activity induces NSF accumulation in toxic aggregates
- Autophagy induction rescues hG2019S BAC mice motor and cognitive impairment

Introduction

Parkinson's disease (PD) is a heterogeneous movement disorder characterized by the progressive degeneration of dopaminergic neurons within the Substantia Nigra pars compacta (SNpc) and the formation of Lewy bodies containing alpha-synuclein in surviving neurons [reviewed in [1]]. Mutations in LRRK2 gene (PARK8; OMIM 609007) are linked to late-onset autosomal dominant PD, accounting for up to 13% of familial PD cases compatible with dominant inheritance [2] and 1 to 2% of sporadic PD patients [3]. Clinically and pathologically, the features of LRRK2-associated parkinsonism are often indistinguishable from idiopathic PD [reviewed in [4]]. Phylogenetically the LRRK2 kinase domain belongs to the TLK (tyrosine like kinases) and shows high similarity to Mixed lineage kinases (MLKs) [5]. Like MLKs, LRRK2 is a serine/threonine kinase with no detectable tyrosine kinase activity [6]. Disease segregating mutations in LRRK2 have been reported in the kinase domain (G2019S, I2020T), the Roc domain (N1347H, R1441C/G), and in the COR domain (Y1699C) [reviewed in [7]]. However, despite its relevance in PD, the physiological function of LRRK2 and the meaning of PD-linked mutations are yet to be completely understood. The inclusions observed in PD patients may be due to the failure of the protein clearance pathways or to aberrant precipitation of protein aggregates. LRRK2 kinase activity plays a major role in LRRK2 physiological and pathological activity [reviewed in [8]]. Few LRRK2 substrates have been characterized *in vivo*, including LRRK2 itself [9] and Rab proteins [10]. In this study, we described that LRRK2 phosphorylates NSF *in vivo*. Mice expressing hLRRK2 G019S via BAC [11] present an age-dependent motor and cognitive impairment together with the deposition of NSF aggregates. At the mechanistic level, LRRK2 phosphorylation triggers the formation of NSF toxic aggregates.

Results

hG2019S mice show an age-dependent motor and cognitive impairment

Previous studies described an age-dependent neuropathological and behavioral phenotype in hG2019S BAC (hG2019S) mice [11]. We characterized age-matched wild-type and hG2019S male mice at 3, 6, 12, and 18-months in a battery of behavioral tests, including spontaneous motor activity (figure 1A-B), balance beam, pole test, rotarod (figure 1C-G) and novel object recognition (figure 1H). Spontaneous activity did not differ between genotypes. Three-months old wild-type and hG2019S cohorts performed equally in all experiments, except in the rotarod test at 32 rpm, where hG2019S mice were significantly impaired. We noticed that hG2019S mice have an impairment in the motor performance at the balance beam and pole test at 6 months, in the rotarod (12 rpm) at 12 and 18 months, in the rotarod (32 rpm) at 6 and 18 months and in the rotarod resistance at 6 and 12 months. Finally, 6, 12, and 18 months old hG2019S mice scored significantly worse at the novel object recognition test in terms of mean discrimination index. These observations suggest that 6-months old hG2019S mice show motor and cognitive impairment.

G2019S mutation correlates with the deposition of NSF aggregates

Protein aggregation is an established histological hallmark of PD. LC3 decorates LB in PD and DLB patients [12,13]. We investigated the presence of proteinaceous aggregates in specimens from substantia nigra, striatum, cortex, and hippocampus obtained from 6-month old wild-type and hG2019S male mice via staining with LC3 antibody. Interestingly, we noticed the presence of a peculiar LC3 staining pattern in nigra, cortex, and hippocampus of hG2091S mice suggesting the presence of perinuclear pale bodies (supplementary figure 1) [13,14]. It has been suggested that LRRK2 mutations promote α-synuclein aggregation [15,16]. Therefore we studied the distribution of α-synuclein in different brain areas of 6-months old wild-type and hG2019S mice. However, we did not report any overt α-synuclein deposition in the hG2019S mice brain (supplementary figure 2). LB [17] and the related intranuclear inclusion bodies [18] contain more than 90 molecules, including NSF, which we described as LRRK2 functional partner [19,20]. Consequently, we analyzed the subcellular distribution of NSF in hG2019S cortical neurons. We noticed that NSF localizes in somatic structures positive for LC3 and p62 (figure 2A-B), i.e., resembling protein aggregates [21]. Protein aggregates form high molecular weight (HMW) complexes that are retained by acetate cellulose in the filter retardation assay [22]. We confirmed the presence of NSF HMW complex in the sample prepared from 6-months hG2019S mice brain (figure 2C-D) despite a similar expression of LRRK2 and NSF in the two mice lines (supplementary figure 3A-D). A well-established feature of protein aggregates is the resistance to proteinase-K digestion [23]. Thus we characterized NSF aggregates by limited proteolysis in brain homogenates gathered from 6-months old wild-type and hG2019S mice. Upon proteinase-K digestion, the 100 kDa MW band, corresponding to full-length NSF protein, gradually disappeared in samples prepared from wild-type but not from hG2019S mice (figure 2E-F). Histological analysis revealed the presence of NSF positive aggregates in nigral, striatal, hippocampal, and cortical sections prepared from 6-months hG2019S mice (figure 2G-H). NSF aggregation resulted less evident in 12-months old hG2019S mice, suggesting the existence of compensatory mechanisms (supplementary figure 4). Next, we characterized post-mortem basal ganglia specimens obtained from healthy control, idiopathic, and G2019S PD cases. The detergent solubility profile characterizes proteinaceous aggregates from the biochemical standpoint [24]. Interestingly, while Tris-buffered saline (TBS)- soluble NSF levels were comparable among the groups (figure 3A, C), the yield of NSF in the SDS soluble fraction was higher in the sample prepared from idiopathic or G2019S PD patients (figure 3B, D). Besides, we found that NSF decorates a proportion of α-synuclein positive structure in both idiopathic and G2019S PD cases (figure 3E and table 1). To directly assess the impact of G2019S mutation on the aggregation state of NSF, we analyzed dopaminergic neurons differentiated from G2019S human neuronal precursor and their respective gene-corrected line (supplementary figure 3E-F). By filter retardation assay, we noticed that NSF forms HMW complexes in samples prepared in G2019S dopaminergic neurons (figure 3F-G). Altogether this evidence suggests that LRRK2 G2019S mutation correlates with the deposition of NSF aggregates in both murine and human models.

LRRK2 G2019S kinase activity triggers NSF aggregation

Previously we have shown that NSF is an LRRK2 substrate *in vitro* [25]. To complement this finding, we generated an antibody specifically recognizing NSF phosphorylated at Thr645 (supplementary figure 5A-B). This reagent showed that NSF phosphorylation at Thr645 increased in post-mortem samples gathered from G2019S patients specimen (figure 4A-C) and in several brain areas gathered from 6-months hG2019S mice (figure 4D-E). Structural analysis of NSF (PDB ID: 3J94) revealed that the side chain of T645 is close to the ATP-binding site on the D2 domain involved in NSF oligomerization (aa 490-744) (figure 4F-G). By differential detergent solubility assay, we noticed an increased amount of NSF in the insoluble fraction gathered from hG2019S cortical neurons (figure 4H-I) and from N2A cells overexpressing hLRRK2 G2019S (supplementary figure 5C-D). This phenomenon depends on the phosphorylation on T645, given that the co-expression of hLRRK2 G2019S did not alter the solubility profile of NSF T645A (supplementary figure 5E-F). This biochemical evidence suggests that LRRK2 G2019S triggers NSF aggregation. Proteins can aggregate upon impairment of proteasome activity [26]. Accordingly, a filter retardation assay showed that the pharmacological inhibition of the proteasome induced NSF aggregation in wild-type neurons. Instead, hG2019S neurons were characterized by a high basal amount of HMW NSF that did not further increase upon MG-132 treatment (supplementary figure 5G-H). Indeed, LRRK2 G2019S might interfere with the activity of the proteasome. However, we reported a comparable UPS proteolytic activity in 6- or 12-months old wild-type and hG2019S mice (supplementary figure 5I). Therefore, we thought that other mechanisms must underline LRRK2 G2019S dependent NSF aggregation. Phosphorylation may directly affect protein folding and oligomeric state [27]. To dissect the biological consequence of NSF phosphorylation on Thr645, we generated by site-direct mutagenesis the NSF phosphomimetic variant NSF T645D. NSF T645D has an augmented ATPase activity (supplementary figure 6A-B), it is prone to aggregation independently from UPS blockade (supplementary figure 6C-D) and it forms higher-molecular weight complexes than the wild-type variant (supplementary figure 6E-F). NSF T645D is strongly enriched in the insoluble fraction, as suggested by differential detergent solubility (figure 4J-K). Strikingly, once co-expressed with HA-NSF wild-type, NSF T645D influenced the solubility of the wild-type protein (figure 4J, L). These observations suggest that phosphorylation at T645 triggers NSF aggregation. Once entrapped within aggregates, proteins get cleaved and tagged by ubiquitin [28]. Our western-blotting analysis revealed that NSF T645D undergoes proteolytic cleavage and is strongly decorated by ubiquitin (figure 4M-O). In ubiquitin chains, each monomer can be conjugated through different lysine residues, generating a code with functional consequences [reviewed in [29]]. To determine the nature of ubiquitination occurring on the two NSF variants, we expressed in HEK293 cells NSF WT and NSF T645D together with ubiquitin wild-type or with individual ubiquitin constructs missing lysine 48, 48 and 63 or 48, 63 and 29, respectively. We noticed that the degradation and the ubiquitination of the two NSF variants depend on different lysine residues (supplementary figure 6G-K). Altogether, these data suggest that LRRK2 phosphorylation at T645 alters NSF biochemical properties and promotes its aggregation.

NSF over-expression is detrimental for hG2019S neurons in an LRRK2 kinase-dependent manner. NSF plays a crucial role in neurons [30]. To investigate whether NSF aggregation may be neurotoxic, we infected wild-type and hG2019S cortical neurons with lentiviral viruses expressing mCherry alone or together with NSF wild-type, the phospho-null variant NSF T645A or the phospho-mimetic variant NSF T645D. Neurons were treated from DIV10 to DIV14 with DMSO or GSK2578215A (GSK, 0.2 µM daily) and then processed at DIV16 (figure 5A and supplementary figure 7). Neurite retraction is an established marker of neuronal damage [31]. Our morphological analyses revealed that the over-expression of either NSF wild-type or T645A had no major effect on wild-type neuron morphology. Instead, NSF T645D was detrimental to wild-type neurons.

Noteworthy, NSF wild-type over-expression caused a significant reduction of neurite number in hG2019S neurons. Such morphological phenotype was absent in hG2019S neurons over-expressing the phospho-null NSF T645A variant (figure 5B). The analysis of neuronal viability via MTT assay confirmed this outcome (figure 5C). Interestingly, the chronic treatment with the LRRK2 kinase inhibitor GSK2578215A prevented the neurite loss of hG2019S cultures expressing wild-type NSF but did not ameliorate the overall viability. Cumulatively, these data indicate that NSF is neurotoxic upon LRRK2 phosphorylation.

Trehalose treatment clears NSF aggregates

Autophagy can attenuate protein aggregation [32]. Basal autophagy resulted similar in 6-months old wild-type and hG2019S mice (supplementary figure 8A-B). We used trehalose, a well-established autophagic inducer [33], to stimulate autophagy in wild-type and hG2019S cortical neurons (supplementary figure 8C-D). The filter retardation assay suggested that trehalose treatment reduced NSF aggregation in HEK293 cell over-expressing NSF and treated with MG132 (supplementary figure 8E-F). *In vivo*, trehalose treatment reduced NSF aggregation in 6-months old hG2019S male mice (1% in the drinking water, 1-month; supplementary figure 8G-H) without significant impact on animal weight (supplementary figure 8I). Specifically, trehalose treatment reduced the number of cells decorated by NSF in substantia nigra (figure 6), striatum (figure 7), cortex, and hippocampus (supplementary figure 9) region of hG2019S mice. Caspase-3 cleavage precedes apoptotic cell death. We noticed a significant increase of cleaved caspase-3 positive cells in nigra (figure 6) and striatum (figure 7) without any overt loss of TH density. Caspase-3 positive cells were also evident in the cortex and hippocampus (supplementary figure 9) of hG2019S mice. Trehalose treatment significantly reduced the number of caspase-3 positive cells in substantia nigra (figure 6), striatum (figure 7), cortex, and hippocampus (supplementary figure 9) of hG2019S mice. Our observations suggest that trehalose treatment cleared NSF aggregation and reduced cell death in hG2019S mice brain.

Trehalose treatment ameliorates motor and cognitive phenotype in hG2019S mice

Next, we profiled the motor and cognitive performances in 6-month old hG2019S and wild-type male mice upon chronic treatment with trehalose (figure 8). We reported a robust recovery of motor and cognitive abilities in trehalose-treated animals. In particular, trehalose treatment ameliorated the performances at the 6-mm balance beam (figure 8C), at the 32-rpm rotarod (figure 8F), the rotarod resistance at 12 rpm (figure 8G) and the novel object recognition (figure 8H). We also observed a partial improvement in motor and cognitive performances (in the rotarod 32 rpm and in the novel object recognition) in 12-month old hG2019S mice treated with trehalose starting at 10 months (1% in the drinking water, 2-month; supplementary figure 10). Altogether, these observations suggest that trehalose treatment is beneficial in rescuing behavioral defects of hG2019S mice.

Discussion

LRRK2 and the proteostatic control

In the present study, we show that hG2019S mice present an age-dependent motor and cognitive impairment together with the deposition of protein aggregates containing NSF and signs of cell death in substantia nigra, striatum, cortex, and hippocampus. Post-mortem brain investigation demonstrated that LRRK2 G2019S patients often show synucleinopathy, occasionally tauopathy, suggesting a role for LRRK2 in protein inclusion pathology [34]. The description of frontotemporal ubiquitinated neuronal intranuclear inclusions in one patient carrying G2019S substitution indicates that the LRRK2 pathological impact is not restricted to the substantia nigra [35,36].
LRRK2 kinase activity leads to protein accumulation without affecting the catalytic activity of the proteasome or expression levels of proteasomal core subcomplexes [37]. Instead, LRRK2 influences the autophagic pathways at multiple levels [reviewed in [38–40]. The investigation of *LRRK2*-deficient mice revealed a biphasic alteration of autophagy in the kidney [41,42]; however, similar studies in an independent *LRRK2*-knock out mouse line demonstrated an accumulation of secondary lysosomes in the kidney without major involvement of autophagy [43]. Our understanding of the impact of LRRK2 mutations on autophagy is still limited. Many authors conclude that G2019S mutation increases autophagy in different models, including stable cell lines [44,45], fibroblasts [46], iPS derived neurons [47], *C.Elegans* [48] and mice [49]. However, other studies have reported that the same mutation reduces [50] or at least does not affect [51,52] autophagy. Such conflicting results leave unclear the impact of LRRK2 G2019S mutation on autophagy [53]. Still, increased accumulation of protein aggregates has been reported in complementary LRRK2 G2019S models [54–57]. Thus it might be possible that LRRK2 controls protein clearance acting upstream of the two main protein-clearance mechanisms.

Phosphorylation can trigger protein aggregation

Post-translational modifications regulate protein structure. In particular, phosphorylation can dictate protein folding and eventually, aggregation state. In the context of PD, phosphorylation has a severe impact on alpha-synuclein [reviewed in [58]]. While soluble, monomeric alpha-synuclein is largely not phosphorylated in physiological conditions, up to 90% of LB-synuclein is phosphorylated on

Ser-129 [59]. It is still unresolved whether phosphorylation might trigger or impair alpha-synuclein aggregation or toxicity. While several reports claim that phosphorylation at Ser-129 favors protein aggregation [60,61] other authors described opposite or no effect [62,63]. However, phosphorylation at Ser-129 influences alpha-synuclein sub-cellular localization [64], suggesting that such PTM dictates alpha-synuclein function and fate. Similarly, hyperphosphorylated Tau protein precipitates in toxic aggregates and destabilizes the axonal tubulin cytoskeleton [65]. *In vitro* evidence shows that the phosphorylation of specific Tau residues modifies local folding, thus affecting global structure [66,67]. We showed that LRRK2 phosphorylates NSF on Thr-645 *in vitro* [25] as well as *in vivo* (here). Based on our structural analysis, the side chain of T645 falls in proximity to the ATP-binding site on NSF located on the D2 domain (aa 206-477). In particular, Thr-645 lies very close to the phosphate group of the bound ATP molecule. ATP binding on the D2 domain is essential for the formation of NSF hexamer [68]. We determined by complementary means that upon phosphorylation at Thr-645 NSF forms *bona fide* HMW aggregates, being insoluble to Triton-X100 [69], resistant to proteinase-K treatment [23] and decorated by ubiquitin and p62 [70].

Altogether, our data suggest that the phosphorylation of NSF at T645 promotes NSF oligomerization and eventually triggers its precipitation into protein inclusions. Indeed, we noticed that acute LRRK2 kinase inhibition was not efficacious in resolving NSF aggregation. Short-term LRRK2 inhibition may avoid the further precipitation of NSF proteins, but not yet clear the pre-existing aggregates. It would be useful evaluating whether long-lasting kinase inhibition can remove NSF aggregates. However, the toxicity observed *in vitro* prevented the assessment of the impact of chronic LRRK2 inhibition in primary cultures. It is unlikely that LRRK2-mediated phosphorylation is sufficient by itself to cause NSF aggregation. Actually, in idiopathic PD patients, we noticed that NSF is expressed at a high level and decorates a proportion of LB. This evidence may argue against a causative role for LRRK2 kinase activity. However, it has been recently postulated a role for LRRK2 in idiopathic PD [9]. It is tempting to speculate that in presence of increased NSF level even the low kinase activity characterizing wild-type LRRK2 may be sufficient to promote NSF aggregation. As reported for other aggregation-prone proteins like tau, it is conceivable that NSF has an intrinsic propensity towards aggregation that is pathologically exacerbated upon LRRK2 phosphorylation. Furthermore, accumulating evidence advocate a role in PD for NSF. Several linkage analyses nominate NSF as a robust risk factor for PD [71–75]. Our hypothesis is that different factors, including but not limited to increased NSF level and LRRK2 kinase activity, may trigger the pathological aggregation of NSF.

NSF aggregation, aging, and neuronal toxicity

NSF is a key component of presynaptic machinery, allowing the first step of SV recycling [76]. Numerous studies have shown that depletion of cytosolic NSF impair membrane fusion machinery [77] and results in the accumulation of intracellular vesicles [78,79]. Thus, NSF aggregation might affect presynaptic fusion machinery. Interestingly, it has been reported that experimental ischemia induces NSF aggregation into Triton-X100 insoluble inclusions that harm neuronal function via sequestering synaptic vesicle [80]. A presynaptic dysfunction might indeed explain the early-stage manifestation of PD observed in animal models [11,81,82] or presymptomatic LRRK2 G2019S carriers [83]. However, it is difficult to envisage how aberrant vesicle release could cause the overt neuronal death that characterizes the late phase of the disease. Neurons benefit from several pathways to effectively handle protein aggregation, but the ultimate resource to counteract proteinaceous stress is the degradative clearance of misfolded protein [84]. Nonetheless, the structure of the proteasome complex itself disfavours the removal of large oligomeric and aggregated proteins: substrates need to be unfolded to pass through the tight pore of the proteasome barrel [85]. Autophagy may help, being capable of handling large protein aggregates [86,87]. Unfortunately, both autophagy and proteasome activity pronouncedly decline with aging [88–90]. Thus, aging and pathological LRRK2 phosphorylation together may contribute to the deposition of NSF aggregates. Given the low stoichiometry that we reported for LRRK2-driven NSF phosphorylation *in vitro* [25], it may well be that NSF phosphorylation occurs at low rate *in vivo*. However, we noticed that T465D NSF affects the detergent solubility of the unmodified protein. Thus, we may depict a model where few phosphorylated NSF molecules lead the formation of pathological seeds capable of sequestering unphosphorylated protein into large aggregates that accumulate along with aging.

Hints towards a therapy

Altogether this evidence may call for a therapeutic strategy targeting LRRK2 kinase activity. Several brain penetrant LRRK2 selective inhibitors have been identified [reviewed in [91]]; however the broad expression of LRRK2 in other organs apart from the central nervous system, including lung, kidney and the immune system raise issues about side effects [92–97]. Presently, complementary therapeutic approaches are still needed. Targeting the protein aggregates caused by LRRK2 kinase activity may be clinically relevant. It is reasonable to predict that LRRK2 kinase activity affects the biochemical profile of other substrates besides NSF. Thus, a more holistic solution is needed. The activation of autophagy may promote the clearance of toxic protein aggregates. We report that chronic treatment with trehalose reduced NSF aggregation and ameliorated motor and cognitive phenotype in aged G2019S mice. However, it affected at a certain extent wild-type mice motor and cognitive performances. Therefore, long-lasting induction of autophagy may rise safety concerns. We deem that while in mutant mice p62 positive NSF aggregates recruits the autophagic machinery, in wild-type mice a prolonged activation of this catabolic process may self-digest proteins and organelles and eventually result in cellular toxicity. Still, treatment with trehalose already demonstrated to be protective in models of Huntington disease, spinocerebellar ataxia, Machado-Joseph disease, and Parkin-PD [98–101]. However, the pharmacokinetics properties of trehalose are poor. The small intestine, kidney, and CNS expression of trehalose catalytic enzyme, trehalase, limits its bio-availability [102]. Also, dietary trehalose results in digestive issues [103] and may enhance the virulence of common nosocomial pathogen [104]. These issues severely reduce the possibility of introducing trehalose into the clinical management of PD patients. In conclusion, boosting autophagy may be a powerful therapeutic strategy in LRRK2-PD, but a clinically relevant drug is still to be discovered.

Experimental procedures

Animals

All animal protocols were approved by the University of Trento and National Ministery of Health (IACUC 793/2016-PR). The *G2019S-LRRK2* BAC mice were previously described [11] and have been backcrossed onto the C57BL/6J mice for >10 generations.

Animals were kept in a normal light/dark cycle (12 hours light/ 12 hours dark) and had free access to food and water. All procedures involving animals were approved by Institutional agencies (OPBA- Università degli Studi di Trento) and Italian Ministry of Health (Università degli Studi di Trento prot. n. 793/2016-PR). At 5 or 10 months, Wild-type and *G2019S-LRRK2* BAC male littermates were divided into trehalose and control groups. In the trehalose group, mice were offered 1% trehalose drinking water solution. The treatment solution was changed every week. In the control group, mice were given drinking water. Mice body weight was measured every week since the start of treatment. Only male mice were used in our experiments due to a strong gender effect (Pischedda et al., manuscript in preparation).

Assays in post-mortem specimen

In total, 5 idiopathic, 4 G2019S and 5 control human brain cases were used in the study which were obtained from the archives of Queen Square Brain Bank following appropriate local ethics committee approval. Demographic details of the cases have been described previously [24]. For biochemical analysis, 5µg of TBS soluble fraction and 10µg from TBS-5% SDS fractions of basal ganglia homogenates were run on 10% Bis-tris gels with MOPS as running buffer. Details of homogenisation and fractionation procedure is mentioned in a previous publication [24]. Protein from gels were transferred onto PVDF membranes and probed with NSF (SYSY, mouse monoclonal) and beta actin (Sigma, mouse monoclonal) antibodies overnight with shaking. Following incubation with appropriate HRP conjugated secondary antibodies, blots were visualized by enhanced chemiluminescence (Pierce; UK) detection. Protein expression levels were determined by densitometry and NSF results normalised to beta-actin levels. For immunohistochemical evaluation, 8µm substantia nigra sections from control, 4 iPD and 2 G2019S-LRRK2 PD were dewaxed in xylene, and pre-treated with 95% formic acid for 10min to expose antigenic sites. Standard immunohistochemistry protocol was followed using NSF (1:200 mouse monoclonal; SY-SY) and alpha-synuclein (1: 300; rabbit polyclonal, Abcam) primary antibodies with o/n incubation at 4°C. Double immunofluorescence was performed using tetramethyl rhodamine labelled secondary antibody for alpha-synuclein and NSF with the fluorescein signal amplification kit (Perkin Elmer, UK). Following adequate washes to remove background fluorescence, sections were mounted with Aquamount (Merck, UK). Control sections where primary antibody was omitted displayed no significant background staining. Fluorescent signals from sections were scanned using Leica fluorescent microscope (Leica CTR6000). Total alpha-synuclein positive LBs were counted from each section and the proportion of NSF+ve LBs were derived. Human brains were donated to the Queen Square Brain bank for neurological disorders, UCL Queen Square Institute of Neurology and stored under a research license No:12198.

Behavioural tests

Spontaneous Motor Activity. Spontaneous motor activity was evaluated in an automated activity cage (43 cm × 43 cm × 32 cm) (Ugo Basile,Varese,Italy) placed in a sound-attenuating room as previously described [105]. Cumulative horizontal and vertical beam breaks were counted for 3 hours. *Balance Beam walking.* The beam apparatus consists of 1 meter beams with a flat surface of 12 mm or 6 mm width resting 50 cm above the table top on two poles according to [106]. A black box is placed at the end of the beam as the finish point. Nesting material from home cage is placed in the black box to attract the mouse to the finish point. A lamp (with 60 watt light bulb) is used to shine light above the start point and serves as an aversive stimulus. A video camera is set on a tripod to record the performance. On training days, each mouse crosses the 12 mm beam 3 times and then the 6 mm beam 3 times. The time required to cross to the escape box at the other end (80 cm away) is measured with a stopwatch. The stopwatch is started by the nose of the mouse entering the center 80 cm, and stopped when the animal reaches the end of the 80 cm. Once the mice are in the safe box, they are allowed some time (~15 secs) to rest there before the next trial. The mice rest for 10 min in their home cages between training sessions on the two beams. On the test day, the time to cross each beam is recorded. The beams and box are cleaned of mouse droppings and wiped with towels soaked with 70% ethanol and then water before the next mouse is placed on the apparatus.

Pole test. In the vertical pole task, the mouse was placed on a vertical wire-mesh pole with its head facing upwards. Mice were habituated to the task in 2 trials per day for 2 days. On test day (third day) mice were subjected to 5 trials: the total time taken to turn the body and to descend was recorded according to [107]. A cut-off of 60 sec was given. Data were shown as mean of 5 trials evaluated during the test day.

Rotarod. The rotarod apparatus (Ugo Basile, Biological Research Apparatus, Varese, Italy) was used to measure fore and hindlimb motor coordination and balance (Dauge et al. 2001). During the training period, each mouse was placed on the rotarod at a constant speed (12 or 32 rpm) for a maximum of 120 sec, and the latency (sec) to fall off the rotarod, within this time period, was recorded. Mice received four tests/trial each day for 4 consecutive days. The fourth test of each trial was evaluated for statistical analysis**.** The fifth day mice were submitted to Rotarod resistance at a constant speed (12 rpm) for a maximum of 30 min and the latency (sec) to fall was measured.

Novel object recognition. The novel-object recognition test was performed over a 3-day period in an open plastic arena (60 cm x 50 cm x 30 cm), as previously described [108]. Animals were habituated to the test arena for 10 min on the first day. After 1 day of habituation, the mice were exposed to familiarization (T1) and novel-object recognition (T2). During the initial familiarization stage, two identical objects were placed in the centre of the arena equidistant from the walls and from each other. Each mouse was placed in the centre of the arena between the two objects for 20 min or until it had completed 30 s of cumulative object exploration. Object recognition was scored when the animal was within 0.5 cm of an object with its nose toward the object. Exploration was not scored if a mouse reared above the object with its nose in the air or climbed on an object. Mice were returned to the home cage after familiarization and then tested again after different delays (from 5 min to 24 h later). A novel object (never seen before) took the place of one of the two familiars. Scoring of object recognition was performed in the same manner as during the familiarization phase. From mouse to mouse the role (familiar or new object) as well as the relative position of the two objects were counterbalanced and randomly permuted. The objects for mice to discriminate consisted of white plastic cylinders and coloured plastic Lego stacks of different shapes. The arena was cleaned with 70% ethanol after each trial. An experimenter blind to the genotype group manually recorded the exploration times to the objects for each animal. Total time spent exploring the two objects during T1 and T2 was also calculated.

Cell cultures

Neuron cultures were prepared from mouse cortexes obtained from embryonic day 15.5–16.5 wild-type or hG2019S mice (C57BL/6J) as previously reported [109,110]. Briefly, after brain dissection the cortexes were mechanically dissociated after 15 min incubation with 0.25% Trypsin (Euroclone) at 37 °C in agitation. The resulting cells were counted and cryopreserved or directly plated on previously poly-D-lysine (Sigma) coated wells or cover slips, according to the desired density. High density (750–1000 cells/mm2) neuron cultures were plated on 12-well plastic tissue culture plates (Iwaki; Bibby Sterilin Staffordshire, UK) and medium-density (150–200 cells/mm2) onto 12mm diameter cover slips inserted into 24-well plastic tissue culture plates (Iwaki). The cells were grown in Neurobasal at 37°C and 5% CO_2. Neuronal transfection was carried out using Lipofectamine 2000 (Life Technologies) following the manufacture's instruction. The cells were treated with LRRK2 kinase inhibitor, GSK-2578215A (Tocris Bioscience, Bristol, UK), MG132 (Tocris Bioscience, Bristol, UK) and trehalose (Sigma) by addition to culture media at the concentrations indicated through the text.

N2A (ATCC CCL-131) and HEK293 cells (ATCC CRL-1573) were cultured in DMEM complete: Dulbecco's modified Eagle's medium (DMEM, Euroclone) supplemented with 10% fetal bovine serum (FBS, Euroclone) at 37°C and 5% CO2. HEK293 were transiently transfected using linear polyethylenimine (PEI, Polysciences) with ratio DNA: PEI 0.8:100. 4 µg of DNA were dissolved in 0.5 ml of PEI solution and vortexed for 20 sec. The DNA-PEI mix was incubated for 10 minutes at room temperature (RT) and added directly to the cells. The medium was changed after 24h and the cells were lysed 48h post transfection. Lentiviruses were produced by transient transfection of HEK293T cells (ATCC CRL-3216) according to standard protocols [111]. Primary cortical cultures were transduced at DIV4 with lentiviruses at multiplicity of infection 3 (MOI3). The 3-(4,5-dimethylthiazol-2-yl)-2,5-diphenyltetrazolium bromide (MTT) assay was performed to measure culture viability as described [112]. High density (750–1000 cells/mm2) neuronal culture were infected at DIV 4 and processed for MTT assay at DIV16. Briefly, MTT ((3-(4, 5-dimethylthiazolyl-2)-2, 5-diphenyltetrazolium bromide- Sigma Aldrich) stock solution 20X (5mg/ml in MilliQ water) was diluted in neuronal complete media and cells were were incubated with MTT mix for 30 minutes at 37°C with 5% CO2. After incubation, media was discarded, cells were resuspended in DMSO to dissolve the intracellular purple precipitates and the absorbance was measured at 570 nm with the Plate reader Infinite 200 PRO (Tecan Life Sciences). Toxicity was calculated as 1- cell viability, being cell viability expressed as fold over control.

iDA culture

Wild-type, G2019S and G2019S corrected Human iPSCs derived Neuronal Precursors Cells (NPCs) were obtained from Dr. Deleidi lab and cultured as previously reported [113]. Briefly, the cells were expanded in 50:50 DMEM F12 and Neurobasal medium with: 1% P/S, 1% B27 (without Ascorbic acid), 0,5% N2, 1%L-glutamax, 150 µM Ascorbic acid, 3 µM CHIR, 0.5 µM Purmorphamine (PMA) (NPC expansion medium). Media was changed every other day and cells were passed every week after 10 min incubation with Acutase (200ul/12 well). The cells were re-plated at a 1:10 ratio in 12-well plates pre-coated with Matrigel (1:30 from Stock) in 'NPC expansion medium' supplemented with 10 µM ROCK inhibitor for the first day after splitting. After the second passage, when the cells reached 80% of confluency, the media was changed to Ventral CNS differentiation medium (50:50 DMEM F12 and Neurobasal medium with: 1% P/S, 1% B27 (without Ascorbic acid), 0,5% N2, 1% L-glutamax, 100 ng/mL FGF8, 200 µM of Ascorbic acid and 1µM PMA. When confluent the cells were split with Acutase and re-plated in Matrigel coated 6 wells plate at a 1:1 ratio. The media was changed every other day. After 10 days the Ventral CNS differentiation medium I was changed to maturation medium (50:50 DMEM F12 and Neurobasal medium with: 1% P/S, 1% B27 (without Ascorbic acid), 0,5% N2, 1%L-glutamax, 10 ng/mL BDNF, 10 ng/mL GDNF, 1ng/mL TGF-b3, 200 µM ascorbic acid, 500 µM dbcAMP and 0,5 µM PMA). After 48h the media was changed to dopaminergic differentiation medium (50:50 DMEM F12 and Neurobasal medium with: 1% P/S, 1% B27 (without Ascorbic acid), 0,5% N2, 1%L-glutamax, 10 ng/mL BDNF, 10 ng/mL GDNF, 1ng/mL TGF-b3, 200 µM ascorbic acid, 500 µM dbcAMP). The cells were kept in dopaminergic differentiation medium until the end of the experiment and the medium was changed every 2-3 days.

Statistical analysis and guidelines

All data are plotted as box, with minimum, maximum and median indicated. The normality of data distributions was determined using the D'Agostino and Pearson omnibus normality test, followed by an unpaired Student's t test, ANOVA followed by Tuckey's post-hoc test or two-way ANOVA followed by Bonferroni or Student's t post-hoc test as appropriate. The indication of number of experiment (n) and level of significance (p) are indicated throughout the text. All methods were performed in accordance with the relevant guidelines and national regulations.

Data availability

The data that support the findings of this study are available from the corresponding author, upon reasonable request.

Further methods, including immunohistochemistry, immunofluorescence, polyclonal phospho-specific NSF antibody production and purification, biochemical assays, list of expressing vectors, list of primary antibodies, and list of secondary antibodies are described in the Supplementary experimental procedures.

Author Contributions

F.P., M.D.C, L.P., M.S., A.B., and M.P.C. performed experiments. O.M., M.M., Li.P., E.G., R.B., M.E.S., and G.P. analysed data and wrote the paper.

Acknowledgments

G.P. is supported by Fondazione Telethon (grant TDPG00514TA), MIUR (PRIN-2017ENN4FY), and Fondazione Cariplo (project 2019-3415). F.P. received support by Fondazione Caritro (project 2019.0230). This work was supported by Fondazione Cariplo (grant 2011-0540) to G.P. and E.G. and Fondazione Telethon (grant GGP12237) to G.P., E.G. and M.M. G.P. is grateful to the Michael J. Fox Foundation, the FIRB program (grant RBFR08F82X_002) and Fondazione Grigioni per il morbo di Parkinson. R.B. is funded by the Reta Lila Weston Trust and the British Neuropathological Society. We gratefully thank Prof. Matthew Farrer and Dr. Heather Melrose for providing LRRK2 hG2019S BAC mice, to Marzia Indrigo for excellent technical advice and Giuseppe La Tona for support in animal handling.

Competing interests

The authors report no competing interests

References

1. Obeso JA, Stamelou M, Goetz CG, et al. Past, present, and future of Parkinson’s disease: A special essay on the 200th Anniversary of the Shaking Palsy. *Mov Disord*. 2017;32(9):1264-1310. doi:10.1002/mds.27115

2. Paisan-Ruiz C, Nath P, Washecka N, Gibbs JR, Singleton AB. Comprehensive analysis of LRRK2 in publicly available Parkinson’s disease cases and neurologically normal controls. *Hum Mutat*. 2008;29(4):485-490.

3. Taylor JP, Mata IF, Farrer MJ. LRRK2: a common pathway for parkinsonism, pathogenesis and prevention? *Trends Mol Med*. 2006;12(2):76-82.

4. Whaley NR, Uitti RJ, Dickson DW, Farrer MJ, Wszolek ZK. Clinical and pathologic features of families with LRRK2-associated Parkinson's disease. *J Neural Transm Suppl*. 2006;(70):221-229.

5. Marin I. The Parkinson disease gene LRRK2: evolutionary and structural insights. *Mol Biol Evol*. 2006;23(12):2423-2433.

6. West AB, Moore DJ, Choi C, et al. Parkinson's disease-associated mutations in LRRK2 link enhanced GTP-binding and kinase activities to neuronal toxicity. *Hum Mol Genet*. 2007;16(2):223-232.

7. Berwick DC, Heaton GR, Azeggagh S, Harvey K. LRRK2 Biology from structure to dysfunction: research progresses, but the themes remain the same. *Mol Neurodegener*. 2019;14(1):49. doi:10.1186/s13024-019-0344-2

8. Taylor M, Alessi DR. Advances in elucidating the function of leucine-rich repeat protein kinase-2 in normal cells and Parkinson's disease. *Curr Opin Cell Biol*. 2020;63:102-113. doi:10.1016/j.ceb.2020.01.001

9. Di Maio R, Hoffman EK, Rocha EM, et al. LRRK2 activation in idiopathic Parkinson's disease. *Sci Transl Med*. 2018;10(451). doi:10.1126/scitranslmed.aar5429

10. Steger M, Tonelli F, Ito G, et al. Phosphoproteomics reveals that Parkinson's disease kinase LRRK2 regulates a subset of Rab GTPases. *Elife*. 2016;5. doi:10.7554/eLife.12813

11. Melrose HL, Dächsel JC, Behrouz B, et al. Impaired dopaminergic neurotransmission and microtubule-associated protein tau alterations in human LRRK2 transgenic mice. *Neurobiol Dis*. 2010;40(3):503-517. doi:10.1016/j.nbd.2010.07.010

12. Higashi S, Moore DJ, Minegishi M, et al. Localization of MAP1-LC3 in vulnerable neurons and Lewy bodies in brains of patients with dementia with Lewy bodies. *J Neuropathol Exp Neurol*. 2011;70(4):264-280. doi:10.1097/NEN.0b013e318211c86a

13. Tanji K, Mori F, Kakita A, Takahashi H, Wakabayashi K. Alteration of autophagosomal proteins (LC3, GABARAP and GATE-16) in Lewy body disease. *Neurobiol Dis*. 2011;43(3):690-697. doi:10.1016/j.nbd.2011.05.022

14. Wakabayashi K, Tanji K, Odagiri S, Miki Y, Mori F, Takahashi H. The Lewy body in Parkinson's disease and related neurodegenerative disorders. *Mol Neurobiol*. 2013;47(2):495-508. doi:10.1007/s12035-012-8280-y

15. Cresto N, Gardier C, Gubinelli F, et al. The unlikely partnership between LRRK2 and α-synuclein in Parkinson's disease. *Eur J Neurosci*. 2019;49(3):339-363. doi:10.1111/ejn.14182

16. MacIsaac S, Quevedo Melo T, Zhang Y, Volta M, Farrer MJ, Milnerwood AJ. Neuron-autonomous susceptibility to induced synuclein aggregation is exacerbated by endogenous Lrrk2 mutations and ameliorated by Lrrk2 genetic knock-out. *Brain Commun*. 2020;2(1):fcz052. doi:10.1093/braincomms/fcz052

17. Xia Q, Liao L, Cheng D, et al. Proteomic identification of novel proteins associated with Lewy bodies. *Front Biosci*. 2008;13:3850-3856.

18. Pountney DL, Raftery MJ, Chegini F, Blumbergs PC, Gai WP. NSF, Unc-18-1, dynamin-1 and HSP90 are inclusion body components in neuronal intranuclear inclusion disease identified by anti-SUMO-1-immunocapture. *Acta Neuropathologica*. 2008;116(6):603-614. doi:10.1007/s00401-008-0437-4

19. Piccoli G, Onofri F, Cirnaru MD, et al. LRRK2 binds to neuronal vesicles through protein interactions mediated by its C-terminal WD40 domain. *Mol Cell Biol*. Published online March 31, 2014. doi:10.1128/MCB.00914-13

20. Piccoli G, Condliffe SB, Bauer M, et al. LRRK2 controls synaptic vesicle storage and mobilization within the recycling pool. *J Neurosci*. 2011;31(6):2225-2237. doi:10.1523/JNEUROSCI.3730-10.2011

21. Kopito RR. Aggresomes, inclusion bodies and protein aggregation. *Trends Cell Biol*. 2000;10(12):524-530.

22. Reid SJ, Rees MI, van Roon-Mom WMC, et al. Molecular investigation of TBP allele length: a SCA17 cellular model and population study. *Neurobiol Dis*. 2003;13(1):37-45.

23. Kheterpal I, Williams A, Murphy C, Bledsoe B, Wetzel R. Structural features of the Abeta amyloid fibril elucidated by limited proteolysis. *Biochemistry*. 2001;40(39):11757-11767.

24. Mamais A, Raja M, Manzoni C, et al. Divergent α-synuclein solubility and aggregation properties in G2019S LRRK2 Parkinson's disease brains with Lewy Body pathology compared to idiopathic cases. *Neurobiol Dis*. 2013;58:183-190. doi:10.1016/j.nbd.2013.05.017

25. Belluzzi E, Gonnelli A, Cirnaru M-D, et al. LRRK2 phosphorylates pre-synaptic N-ethylmaleimide sensitive fusion (NSF) protein enhancing its ATPase activity and SNARE complex disassembling rate. *Mol Neurodegener*. 2016;11(1):1. doi:10.1186/s13024-015-0066-z

26. Varshavsky A. The Ubiquitin System, Autophagy, and Regulated Protein Degradation. *Annu Rev Biochem*. 2017;86:123-128. doi:10.1146/annurev-biochem-061516-044859

27. Metskas LA, Rhoades E. Folding upon phosphorylation: translational regulation by a disorder-to-order transition. *Trends Biochem Sci*. 2015;40(5):243-244. doi:10.1016/j.tibs.2015.02.007

28. Olanow CW, Perl DP, DeMartino GN, McNaught KSP. Lewy-body formation is an aggresome-related process: a hypothesis. *The Lancet Neurology*. 2004;3(8):496-503. doi:10.1016/S1474-4422(04)00827-0

29. Akutsu M, Dikic I, Bremm A. Ubiquitin chain diversity at a glance. *J Cell Sci*. 2016;129(5):875-880. doi:10.1242/jcs.183954

30. Bonnycastle K, Davenport EC, Cousin MA. Presynaptic dysfunction in neurodevelopmental disorders: Insights from the synaptic vesicle life cycle. *J Neurochem*. Published online May 7, 2020. doi:10.1111/jnc.15035

31. Chernova T, Steinert JR, Guerin CJ, Nicotera P, Forsythe ID, Smith AG. Neurite Degeneration Induced by Heme Deficiency Mediated via Inhibition of NMDA Receptor-

Dependent Extracellular Signal-Regulated Kinase 1/2 Activation. *Journal of Neuroscience*. 2007;27(32):8475-8485. doi:10.1523/JNEUROSCI.0792-07.2007

32. Fujikake N, Shin M, Shimizu S. Association Between Autophagy and Neurodegenerative Diseases. *Front Neurosci*. 2018;12:255. doi:10.3389/fnins.2018.00255

33. DeBosch BJ, Heitmeier MR, Mayer AL, et al. Trehalose inhibits solute carrier 2A (SLC2A) proteins to induce autophagy and prevent hepatic steatosis. *Sci Signal*. 2016;9(416):ra21. doi:10.1126/scisignal.aac5472

34. Taymans J-M, Cookson MR. Mechanisms in dominant parkinsonism: The toxic triangle of LRRK2, alpha-synuclein, and tau. *Bioessays*. 2010;32(3):227-235. doi:10.1002/bies.200900163

35. Dächsel JC, Ross OA, Mata IF, et al. Lrrk2 G2019S substitution in frontotemporal lobar degeneration with ubiquitin-immunoreactive neuronal inclusions. *Acta Neuropathol*. 2007;113(5):601-606. doi:10.1007/s00401-006-0178-1

36. Kalia LV, Lang AE, Hazrati L-N, et al. Clinical correlations with Lewy body pathology in LRRK2-related Parkinson disease. *JAMA Neurol*. 2015;72(1):100-105. doi:10.1001/jamaneurol.2014.2704

37. Lichtenberg M, Mansilla A, Zecchini VR, Fleming A, Rubinsztein DC. The Parkinson's disease protein LRRK2 impairs proteasome substrate clearance without affecting proteasome catalytic activity. *Cell Death Dis*. 2011;2:e196. doi:10.1038/cddis.2011.81

38. Manzoni C, Lewis PA. LRRK2 and Autophagy. *Adv Neurobiol*. 2017;14:89-105. doi:10.1007/978-3-319-49969-7_5

39. Albanese F, Novello S, Morari M. Autophagy and LRRK2 in the Aging Brain. *Front Neurosci*. 2019;13:1352. doi:10.3389/fnins.2019.01352

40. Cogo S, Manzoni C, Lewis PA, Greggio E. Leucine-rich repeat kinase 2 and lysosomal dyshomeostasis in Parkinson disease. *J Neurochem*. 2020;152(3):273-283. doi:10.1111/jnc.14908

41. Tong Y, Yamaguchi H, Giaime E, et al. Loss of leucine-rich repeat kinase 2 causes impairment of protein degradation pathways, accumulation of alpha-synuclein, and apoptotic cell death in aged mice. *Proc Natl Acad Sci USA*. 2010;107(21):9879-9884. doi:10.1073/pnas.1004676107

42. Tong Y, Giaime E, Yamaguchi H, et al. Loss of leucine-rich repeat kinase 2 causes age-dependent bi-phasic alterations of the autophagy pathway. *Mol Neurodegener*. 2012;7:2. doi:10.1186/1750-1326-7-2

43. Herzig MC, Kolly C, Persohn E, et al. LRRK2 protein levels are determined by kinase function and are crucial for kidney and lung homeostasis in mice. *Hum Mol Genet*. 2011;20(21):4209-4223. doi:10.1093/hmg/ddr348

44. Gómez-Suaga P, Luzón-Toro B, Churamani D, et al. Leucine-rich repeat kinase 2 regulates autophagy through a calcium-dependent pathway involving NAADP. *Hum Mol Genet*. 2012;21(3):511-525. doi:10.1093/hmg/ddr481

45. Plowey ED, Cherra SJ, Liu Y-J, Chu CT. Role of autophagy in G2019S-LRRK2-associated neurite shortening in differentiated SH-SY5Y cells. *J Neurochem*. 2008;105(3):1048-1056. doi:10.1111/j.1471-4159.2008.05217.x

46. Yakhine-Diop SMS, Bravo-San Pedro JM, Gómez-Sánchez R, et al. G2019S LRRK2 mutant fibroblasts from Parkinson's disease patients show increased sensitivity to neurotoxin 1-methyl-4-phenylpyridinium dependent of autophagy. *Toxicology*. 2014;324C:1-9. doi:10.1016/j.tox.2014.07.001

47. Bravo-San Pedro JM, Niso-Santano M, Gómez-Sánchez R, et al. The LRRK2 G2019S mutant exacerbates basal autophagy through activation of the MEK/ERK pathway. *Cell Mol Life Sci*. 2013;70(1):121-136. doi:10.1007/s00018-012-1061-y

48. Ferree A, Guillily M, Li H, et al. Regulation of physiologic actions of LRRK2: focus on autophagy. *Neurodegener Dis*. 2012;10(1-4):238-241. doi:10.1159/000332599

49. Ramonet D, Daher JPL, Lin BM, et al. Dopaminergic Neuronal Loss, Reduced Neurite Complexity and Autophagic Abnormalities in Transgenic Mice Expressing G2019S Mutant LRRK2. *PLoS ONE*. 2011;6(4):e18568. doi:10.1371/journal.pone.0018568

50. Manzoni C, Mamais A, Dihanich S, et al. Pathogenic Parkinson's disease mutations across the functional domains of LRRK2 alter the autophagic/lysosomal response to starvation. *Biochem Biophys Res Commun*. 2013;441(4):862-866. doi:10.1016/j.bbrc.2013.10.159

51. Sánchez-Danés A, Richaud-Patin Y, Carballo-Carbajal I, et al. Disease-specific phenotypes in dopamine neurons from human iPS-based models of genetic and sporadic Parkinson's disease. *EMBO Mol Med*. 2012;4(5):380-395. doi:10.1002/emmm.201200215

52. Wauters F, Cornelissen T, Imberechts D, et al. LRRK2 mutations impair depolarization-induced mitophagy through inhibition of mitochondrial accumulation of RAB10. *Autophagy*. Published online April 4, 2019. doi:10.1080/15548627.2019.1603548

53. Manzoni C. The LRRK2-macroautophagy axis and its relevance to Parkinson's disease. *Biochem Soc Trans*. 2017;45(1):155-162. doi:10.1042/BST20160265

54. Bang Y, Kim K-S, Seol W, Choi HJ. LRRK2 interferes with aggresome formation for autophagic clearance. *Mol Cell Neurosci*. 2016;75:71-80. doi:10.1016/j.mcn.2016.06.007

55. Guerreiro PS, Gerhardt E, Lopes da Fonseca T, Bähr M, Outeiro TF, Eckermann K. LRRK2 Promotes Tau Accumulation, Aggregation and Release. *Mol Neurobiol*. 2016;53(5):3124-3135. doi:10.1007/s12035-015-9209-z

56. Novello S, Arcuri L, Dovero S, et al. G2019S LRRK2 mutation facilitates α-synuclein neuropathology in aged mice. *Neurobiol Dis*. 2018;120:21-33. doi:10.1016/j.nbd.2018.08.018

57. Schapansky J, Khasnavis S, DeAndrade MP, et al. Familial knockin mutation of LRRK2 causes lysosomal dysfunction and accumulation of endogenous insoluble α-synuclein in neurons. *Neurobiol Dis*. 2018;111:26-35. doi:10.1016/j.nbd.2017.12.005

58. Tenreiro S, Eckermann K, Outeiro TF. Protein phosphorylation in neurodegeneration: friend or foe? *Front Mol Neurosci*. 2014;7:42. doi:10.3389/fnmol.2014.00042

59. Anderson JP, Walker DE, Goldstein JM, et al. Phosphorylation of Ser-129 is the dominant pathological modification of alpha-synuclein in familial and sporadic Lewy body disease. *J Biol Chem*. 2006;281(40):29739-29752. doi:10.1074/jbc.M600933200

60. Kragh CL, Lund LB, Febbraro F, et al. Alpha-synuclein aggregation and Ser-129 phosphorylation-dependent cell death in oligodendroglial cells. *J Biol Chem*. 2009;284(15):10211-10222. doi:10.1074/jbc.M809671200

61. Wu B, Liu Q, Duan C, et al. Phosphorylation of α-synuclein upregulates tyrosine hydroxylase activity in MN9D cells. *Acta Histochem*. 2011;113(1):32-35. doi:10.1016/j.acthis.2009.07.007

62. Fiske M, Valtierra S, Solvang K, et al. Contribution of Alanine-76 and Serine Phosphorylation in α-Synuclein Membrane Association and Aggregation in Yeasts. *Parkinsons Dis*. 2011;2011:392180. doi:10.4061/2011/392180

63. Sancenon V, Lee S-A, Patrick C, et al. Suppression of α-synuclein toxicity and vesicle trafficking defects by phosphorylation at S129 in yeast depends on genetic context. *Hum Mol Genet*. 2012;21(11):2432-2449. doi:10.1093/hmg/dds058

64. Gonçalves S, Outeiro TF. Assessing the subcellular dynamics of alpha-synuclein using photoactivation microscopy. *Mol Neurobiol*. 2013;47(3):1081-1092. doi:10.1007/s12035-013-8406-x

65. Alonso AD, Cohen LS, Corbo C, et al. Hyperphosphorylation of Tau Associates With Changes in Its Function Beyond Microtubule Stability. *Front Cell Neurosci*. 2018;12:338. doi:10.3389/fncel.2018.00338

66. Bibow S, Ozenne V, Biernat J, Blackledge M, Mandelkow E, Zweckstetter M. Structural impact of proline-directed pseudophosphorylation at AT8, AT100, and PHF1 epitopes on 441-residue tau. *J Am Chem Soc*. 2011;133(40):15842-15845. doi:10.1021/ja205836j

67. Inoue M, Konno T, Tainaka K, Nakata E, Yoshida H-O, Morii T. Positional effects of phosphorylation on the stability and morphology of tau-related amyloid fibrils. *Biochemistry*. 2012;51(7):1396-1406. doi:10.1021/bi201451z

68. Whiteheart SW, Schraw T, Matveeva EA. N-ethylmaleimide sensitive factor (NSF) structure and function. *Int Rev Cytol*. 2001;207:71-112.

69. Naslavsky N, Stein R, Yanai A, Friedlander G, Taraboulos A. Characterization of detergent-insoluble complexes containing the cellular prion protein and its scrapie isoform. *J Biol Chem*. 1997;272(10):6324-6331.

70. Bjørkøy G, Lamark T, Brech A, et al. p62/SQSTM1 forms protein aggregates degraded by autophagy and has a protective effect on huntingtin-induced cell death. *J Cell Biol*. 2005;171(4):603-614. doi:10.1083/jcb.200507002

71. Simón-Sánchez J, Schulte C, Bras JM, et al. Genome-wide association study reveals genetic risk underlying Parkinson’s disease. *Nat Genet*. 2009;41(12):1308-1312. doi:10.1038/ng.487

72. Liu X, Cheng R, Verbitsky M, et al. Genome-wide association study identifies candidate genes for Parkinson's disease in an Ashkenazi Jewish population. *BMC Med Genet*. 2011;12:104. doi:10.1186/1471-2350-12-104

73. Pankratz N, Beecham GW, DeStefano AL, et al. Meta-analysis of Parkinson's disease: identification of a novel locus, RIT2. *Ann Neurol*. 2012;71(3):370-384. doi:10.1002/ana.22687

74. Cheng W-W, Zhu Q, Zhang H-Y. Identifying Risk Genes and Interpreting Pathogenesis for Parkinson's Disease by a Multiomics Analysis. *Genes (Basel)*. 2020;11(9). doi:10.3390/genes11091100

75. Nalls M, C B, Cl V, et al. Identification of novel risk loci, causal insights, and heritable risk for Parkinson's disease: a meta-analysis of genome-wide association studies. The Lancet. Neurology. doi:10.1016/S1474-4422(19)30320-5

76. Pallanck L, Ordway RW, Ramaswami M, Chi WY, Krishnan KS, Ganetzky B. Distinct roles for N-ethylmaleimide-sensitive fusion protein (NSF) suggested by the identification of a second Drosophila NSF homolog. *J Biol Chem*. 1995;270(32):18742-18744.

77. Rothman JE. Mechanisms of intracellular protein transport. *Nature*. 1994;372(6501):55-63. doi:10.1038/372055a0

78. Malhotra V, Orci L, Glick BS, Block MR, Rothman JE. Role of an N-ethylmaleimide-sensitive transport component in promoting fusion of transport vesicles with cisternae of the Golgi stack. *Cell*. 1988;54(2):221-227.

79. Mohtashami M, Stewart BA, Boulianne GL, Trimble WS. Analysis of the mutant Drosophila N-ethylmaleimide sensitive fusion-1 protein in comatose reveals molecular correlates of the behavioural paralysis. *J Neurochem*. 2001;77(5):1407-1417.

80. Liu C, Hu B. Alterations of N-ethylmaleimide-sensitive atpase following transient cerebral ischemia. *Neuroscience*. 2004;128(4):767-774. doi:10.1016/j.neuroscience.2004.07.025

81. Longo F, Mercatelli D, Novello S, et al. Age-dependent dopamine transporter dysfunction and Serine129 phospho-α-synuclein overload in G2019S LRRK2 mice. *Acta Neuropathol Commun*. 2017;5(1):22. doi:10.1186/s40478-017-0426-8

82. Sloan M, Alegre-Abarrategui J, Potgieter D, et al. LRRK2 BAC transgenic rats develop progressive, L-DOPA-responsive motor impairment, and deficits in dopamine circuit function. *Hum Mol Genet*. 2016;25(5):951-963. doi:10.1093/hmg/ddv628

83. Sossi V, de la Fuente-Fernández R, Nandhagopal R, et al. Dopamine turnover increases in asymptomatic LRRK2 mutations carriers. *Movement Disorders*. 2010;25(16):2717-2723. doi:10.1002/mds.23356

84. Rubinsztein DC. The roles of intracellular protein-degradation pathways in neurodegeneration. *Nature*. 2006;443(7113):780-786. doi:10.1038/nature05291

85. Verhoef LGGC, Lindsten K, Masucci MG, Dantuma NP. Aggregate formation inhibits proteasomal degradation of polyglutamine proteins. *Hum Mol Genet*. 2002;11(22):2689-2700.

86. Hara T, Nakamura K, Matsui M, et al. Suppression of basal autophagy in neural cells causes neurodegenerative disease in mice. *Nature*. 2006;441(7095):885-889. doi:10.1038/nature04724

87. Komatsu M, Waguri S, Chiba T, et al. Loss of autophagy in the central nervous system causes neurodegeneration in mice. *Nature*. 2006;441(7095):880-884. doi:10.1038/nature04723

88. Del Roso A, Vittorini S, Cavallini G, et al. Ageing-related changes in the in vivo function of rat liver macroautophagy and proteolysis. *Exp Gerontol*. 2003;38(5):519-527.

89. Graham SH, Liu H. Life and death in the trash heap: The ubiquitin proteasome pathway and UCHL1 in brain aging, neurodegenerative disease and cerebral Ischemia. *Ageing Res Rev*. 2017;34:30-38. doi:10.1016/j.arr.2016.09.011

90. Martinez-Vicente M, Sovak G, Cuervo AM. Protein degradation and aging. *Exp Gerontol*. 2005;40(8-9):622-633. doi:10.1016/j.exger.2005.07.005

91. Ding X, Ren F. Leucine-rich repeat kinase 2 inhibitors: a patent review (2014-present). *Expert Opin Ther Pat*. 2020;30(4):275-286. doi:10.1080/13543776.2020.1729354

92. Baptista MAS, Dave KD, Frasier MA, et al. Loss of leucine-rich repeat kinase 2 (LRRK2) in rats leads to progressive abnormal phenotypes in peripheral organs. *PLoS ONE*. 2013;8(11):e80705. doi:10.1371/journal.pone.0080705

93. Fuji RN, Flagella M, Baca M, et al. Effect of selective LRRK2 kinase inhibition on nonhuman primate lung. *Sci Transl Med*. 2015;7(273):273ra15. doi:10.1126/scitranslmed.aaa3634

94. Herzig MC, Kolly C, Persohn E, et al. LRRK2 protein levels are determined by kinase function and are crucial for kidney and lung homeostasis in mice. *Hum Mol Genet*. 2011;20(21):4209-4223. doi:10.1093/hmg/ddr348

95. Ness D, Ren Z, Gardai S, et al. Leucine-rich repeat kinase 2 (LRRK2)-deficient rats exhibit renal tubule injury and perturbations in metabolic and immunological homeostasis. *PLoS ONE*. 2013;8(6):e66164. doi:10.1371/journal.pone.0066164

96. Tong Y, Yamaguchi H, Giaime E, et al. Loss of leucine-rich repeat kinase 2 causes impairment of protein degradation pathways, accumulation of alpha-synuclein, and apoptotic cell death in aged mice. *Proc Natl Acad Sci USA*. 2010;107(21):9879-9884. doi:10.1073/pnas.1004676107

97. Baptista MAS, Merchant K, Barrett T, et al. LRRK2 inhibitors induce reversible changes in nonhuman primate lungs without measurable pulmonary deficits. *Sci Transl Med*. 2020;12(540). doi:10.1126/scitranslmed.aav0820

98. Rodríguez-Navarro JA, Rodríguez L, Casarejos MJ, et al. Trehalose ameliorates dopaminergic and tau pathology in parkin deleted/tau overexpressing mice through autophagy activation. *Neurobiol Dis*. 2010;39(3):423-438. doi:10.1016/j.nbd.2010.05.014

99. Sarkar S, Davies JE, Huang Z, Tunnacliffe A, Rubinsztein DC. Trehalose, a novel mTOR-independent autophagy enhancer, accelerates the clearance of mutant huntingtin and alpha-synuclein. *J Biol Chem*. 2007;282(8):5641-5652. doi:10.1074/jbc.M609532200

100. Seki T, Abe-Seki N, Kikawada T, et al. Effect of trehalose on the properties of mutant {gamma}PKC, which causes spinocerebellar ataxia type 14, in neuronal cell lines and cultured Purkinje cells. *J Biol Chem*. 2010;285(43):33252-33264. doi:10.1074/jbc.M110.146704

101. Zaltzman R, Elyoseph Z, Lev N, Gordon CR. Trehalose in Machado-Joseph Disease: Safety, Tolerability, and Efficacy. *Cerebellum*. Published online June 9, 2020. doi:10.1007/s12311-020-01150-6

102. Halbe L, Rami A. Trehalase localization in the cerebral cortex, hippocampus and cerebellum of mouse brains. *J Adv Res*. 2019;18:71-79. doi:10.1016/j.jare.2019.01.009

103. Montalto M, Gallo A, Ojetti V, Gasbarrini A. Fructose, trehalose and sorbitol malabsorption. *Eur Rev Med Pharmacol Sci*. 2013;17 Suppl 2:26-29.

104. Collins J, Robinson C, Danhof H, et al. Dietary trehalose enhances virulence of epidemic Clostridium difficile. *Nature*. 2018;553(7688):291-294. doi:10.1038/nature25178

105. Ferri ALM, Cavallaro M, Braida D, et al. Sox2 deficiency causes neurodegeneration and impaired neurogenesis in the adult mouse brain. *Development*. 2004;131(15):3805-3819. doi:10.1242/dev.01204

106. Luong TN, Carlisle HJ, Southwell A, Patterson PH. Assessment of motor balance and coordination in mice using the balance beam. *J Vis Exp*. 2011;(49). doi:10.3791/2376

107. Hickey MA, Kosmalska A, Enayati J, et al. Extensive early motor and non-motor behavioral deficits are followed by striatal neuronal loss in knock-in Huntington's disease mice. *Neuroscience*. 2008;157(1):280-295. doi:10.1016/j.neuroscience.2008.08.041

108. Pan D, Sciascia A, Vorhees CV, Williams MT. Progression of multiple behavioral deficits with various ages of onset in a murine model of Hurler syndrome. *Brain Res*. 2008;1188:241-253. doi:10.1016/j.brainres.2007.10.036

109. Pischedda F, Piccoli G. The IgLON Family Member Negr1 Promotes Neuronal Arborization Acting as Soluble Factor via FGFR2. *Front Mol Neurosci*. 2015;8:89. doi:10.3389/fnmol.2015.00089

110. Pischedda F, Montani C, Obergasteiger J, et al. Cryopreservation of Primary Mouse Neurons: The Benefit of Neurostore Cryoprotective Medium. *Front Cell Neurosci*. 2018;12:81. doi:10.3389/fncel.2018.00081

111. Wiznerowicz M, Trono D. Conditional suppression of cellular genes: lentivirus vector-mediated drug-inducible RNA interference. *J Virol*. 2003;77(16):8957-8961.

112. Mosmann T. Rapid colorimetric assay for cellular growth and survival: application to proliferation and cytotoxicity assays. *J Immunol Methods*. 1983;65(1-2):55-63.

113. Reinhardt P, Glatza M, Hemmer K, et al. Derivation and expansion using only small molecules of human neural progenitors for neurodegenerative disease modeling. *PLoS ONE*. 2013;8(3):e59252. doi:10.1371/journal.pone.0059252

Table 1

cases	n° α–syn + LBs	n° NSF + LBs	% of LBs + for NSF
iPD 1	16	6	37
iPD2	22	8	36
iPD3	10	4	40
iPD4	18	4	22
G2019S1	15	5	33
G2019S2	12	3	25

The table lists the number of α-synuclein positive structure (α-syn +), the number of α-synuclein and NSF positive structure (NSF +) and the relative percentage (%) in specimens prepared from substantia nigra region of 4 idiopathic (iPD) and 2 G2019S patients

Figure legends

Figure 1. hG2019S mice show age-dependent motor and cognitive impairment. Wild-type and hG2019S mice were profiled for motor and cognitive abilities at 3, 6, 12, and 18 months. 6 and 12 months-old hG2019S mice are characterized by impaired motor coordination and cognitive performance. In detail, we measured spontaneous motor activity in terms of the number of horizontal (A) and vertical (B) counts in 3 hours, time to cross a 6-mm width beam (C), time to reach the ground from the top of a vertical wire-mesh pole (D), time spent on a rotarod running at 12 rpm (E) or 32 rpm (F), total resistance on a 12 rpm running rotarod (G), and ability to recognize novel object compared to the familiar one (H); n=7-18, * $p<0.05$, ** $p<0.01$, *** $p<0.001$,**** $p<0.0001$ versus aged-matched wild-type.

Figure 2. NSF aggregation in hG2019S mice. NSF accumulates in perinuclear aggregates decorated by LC-3 (A) and p62 (B) in DIV14 cortical neurons prepared from hG2019S mice. Images are shown in pseudocolor (NSF green, LC-3 and p62 red, DAPI blue). Scale bar= 10μm. Brain samples from 6 months old wild-type or hG2019S mice were assayed by filter retardation assay to isolate the high-molecular-weight form of NSF (HMW) or by dot-blot to measure total NSF protein (C). The graph reports NSF aggregation expressed as HMW fold-over total NSF; n=8,

* $p<0.05$ versus wild-type (D). The biochemical analysis of brain homogenate shows that NSF is resistant to proteinase K degradation in samples prepared from of 6-months old hG2019S mice. The arrowhead indicates the band corresponding to full-length NSF (E). The graph indicates the amount of full-length NSF protein expressed as optical density after digestion with 0.5 μg/ml proteinase K; n=8, * $p<0.05$ versus wild-type (F). NSF accumulates in aggregates in substantia nigra and striatum (G) as well as in cortex and hippocampus (H) in 6-months hG2019S LRRK2 mice. Scale bar= 10μm.

Figure 3. NSF aggregation in human-derived samples. NSF distribution in the TBS (A) or SDS (B) soluble fraction in PD specimens. The graphs report NSF optical density in the TBS (C) or SDS (D) soluble fraction, normalized versus actin amount; n=4-5, * $p<0.05$ versus control. Post-mortem analysis of nigra specimens shows that NSF decorates α-synuclein positive Lewy bodies and Lewy neurite in G2019S PD patients. Scale bar= 10μm (E). Induced dopaminergic neurons differentiated from two independent G2019S patients (G2019S 1 and 2) as well as gene-corrected counterpart (GC 1 and 2) were assayed by filter retardation assay to isolate high-molecular-weight form of NSF (HMW) or by dot-blot to measure total NSF protein (total) (F). The graph reports NSF aggregation expressed as HMW fold-over total NSF; n=8, ** $p<0.001$ versus wild-type (G).

Figure 4. LRRK2 phosphorylation induces NSF aggregation. NSF is phosphorylated at Thr645 in G2019S PD-patients brains (A). The graphs report NSF phosphorylation at Thr645 fold-over total NSF (B) as well as NSF relative amount (C); n=4-5, * $p<0.05$. NSF is phosphorylated at Thr645 in hG2019S mice brain (D). The graph reports NSF phosphorylation at Thr645 fold-over total NSF; n=8, *, ** $p<0.05$, 0.01 versus wild-type (E). The combined ribbon, stick, and sphere representation showing the overall architecture of NSF hexamer structure from human (PDB ID: 3J94) as well as the positions of T645 and two bound ATP molecules in one NSF monomer. In this drawing, the six NSF monomers are shown in different colours, and the side chain of T645 is shown in the sphere mode and the bound ATP in the stick mode. The missing region between residue 456 and 479 in the NSF monomer is represented by a dashed pink line (F). The enlarged view of an NSF monomer (in blue) shows that the side chain of T645 is very close to the bound ATP molecule on the D2 domain (G). LRRK2 phosphorylation influences NSF aggregation. We assayed the solubility profile of NSF in samples prepared from DIV14 wild-type or hG2019S cortical neurons and treated with vehicle (DMSO) or the LRRK2 kinase inhibitor GSK2578215A (GSK, 0.2 μM, 18 hours). Short and long acquisition time of the ECL signal emitted by anti-NSF western-blot is

reported (H). The graph reports the amount of NSF present in the Triton-X100 insoluble fraction, expressed as fold-over total NSF; n=11, ** $p<0.01$ versus wild-type DMSO (I). We assayed the solubility profile of FLAG- and HA-NSF in samples prepared from HEK293 cell over-expressing wild-type or phosphomimetic T645D Strep-FLAG-NSF isoform together with HA-NSF wild-type. Strep-FLAG NSF T465D is present in the Triton-X100 insoluble fraction and sequesters HA-NSF wild-type (J). The graphs report the amount of FLAG-NSF (K) and HA-NSF (L) present in the Triton-X100 insoluble fraction, expressed as fold-over total NSF; n=8-14, * $p<0.05$, *** $p<0.001$ versus wild-type. We transfected in HEK293 cells myc-ubiquitin together with Strep-FLAG-NSF WT or T645D. We purified on streptavidin-beads NSF protein and assessed ubiquitination level by western-blotting with anti-myc antibody. The arrowheads indicate putative NSF low molecular weight fragments detected by the anti-FLAG antibody (M). The graphs report NSF ubiquitination in presence of myc-ubiquitin wild-type, calculated as anti-myc optical density normalized versus total NSF yield (N) and NSF fragmentation, expressed as the ratio of low molecular weight NSF fragments over high molecular weight NSF optical density (O); n=7, ** $p<0.01$ versus wild-type.

Figure 5. LRRK2 phosphorylation triggers NSF toxicity. Representative images of DIV14 wild-type and hG2019S cortical neurons transduced at DIV4 with mCherry expressing viruses (control) or viruses co-expressing mCherry and wild-type Strep-FLAG NSF WT, phospho-null variant T645A or phospho-mimetic variant T645D. Where indicated, cells were treated from DIV10 to DIV14 with DMSO or GSK2578215A (GSK, 0.2 μM, every two days); scale bar= 40um (A). The graph reports the number of neurites per neuron; n=14, *** $p<0.001$ versus NSF WT in wild-type neuron, °°° $p<0.001$ versus control infection in wild-type neuron, ## $p<0.01$ versus NSF WT in hG2019S neurons DMSO (B). Neuronal cultures were infected and treated as above and then processed for MTT assay at DIV14. The graph reports toxicity, calculated as 100- relative absorbance, where 100 is the mean MTT absorbance measured in not treated wild-type neurons (control) and the relative absorbance is the MTT absorbance measured in each culture folded over the control (C); n=18, ** $p<0.01$ versus NSF WT in wild-type neurons, # $p<0.01$ versus NSF WT in wild-type neurons DMSO,°° $p<0.001$ versus control infection in wild-type neuron.

Figure 6. Trehalose treatment rescues histochemical pathological hallmark of hG2019S mice in the substantia nigra. Representative micrographs of nigra sections from 6 months old wild-type and hG2019S mice treated with trehalose for 1 month, stained with anti-NSF, anti-TH, and anti-cleaved caspase-3 antibodies and counterstained with hematoxylin to visualize nuclei, scale bar = 50 μm (A). The graphs report the number of NSF aggregates (B), the TH optical density (C), and

the number of caspase-3 positive cells (D) detected in a 0.1 mm^2 area; n=6, *** $p<0.001$ versus wild-type, same treatment, $$$ $p<0.001$ versus water, same genotype.

Figure 7. Trehalose treatment rescues the histochemical pathological hallmark of hG2019S mice in the striatum. Representative micrographs of striatal sections from 6 months old wild-type and hG2019S mice treated with trehalose for 1 month, stained with anti-NSF, anti-TH, and anti-cleaved caspase-3 antibodies and counterstained with hematoxylin to visualize nuclei, scale bar = 50 µm (A). The graphs report the number of NSF aggregates (B), the TH optical density (C) and the number of caspase-3 positive cells (D) detected in a 0.1 mm^2 area; n=6, *** $p<0.001$ versus wild-type, same treatment, $$$ $p<0.001$ versus water, same genotype.

Figure 8. Trehalose treatment rescues motor and cognitive defects of hG2019S mice. Wild-type and hG2019S mice were treated starting at 5 months with trehalose (1% in drinking water) and profiled for motor and cognitive abilities at 6 months. In detail, we measured spontaneous motor activity in terms of the number of horizontal (A) and vertical (B) counts in 3 hours, time to cross a 12- and 6-mm width beam (C), time to reach the ground from the top of a vertical wire-mesh pole (D), time spent on a rotarod running at 12 rpm (E) or 32 rpm (F), total resistance on a 12 rpm running rotarod (G), and ability to recognize novel object compared to the familiar one (H); n=7-18, * $p<0.05$, ** $p<0.01$, *** $p<0.001$, **** $p<0.0001$ versus wild-type, same treatment, $ $p<0.05$, $$ $p<0.01$, $$$ $p<0.001$ versus water, same genotype.

Supplementary figure 1. hG2019S mice present proteinaceous aggregates. Wild-type and hG2019S mice were processed for imaging analysis at 6 months. Brain sections were stained with anti-LC-3 antibody and counterstained with hematoxylin to visualize nuclei. Scale bars = 50µm. We reported a peculiar LC3-immunoreactivity in the nigra, cortex, and hippocampus specimen prepared from hG2019S mice brain. The insets highlight differences in LC3 immunoreactivity in neurons (2X higher magnification). We noticed intense LC3 staining surrounding *bona fide* pale bodies (indicated by the asterisk) in nigra (e-f), striatum (k-l), cortex (q-r), and hippocampus (w-x).

Supplementary figure 2. Wild-type and hG2019S mice were processed for imaging analysis at 6 months. Brain sections were stained with anti alpha-synuclein antibody and counterstained with hematoxylin to visualize nuclei. Scale bars= 50µm.

Supplementary figure 3. We performed a biochemical analysis of cortical (Cx), hippocampal (Hi), and striatal (St) samples harvested from 6 months old wild-type and hG2019S mice brains (A). The graphs report LRRK2 phosphorylation at Ser935 fold-over total LRRK2 (B), relative LRRK2 (C), and relative NSF (D) amount; n=8. We performed a western-blot analysis to profile the maturation of G2019S or gene-corrected neural precursor cell to dopaminergic neurons. Anti-nestin antibody stains immature proliferating cells while TH mature DA-neurons. I: expansion media; II: ventral CNS neuron differentiation medium; III maturation medium; IV: differentiation medium (E). Immunofluorescence characterization of terminally differentiated NPC shows the expression of β-III-tubulin, synapsin I, and TH proteins. Scale bars = 10µm (F).

Supplementary figure 4. Wild-type and hG2019S mice were processed for imaging analysis at 12 months. Brain sections were stained with anti-NSF antibody and counterstained with hematoxylin to visualize nuclei. Scale bars = 50µm (A). We performed a biochemical analysis of brain samples harvested from 12 months old wild-type and hG2019S mice (B). The graphs report relative LRRK2 (C), and relative NSF (D) amount; n=4-6. We assessed by filter retardation assay NSF aggregation in brain specimens prepared from 12-months wild-type and hG2019S mice (E). The graph reports NSF aggregation expressed as the ratio of HMW over total NSF optical density; n=18, * $p<0.05$ versus wild-type (F). The biochemical analysis of brain homogenate shows NSF resistance to proteinase K degradation in samples prepared from of 12-months old wild-type and hG2019S mice. The arrowhead indicates the band corresponding to full-length NSF (G). The graph reports the amount of full-length NSF protein expressed as optical density after digestion with 0.5 µg/ml proteinase K; n=6 (H).

Supplementary figure 5. Validation of a polyclonal anti-P-Thr645 NSF antibody. HEK293 cells were transfected with LRRK2-G2019S and FLAG-tagged wild-type NSF protein. 48h post-transfection cells were treated with increasing doses of MLi-2 for 4 hours, then lysed and analyzed (40µg of proteins) by immunoblotting (A). HEK293 cells were transfected with FLAG-tagged wild-type NSF protein or NSF T645A or the phosphomimetics NSF T645E and T645D variant together with GFP or LRRK2-G2019S. Upon solubilization, lysates (40µg of proteins) were subjected to immunoblotting. Affinity-purified anti- P-Thr645-NSF was used for immunoblot at 1:1000 dilution (in 3% BSA in TBS-T), and in the presence of an excess (5X) of non-phosphorylated peptide antigen (KKAPPQGRKLLIIGTTSRKDVLQEME) (B). LRRK2 phosphorylation influences NSF aggregation. We assayed the solubility profile of NSF in samples prepared from N2A cell over-expressing LRRK2 K1906M or LRRK2 G2019S variants and treated with vehicle (DMSO) or the LRRK2 kinase inhibitor GSK2578215A (GSK, 2 µM, 18 hours) (C). The graph reports the amount of NSF present in the Triton-X100 insoluble fraction, expressed as fold-over total NSF; n=7, ** $p<0.01$ versus wild-type, same treatment; # $p<0.05$ versus G2019S DMSO (D). We assayed the solubility profile of NSF in samples prepared from HEK293 cell over-expressing NSF wild-type or T645A variant together with either LRRK2 K1906M or LRRK2 G2019S variants (E). The graph reports the amount of NSF present in the Triton-X100 insoluble fraction, expressed as fold-over LRRK2 K1906M condition; n=9, ** $p<0.01$ versus LRRK2 K1906M (F). NSF aggregates in hG2019S cellular models independently from the proteasome activity. Wild-type and hG2019S DIV14 cortical neurons were treated with 100nM MG-132 or vehicle (DMSO) for 48 hours and then assayed by filter retardation assay to isolate high molecular weight (HMW) form of NSF or by dot-blot to measure total NSF protein. NSF appears in HMW aggregates in wild-type neurons upon proteasome impairment and in vehicle-treated hG2019S neurons (G). The graph reports NSF aggregation expressed as HMW fold-over total NSF; n=8, *** $p<0.001$ versus wild-type, same treatment, ## $p<0.01$ versus DMSO, same genotype (H). We analyzed 20S proteasome activity in brain samples prepared from 6- or 12-months old mice. The graph reports relative fluorescence at 520-530 nm, n= 4 (I).

Supplementary figure 6. Inorganic phosphate (Pi) generated by ATP hydrolysis in the presence of NSF wild-type and T645D mutant was measured with the Malachite Green Assay at 120 min; n=3, ** $p<0.01$ Student T-test (A). Kinetic constants were obtained by data fitting with the Michaelis-Menten kinetic model $Y = Vmax*S/(Km + [S])$. Vmax NSF wild-type=3.6 µmol/min NSF T645D=4 µmol/min; Km NSF wild-type=188 µM Km NSF T645D=180 µM. Extra sum-of-squares F test was used for statistical analysis; n=3, *** $p<0.001$ (B). We analyzed HEK293 cell over-expressing Strep-FLAG-NSF wild-type or phosphomimetic T645D isoform and treated with vehicle (DMSO) or MG-132 (10 µM, 18 hours) by filter retardation assay to isolate high molecular weight (HMW) form of NSF or by dot-blot to measure total NSF protein (C). The graph reports NSF aggregation expressed as the ratio of HMW over total NSF optical density; n=5, ** $p<0.01$ versus wild-type, same treatment (D). Size exclusion chromatography fractions of HEK293 expressing ectopic Strep-FLAG-NSF wild-type or T645D alone spotted onto nitrocellulose membrane and probed with anti-flag antibody. Theoretical molecular weight are V0 at fraction 8.5, 669kDa at fraction 12, 449kDa at fraction 13 (E). The graph reports the intensity of each dot (fraction) normalized by the integrated intensities. The column void volume is 7.5 ml, n=3 (F). We transfected myc-ubiquitin wild-type, K48R, K63R, or K29/48/63 R together with Strep-FLAG-NSF WT or T645D in HEK293 cells. We purified on streptavidin-beads NSF protein and assessed ubiquitination level by western-blotting with anti-myc antibody. The arrowheads indicate putative NSF low molecular weight fragments detected by anti-FLAG antibody (G). The graphs H, J report NSF ubiquitination calculated as anti-myc optical density normalized versus total NSF wild-type (H) or T645D (J) yield and expressed as fold-over ubiquitin wild-type condition. The graphs I, K show NSF fragmentation, expressed as the ratio of low molecular weight NSF fragments over high molecular weight NSF wild-type (I) or T645D (K) optical density and folded over ubiquitin wild-type condition; n=7, * $p<0.05$, ** $p<0.01$ versus ubiquitin wild-type, one-sample T-test.

Supplementary figure 7. Wild-type and hG2019S cortical neurons were infected at DIV4 with mCherry expressing viruses or viruses co-expressing mCherry and wild-type Strep-FLAG NSF (NSF WT) or Thr645Ala Strep-FLAG NSF (NSF T645A). Cells were treated from DIV10 to DIV14 with DMSO or GSK2578215A (0.2 µM, every two days). Cells were then solubilized and processed for western-blotting to assess ectopic NSF expression, LRRK2 phosphorylation, and total LRRK2 level.

Supplementary figure 8. We evaluated basal autophagy in samples prepared from 6 months old wild-type and hG2019S mice brain (A). The graphs report LC3II/actin (left) and LC3II/LC3I ratio (right); n=5 (B). We treated DIV13 wild-type and hG2019S cortical neurons with vehicle (water) or trehalose (100 mM, 1 day) alone or in combination with NH_4Cl (5mM, 2 hours) and then processed for western blotting to evaluate the induction of autophagy, indicated by the appearance of LC3II band (C). The graph reports the LC3II/LC3I ratio; n=8, *** $p<0.001$ versus water (D). We assayed HEK293 cells over-expressing NSF wild-type and treated with vehicle (DMSO) or MG-132 (10 µM, 18 hours) alone or in combination with trehalose (100 mM, 18 hours). We measured the presence of NSF in high molecular weight aggregates (HMW) by filter retardation assay as well as total NSF expression (total) via dot-blot on a nitrocellulose membrane (E). The graph reports NSF aggregation expressed as ratio of HMW over total NSF optical density; n=8, ** $p<0.01$ versus DMSO, # $p<0.05$ versus control treatment (F). We assessed by filter retardation assay NSF aggregation in brain specimens prepared from 6-month wild-type and hG2019S mice treated with trehalose (1% in drinking water, 1 month). Trehalose treatment reduces HMW NSF forms in cortical specimens obtained from 6 months mice (G). The graph reports NSF aggregation expressed as the ratio of HMW over total NSF optical density; n=6, * $p<0.05$ versus wild-type, same treatment, ## $p<0.01$ versus water, same genotype (H). Trehalose treatment did not influence mice weight. The graph reports mice weight along with the 4 weeks treatment, n=10 (I).

Supplementary figure 9. Trehalose treatment rescues the histochemical pathological hallmark of hG2019S mice in the cortex and hippocampus. Wild-type and hG2019S mice were treated starting at 5 months with trehalose (1% in drinking water) and processed for imaging analysis at 6 months. Brain sections encompassing cortical area or hippocampus were stained with anti-NSF and anti-cleaved caspase-3 antibodies and counterstained with hematoxylin to visualize nuclei. hG2019S mice are characterized by NSF aggregation and caspase-3 cleavage in the cortex and hippocampus. Trehalose treatment reduced NSF aggregation and cleaved-caspase 3 signal (A). The graphs report number of NSF aggregates in cortex (B) and hippocampus (D) as well as the number of caspase-3 positive cells in cortex (C) and hippocampus (E) detected in a 0.1 mm^2 area; n=5, *$p<0.05$, *** $p<0.001$ versus wild-type, same treatment, $$$ $p<0.001$ versus water, same genotype.

Supplementary figure 10. Wild-type and hG2019S mice were treated starting at 10 months with trehalose (1% in drinking water) and profiled for motor and cognitive abilities at 12 months. In detail, we measured spontaneous motor activity in terms of the number of horizontal (A) and vertical (B) counts in 3 hours, time to cross a 6-mm or 12-mm width beam (C), time to reach the ground from the top of a vertical wire-mesh pole (D), time spent on rotarod running at 12 rpm (E) or 32 rpm (F), total resistance on 12 rpm running rotarod (G) and ability to recognize a novel object (H); n=7-18, * $p<0.05$, ** $p<0.01$, *** $p<0.001$,**** $p<0.0001$ versus wild-type, same treatment, $ $p<0.05$, $$$ $p<0.001$ versus water, same genotype.

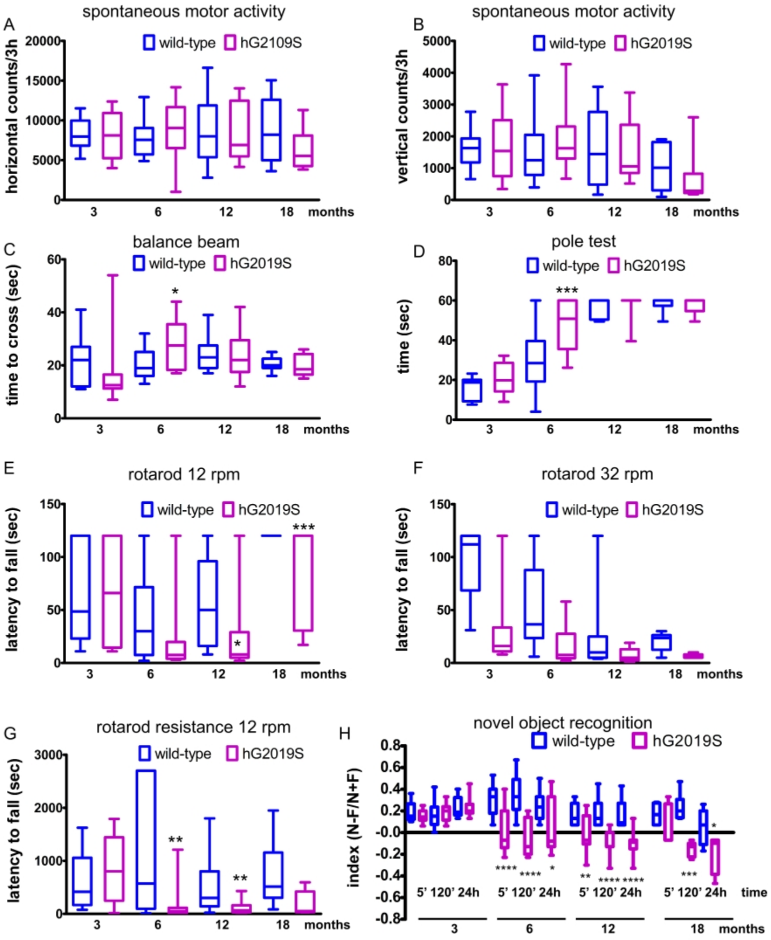

420x594mm (300 x 300 DPI)

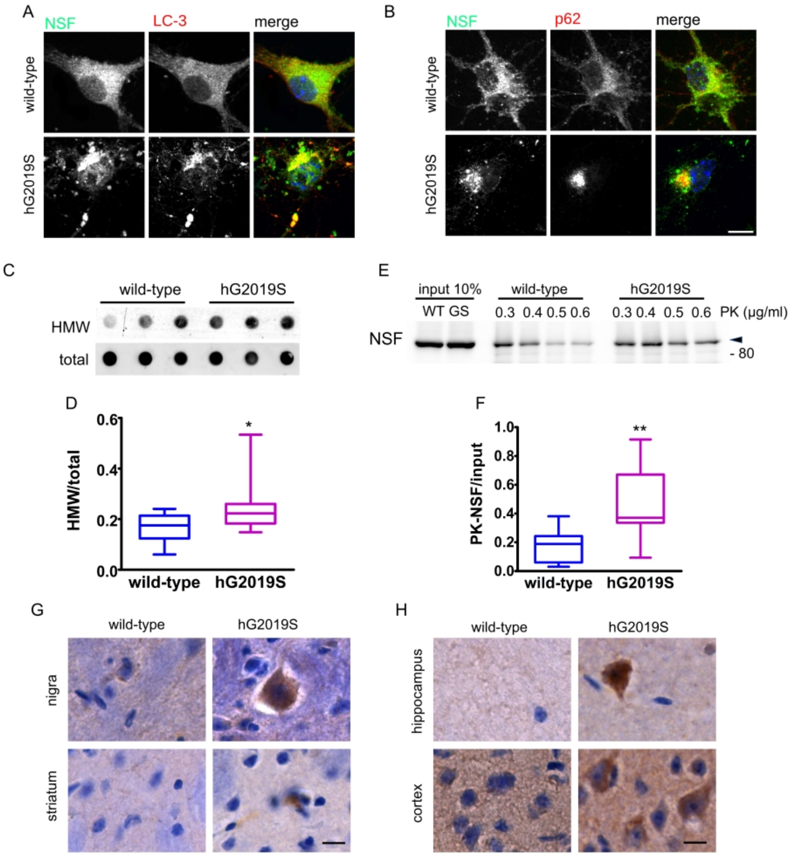

420x594mm (300 x 300 DPI)

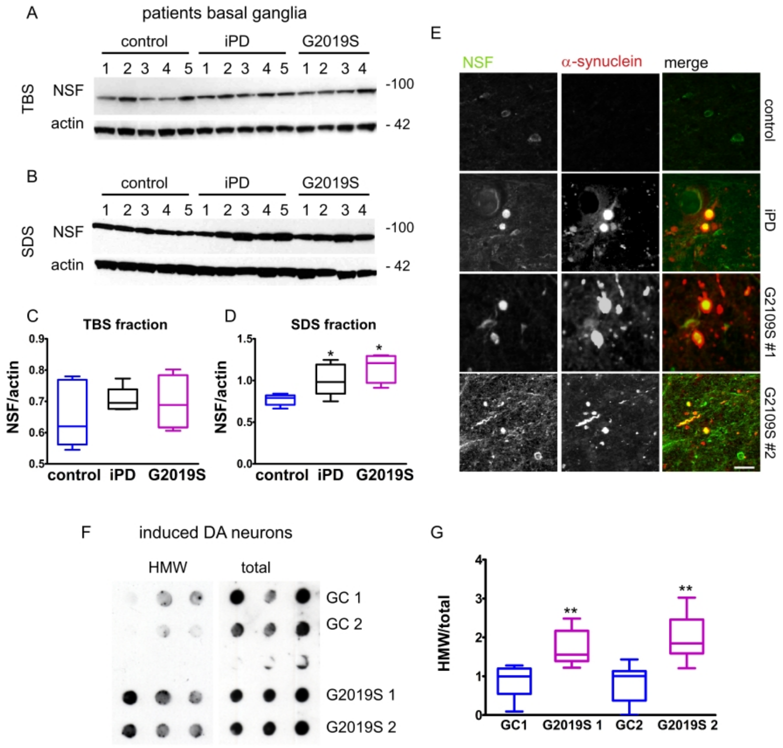

420x594mm (300 x 300 DPI)

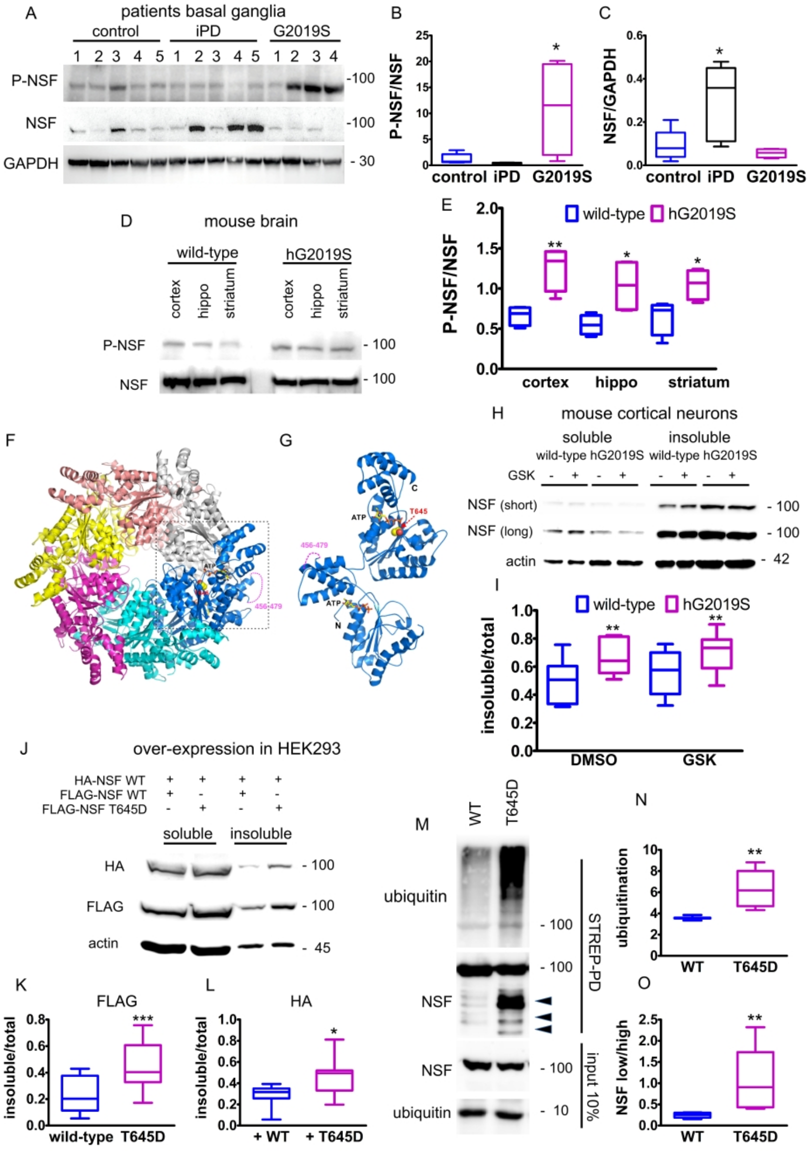

420x594mm (300 x 300 DPI)

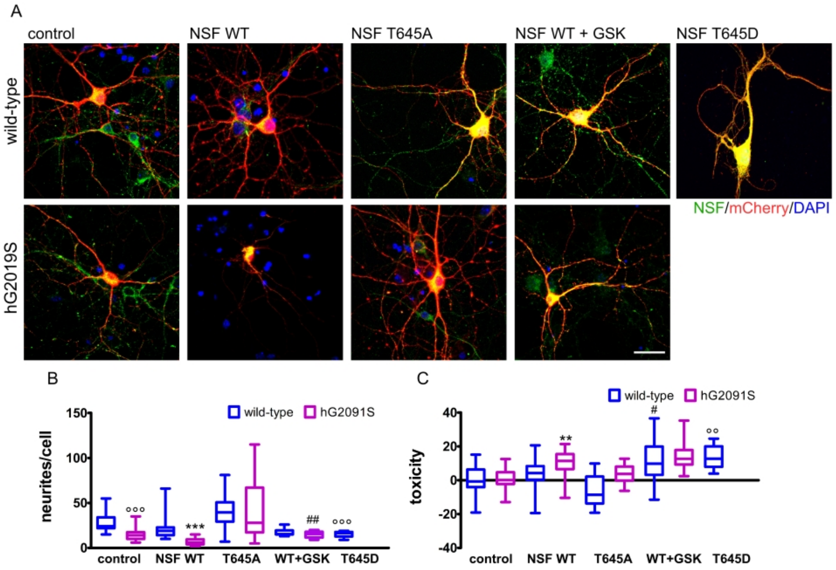

420x594mm (300 x 300 DPI)

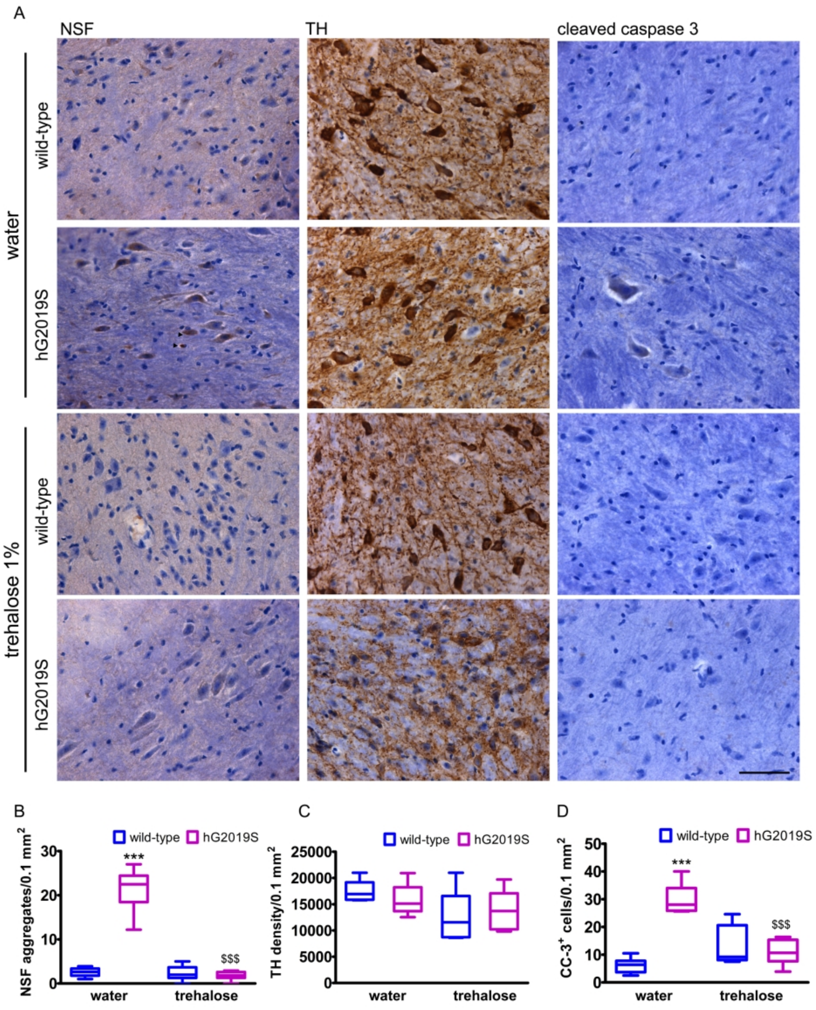

209x297mm (300 x 300 DPI)

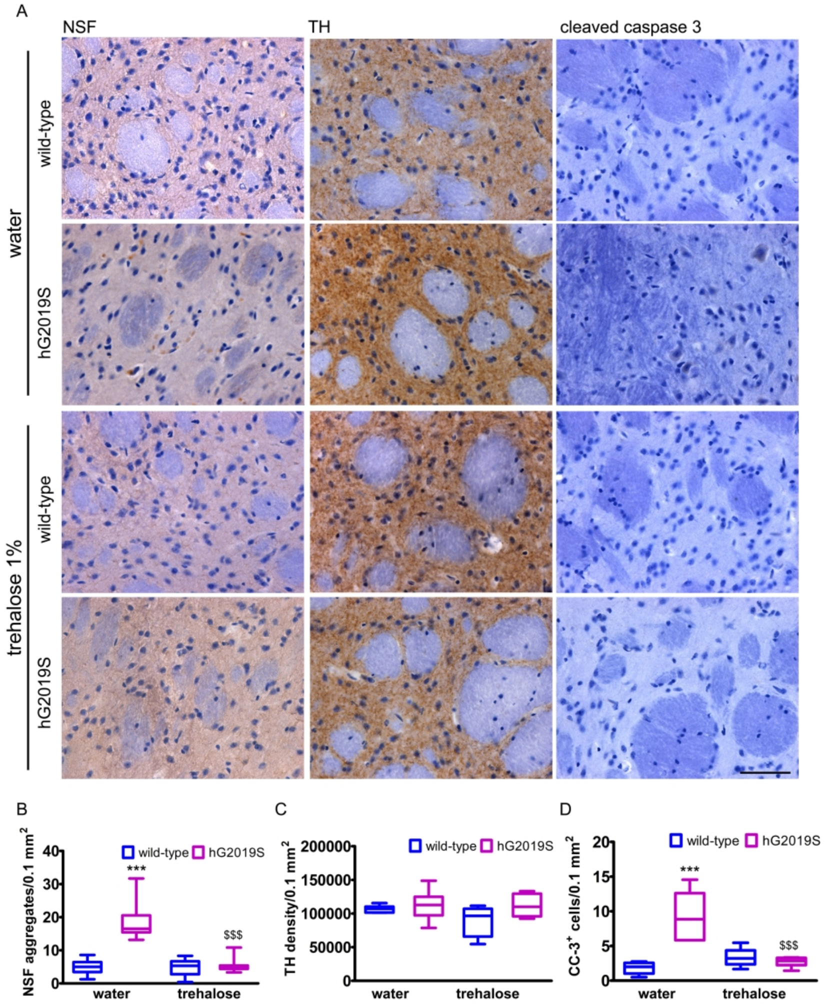

209x297mm (300 x 300 DPI)

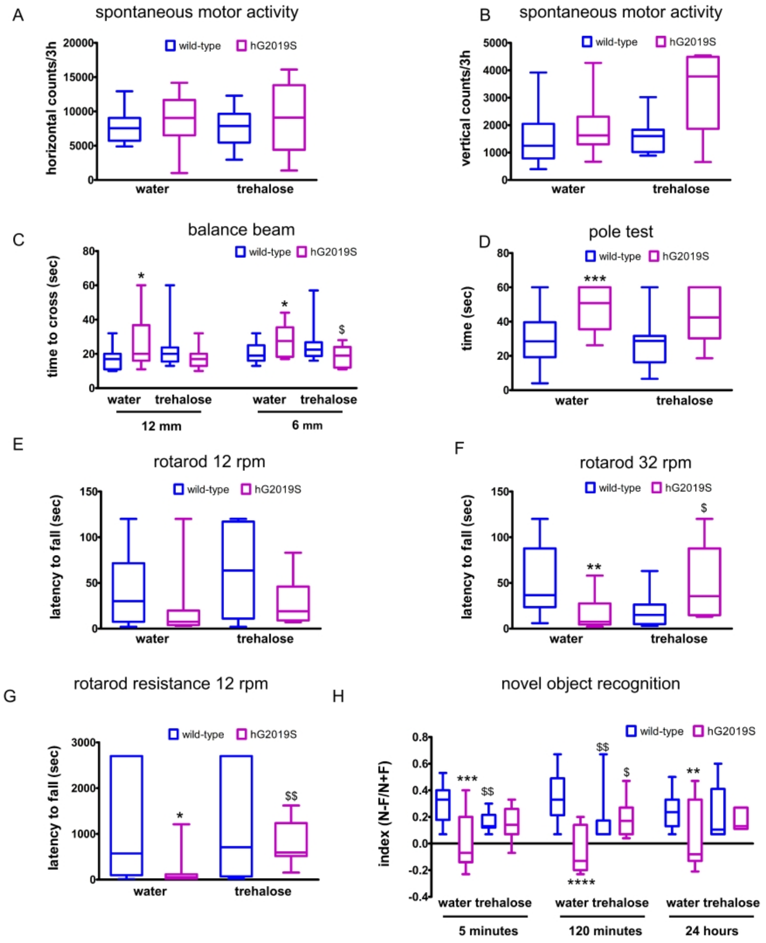

420x594mm (300 x 300 DPI)

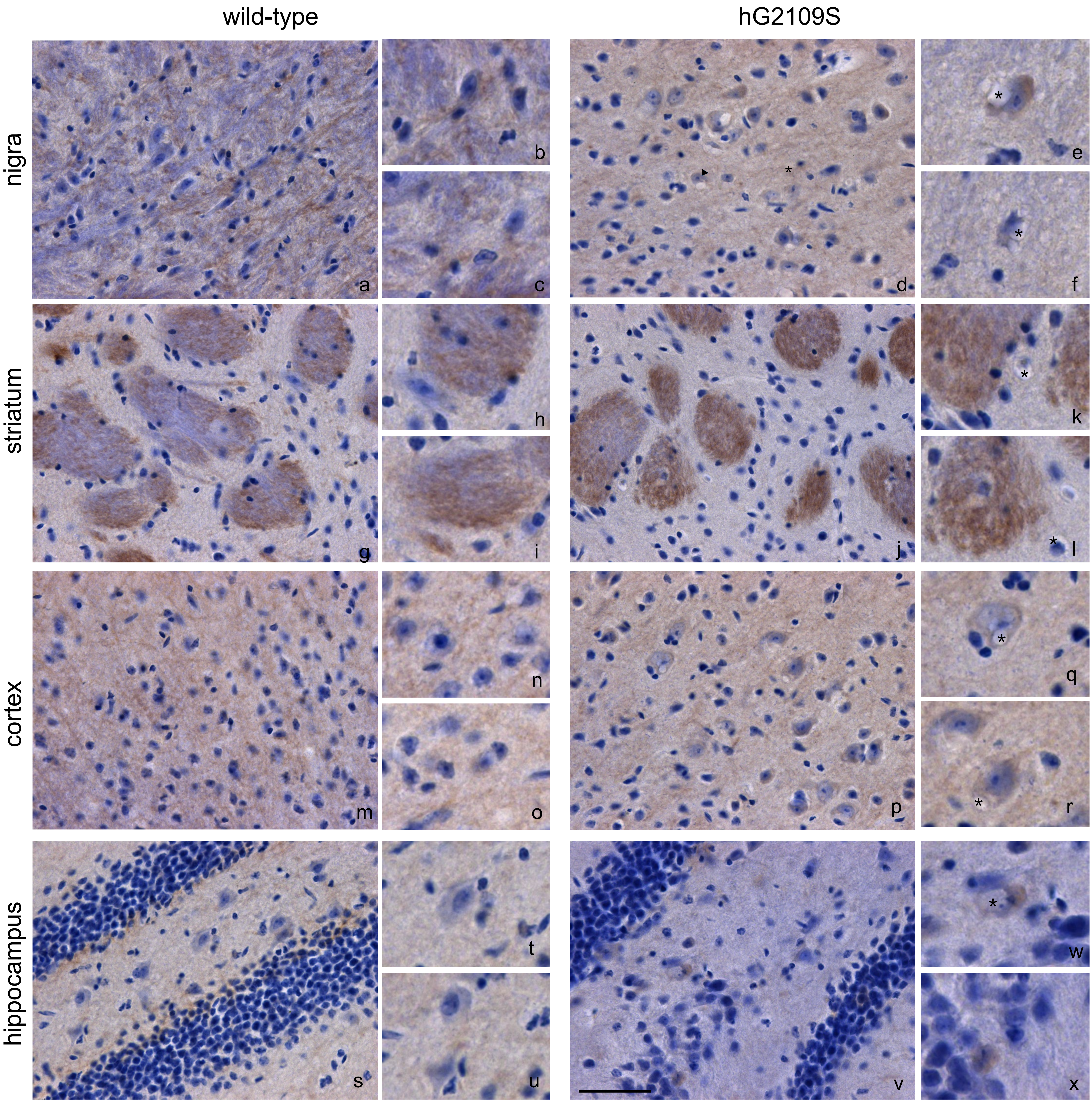

Supplementary figure 1

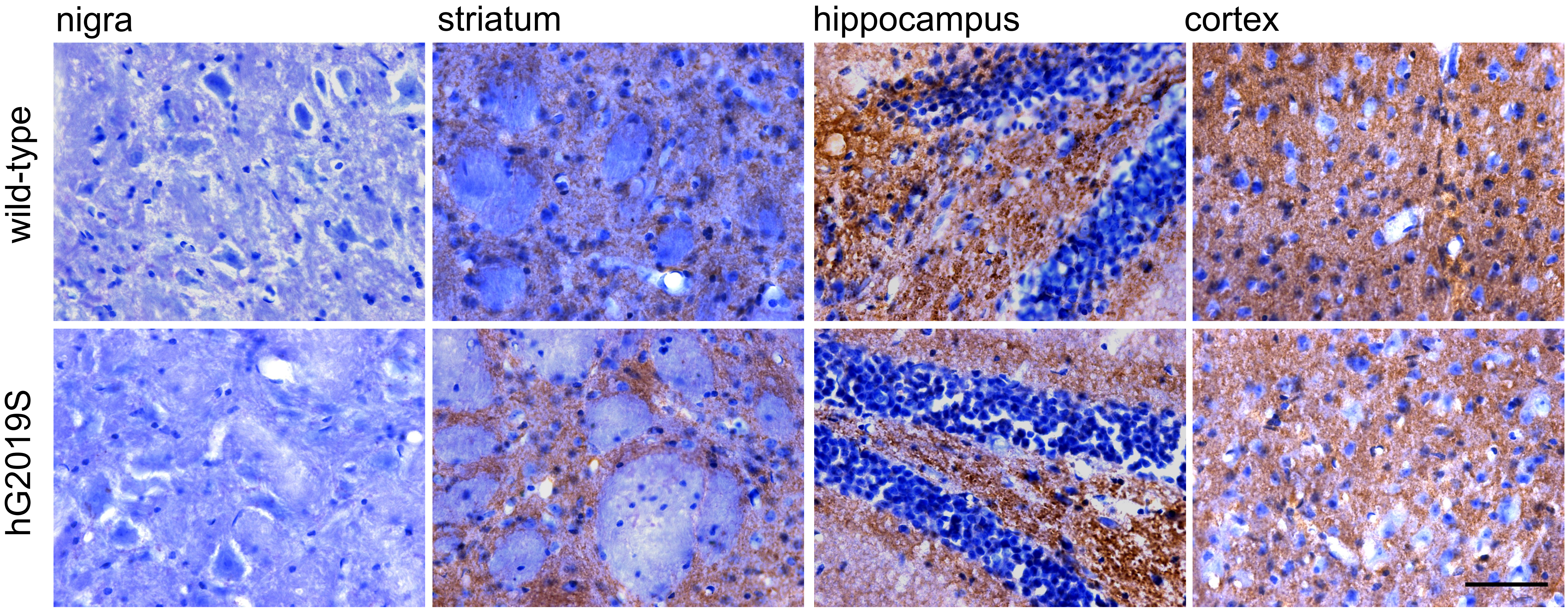

Supplementary figure 2

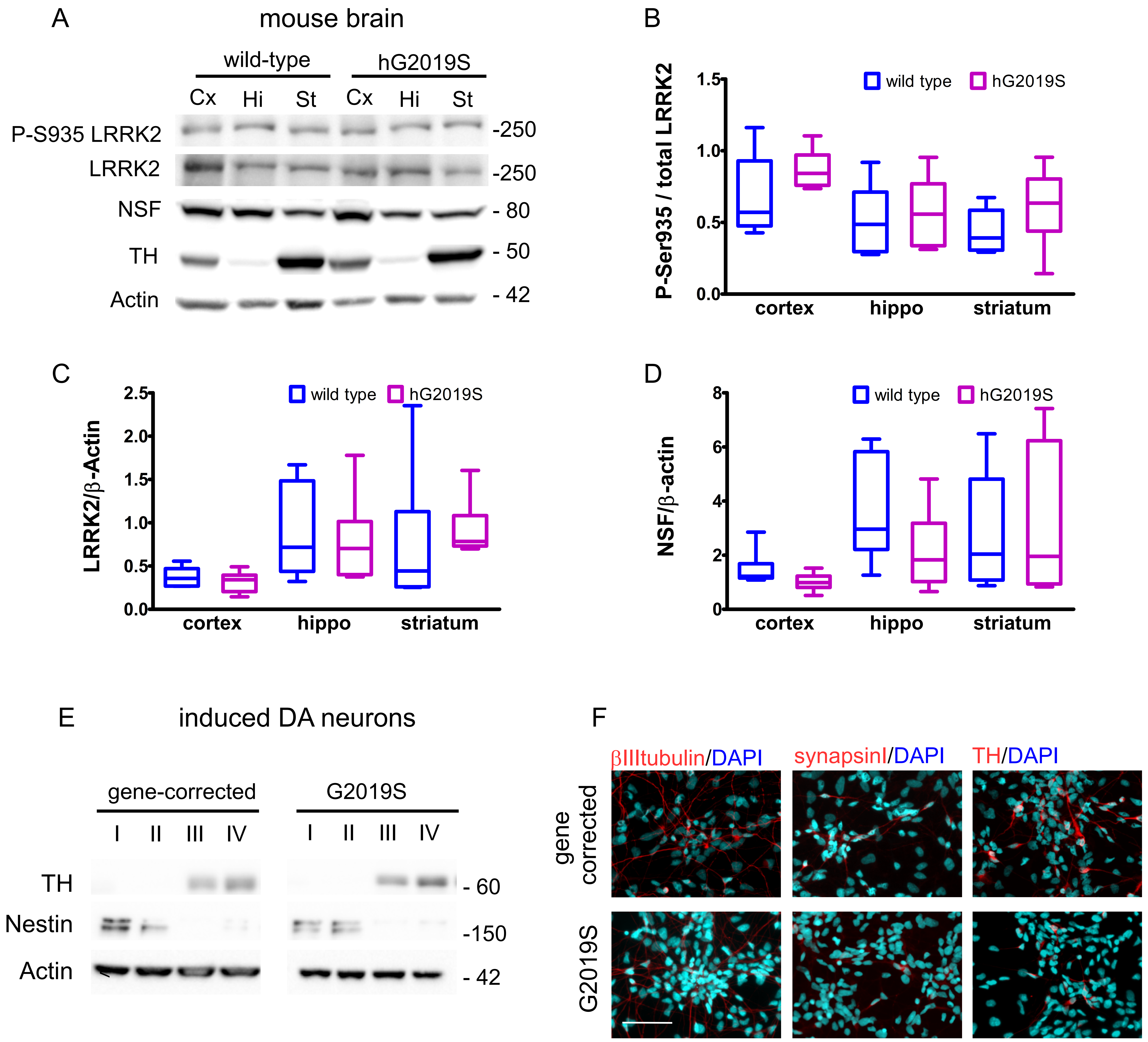

Supplementary figure 3

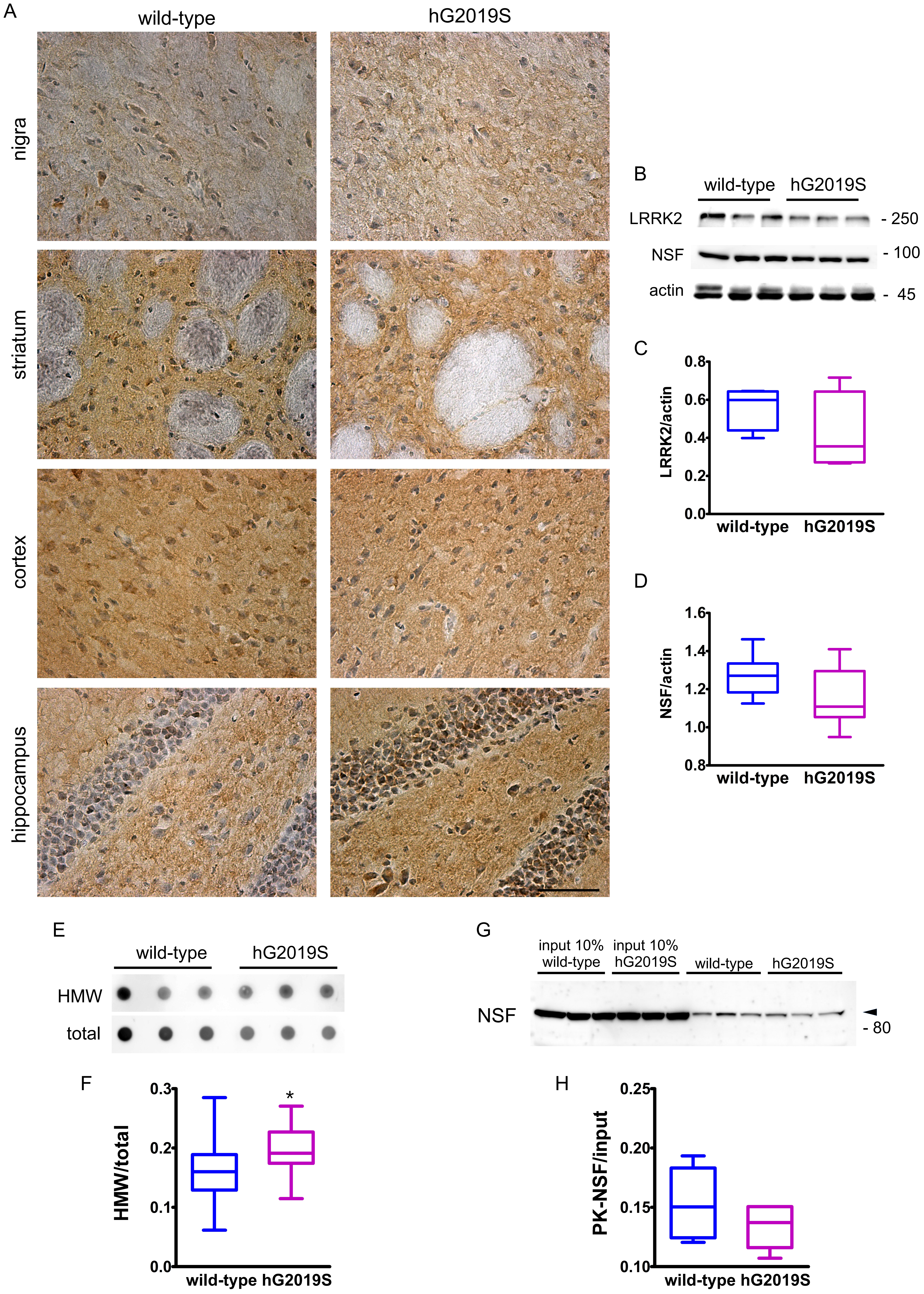

Supplementary figure 4

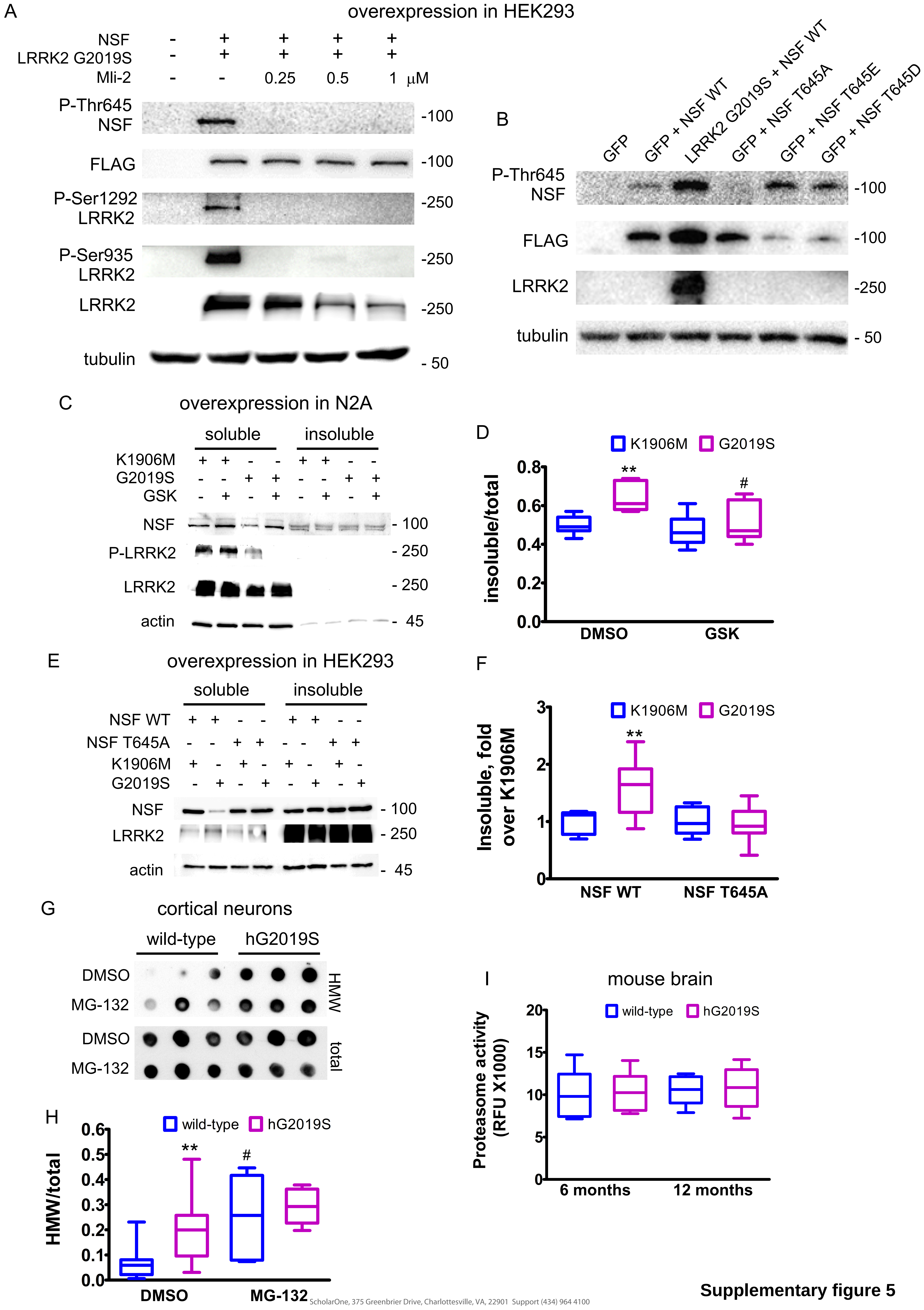

Supplementary figure 5

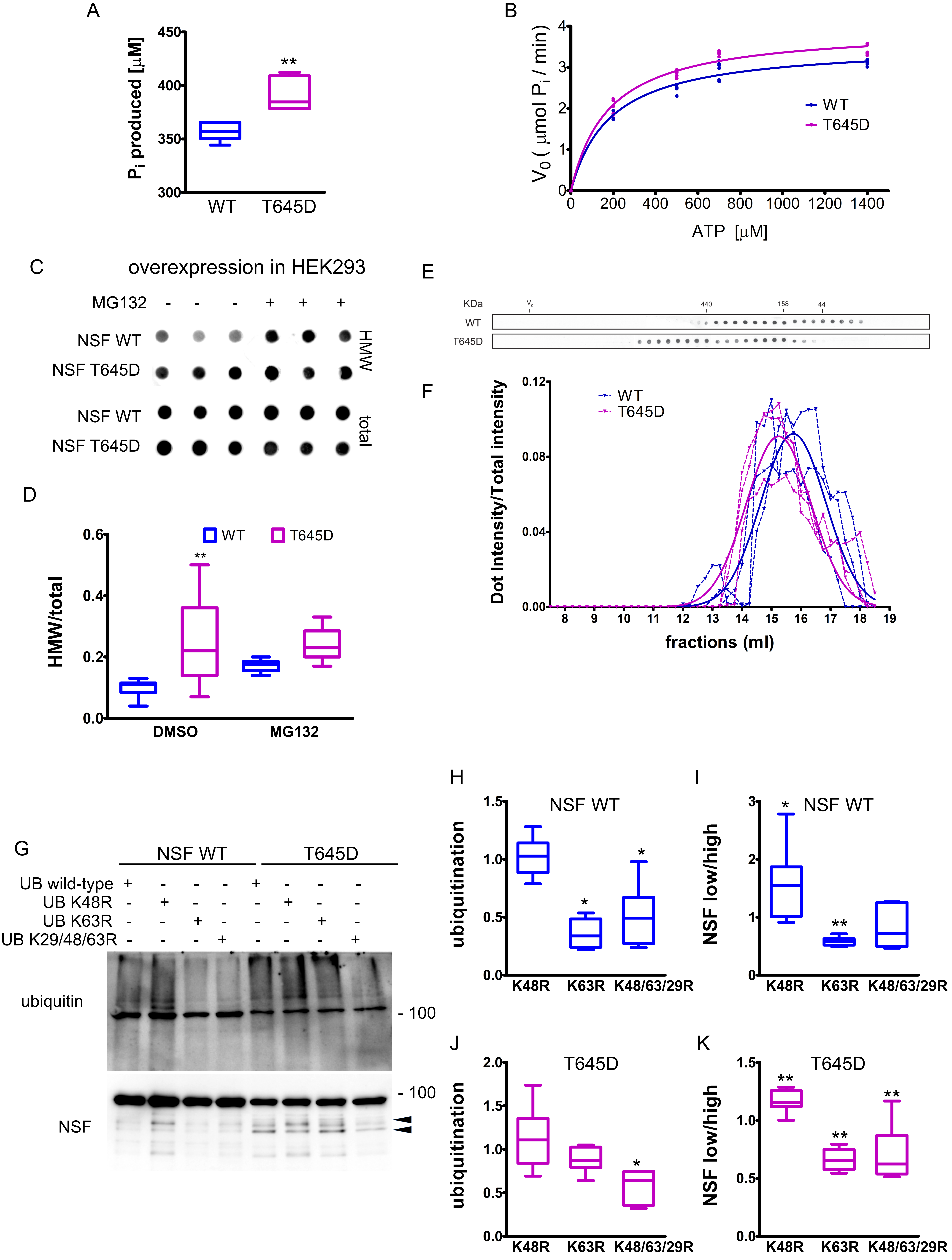

Supplementary figure 6

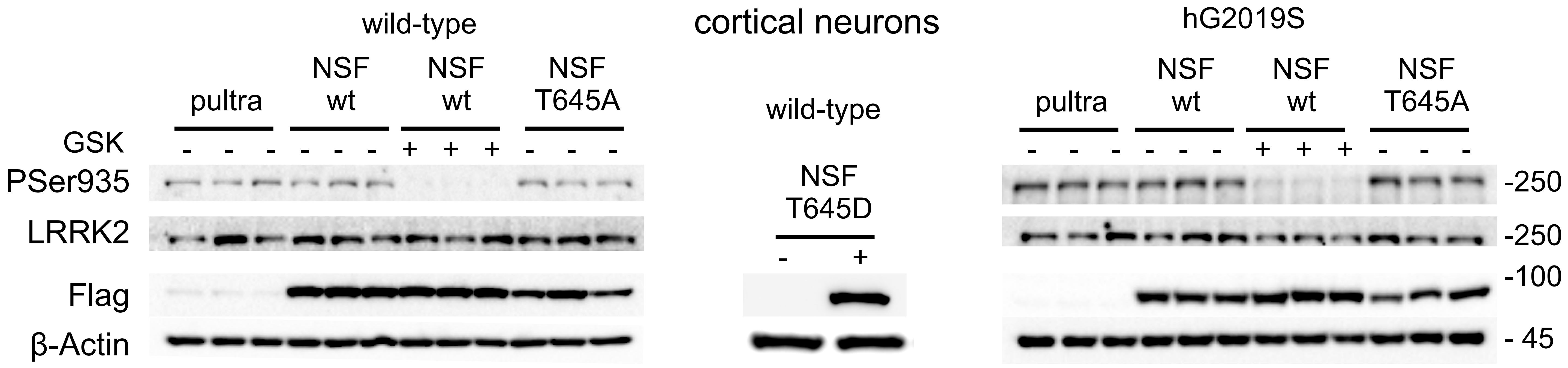

Supplementary figure 7

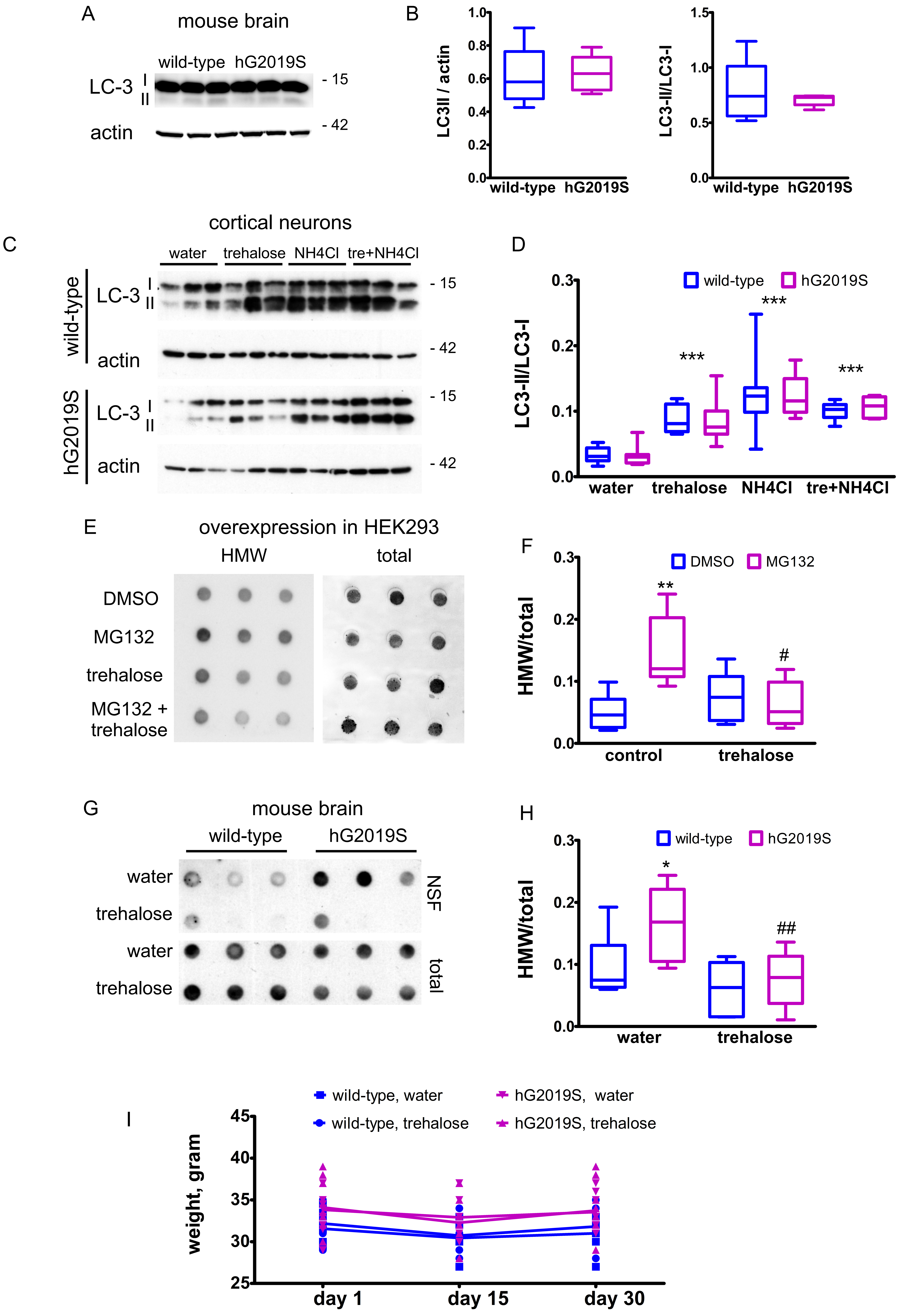

Supplementary figure 8

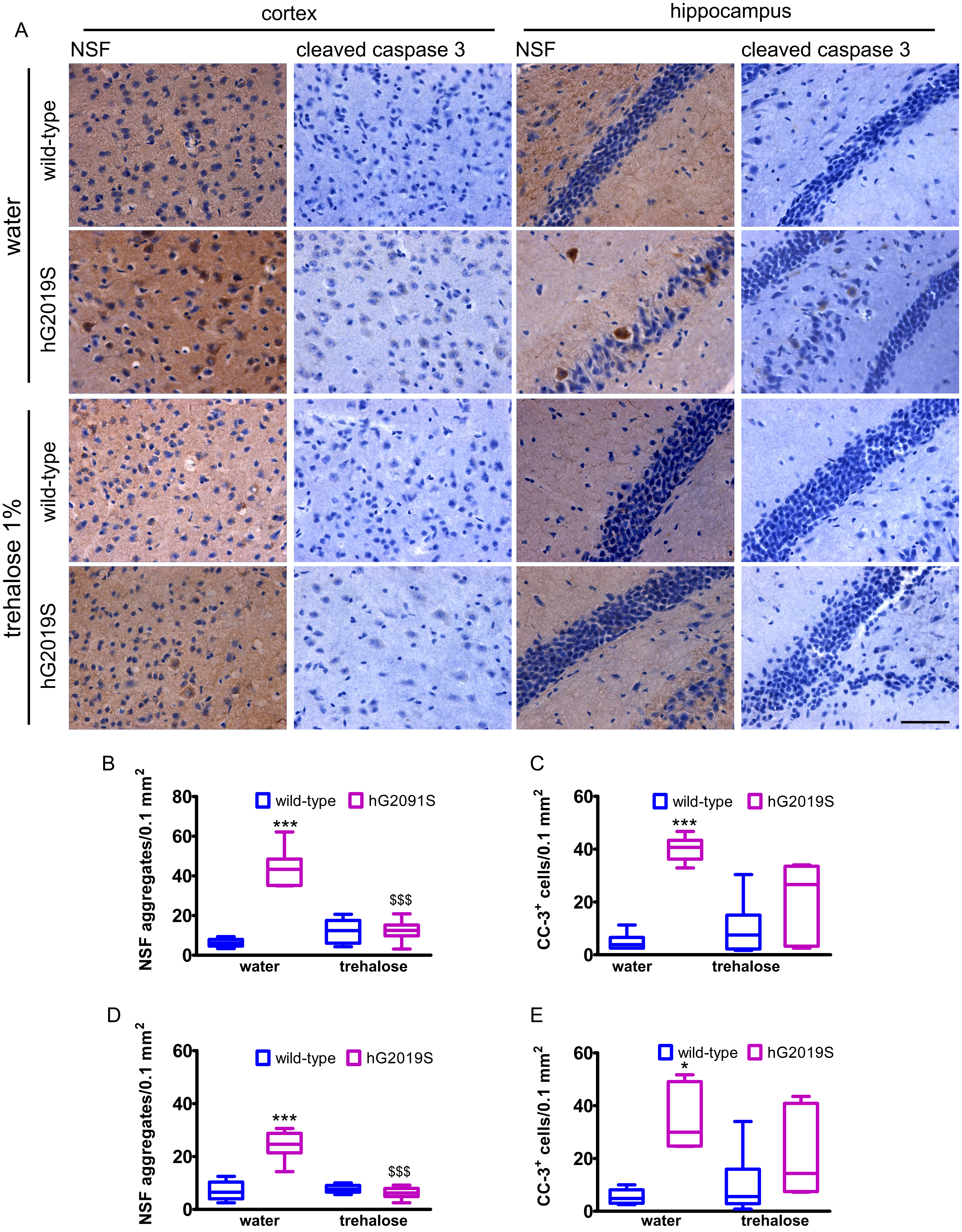

Supplementary figure 9

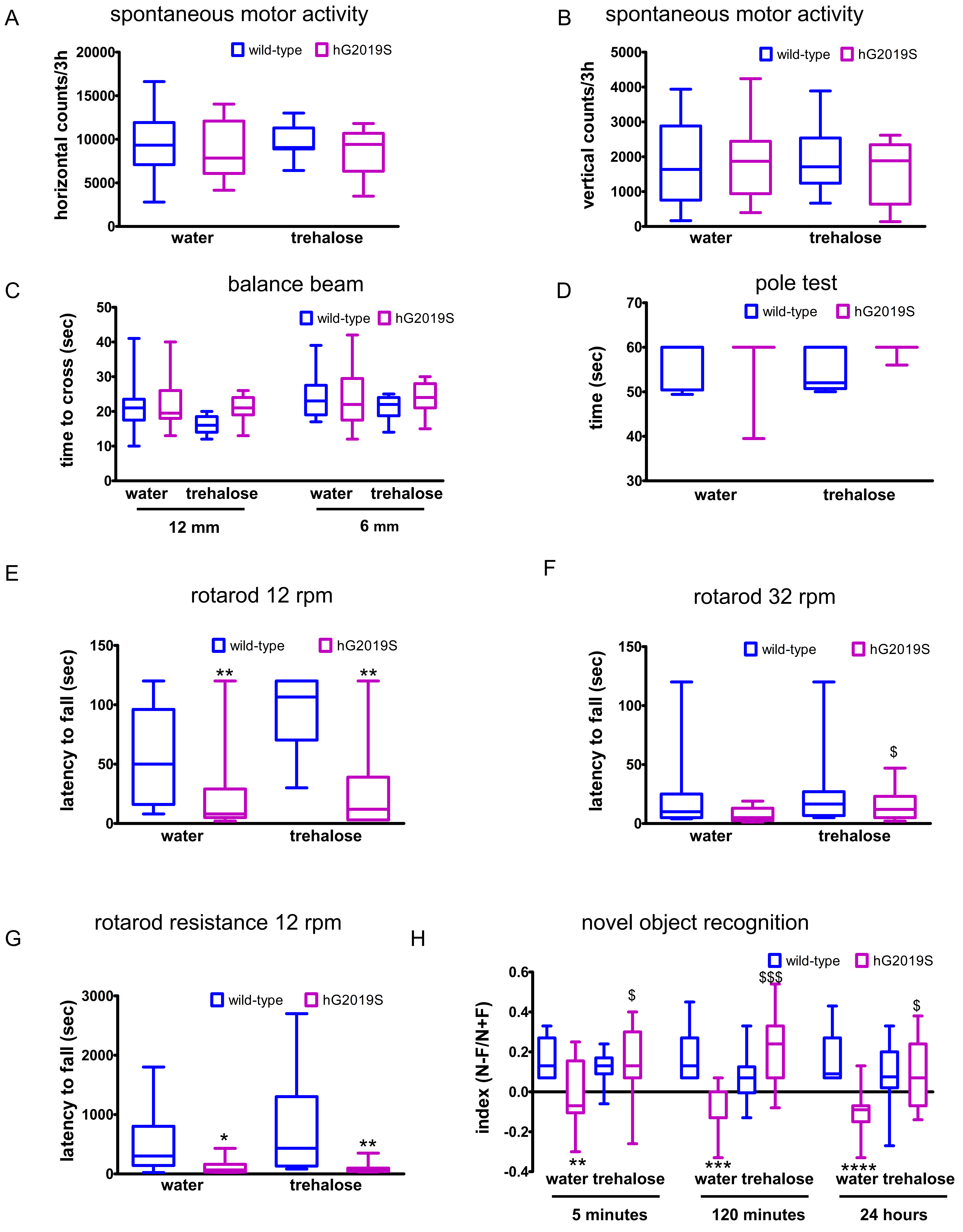

Supplementary figure 10

Supplementary experimental procedures

Immunohistochemistry

Six and 12 months old mice were anaesthetized and transcardially perfused with PBS 1X followed by 4% paraformaldehyde in PBS 1X. Brains were dissected, postfixed for 2h by immersion in the same fixative and then cryoprotected by immersion in 30% sucrose solution in PBS 1X for 24 h at 4°C. Brains were included in OCT and stored at -80°C until processing. 14 µm brain coronal sections were obtained after serial sectioning on Leica cryostat and mounted on Polysine Slides (Thermo Fischer Scientific). The slices were saturated in 2,5% BSA, 10% NGS, 0,2% Triton X-100, PBS 1X, for 1 hour at RT and incubated with the primary antibody O/N at 4°C. After 3 washes in PBS 1X – 0,2% Triton X-100 the sections were quenched for 15 min in PBS 1X plus 0,3% H_2O_2at RT, then washed with PBS 1X. The sections were incubated for 30 min with the secondary biotinylated antibody at RT. The slices were then rinsed in PBS1X and incubated for 30 minutes with Vectastain ABC kit 1:1 mix (Vectorlab), washed 2 times in PBS 1X – 0.2% Triton X-100, washed once in PBS1X, and developed with DAB quanto mix (Thermo Scientific) for 30 sec. The stained sections were rinsed in PBS 1X stained in Hematoxylin solution, Gill No.2 (Sigma Aldrich) for 2,5 minutes and then washed for 2 minutes with tap water. Sections were incubated with differentiation solution (70% ETOH plus 0,3% HCl) for 10 seconds, washed with tap water and then incubated for 30 seconds with Scott's Tap water Substitute (Sigma Aldrich) for blueing. Sections were then dehydrated, mounted using DPC mounting reagent (Sigma) and kept at RT until acquisition with a Zeiss Axio Imager M2 equipped with 40X objective.

Immunofluorescence

For the immunostaining experiments, neurons were fixed in 4% paraformaldehyde and 4% sucrose at room temperature or 100% methanol at -20°C. mCherry positive neurons were randomly chosen for quantification in at least four independent experiments for each condition. Cover slips were mounted with prolonged reagent (Life Technologies) and observed with Zeiss Observer Z1 microscope equipped with an Apotome module. The obtained images provide an axial resolution comparable to confocal microscopy[1,2]. Images were acquired with AxioObserv Z1 microscope equipped with Apotome module using a plan-Apochromat 63x/1.40 Oil objective, pixel size 0,102 mm x 0.102 mm. Acquired images were analyzed with ImageJ software using NeuronJ plugin [3].

Polyclonal phospho-specific NSF antibody production and purification

Affinity-purified anti-P-Thr645-NSF polyclonal antibody was made in a NZW female rabbit (Envigo) by immunization against a single peptide (amino acids 631–656:

KKAPPQGRKLLIIGpTTSRKDVLQEME), encompassing the LRRK2 phosphorylation site of NSF, conjugated via an N-terminal Cys residue to maleimide-activated KLH (keyhole limpet haemocyanin, Sigma-Aldrich). Rabbit was injected subcutaneously four times at 3-week intervals, with 0.5 mg of phosphopeptide-protein conjugates in PBS emulsified with Freund's adjuvant (1:1 v/v). After the last immunization, blood was collected and antisera was purified using an immobilized peptide affinity resin (Sulfo Link Coupling Gel, Thermo) according to manufacturer's instructions. Briefly, a shorter peptide (LIIGpTTSRKD) was conjugated via an N-terminal Cys residue and coupled to the resin. Fractions were eluted with Glycine Buffer (0.2 M, pH 2.5) into Tris buffer (1 M, pH 8.5) solution for pH neutralization. Protein eluted fractions (as determined by Abs at 280 nm) were pooled and concentrated by ultrafiltration (Amicon Ultra-15 30KD, Millipore). All synthetic peptides were synthesized, purified by RP-HPLC, and confirmed by mass spectroscopy at CRIBI (University of Padova) as previously described [4]. All animal protocols were approved by the University of Padova and National Ministery of Health (IACUC 906/2016-PR).

Biochemical assays

Proteinase K digestion. Proteinase K digestion of mouse brain lysates was performed on samples prepared from 6 months mouse LRRK2 wild-type and LRRK2 G2019S brains. Brains were solubilized by mechanical homogenization of 1g of tissue in lysis buffer (150 mM NaCl, 2 mM EDTA, 50mM Tris-HCl, 1% NP-40 and 0.25% sodium deoxycholate, pH 7.4) using a pestle and incubated 1h at 4ºC. Next brain lysates were centrifuged at 14,000xg for 10 min at 4°C to collect supernatant and samples were quantified following Bradford's method. Proteinase K was added to 50 μL of sample (previously prepared at 1μg/μL concentration) at different final concentration ranging from 0.3-0.5 μg/mL and incubated at 37ºC for 25 minutes under shaking. Digestion reactions were stopped by addition of the inhibitor PMSF (4mM) and samples (undigested and exposed to Proteinase K) were prepared in sample buffer 5X for Western-blotting analysis.

Proteasome activity. Proteasome activity in mice brain tissue was analysed following the 20S Proteasome activity assay kit protocol by Millipore (APT280). The assay detects the fluorophore 7-Amino-4-methylcoumarin (AMC) after cleavage from the labelled substrate LLVY-AMC. Briefly, 3 μg of protein from each sample was incubated for 1 h at 37°C with proteasome labeled substrate in 96 dark multiwells. The sensibility of the assay was tested performing serial dilution of proteasome positive control (1:4 to 1:256) of the stock solution in 1X Assay buffer. Fluorescence data was collected using a PE Biosystems CytoFluor 400 plate reader using a 380 nm excitation and 460nm emission filters.

Filter retardation assay. Filter retardation assay were performed as described in [5]. Briefly, cell cultures were rinsed once in cold PBS 1X and mechanically detached in PBS 1 X plus protease and phosphatase inhibitor cocktails Calbiochem (40 µl/well 12 wells plate). Cell samples were sonicated 3 times with 1s pulse and 1s stop sequence at 10% pulse amplitude. Brain extracts from 6 months mouse LRRK2 wild-type and LRRK2 G2019S variant were prepared by mechanical homogenization of 1 gr of tissue in solubilization buffer (150 mM NaCl, 2 mM EDTA, 50mM Tris-HCl, pH 7.4) using a pestle and incubated 1h at 4ºC. Then brain lysates were centrifuged at 14,000xg for 10 min at 4°C to collect supernatant. Protein amounts were quantified following Bradford's method. Ten µg of each sample were diluted to 120 µl in PBS 1X. The samples were immobilized on methanol equilibrated cellulose acetate membrane through a dot blot void system (BioRad).

Streptavidin pull down. Streptavidin pull down was performed as described in [6]. Briefly, HEK293 cells were transiently transfected and treated as indicated trough the text. The cells were then resuspended in 5ml ice cold PBS 1X, centrifuged at 150xg for 5 min and lysed in 1 ml of 50mM HEPES pH 7.4, 150mM NaCl, 0.5mM EDTA, 0.5% Triton X-100, protease inhibitors (Calbiochem) and phosphatase inhibitor cocktails II and IV (Calbiochem), after incubation for 1 h at 4°C in rotation. The cell lysate was recovered after 10 min centrifugation at 15000xg at 4°C and 10% of supernatant kept as input. The remaining supernatant was incubated with 25 µl of Streptavidin resin (IBA) for 1 hour at 4°C in rotation. After three washes in 0.5 ml of 50mM HEPES pH 7.4, 150mM NaCl, 0,2% Triton X-100, the bound protein was eluted in 60 µl of Laemmli buffer 1X after 10 min incubation at 52°C.

Solubility assay. HEK293 cells were cultivated in 12 well plates and transiently transfected and treated as indicated trough the text. Cells were rinsed with cold PBS1X and then lysed in Triton-X100 buffer at 4°C (50mM HEPES pH 7.4, 150mM NaCl, 1 % Triton X-100, protease inhibitors (Calbiochem) and phosphatase inhibitor cocktails II and IV (Calbiochem)). The cell lysate was kept on ice and briefly vortexed every 10 minutes for 3 times, then centrifuged at 16.000g for 10 minutes at 4°C. The Supernatant was collected as the detergent-soluble fraction and the pellet constituted the insoluble fraction. The pellet was resuspended in 75 ul of Laemmli sample buffer 2X, whereas the same volume of Laemmli sample buffer 5X was added to the soluble fraction.

Protein purification. HEK-293T cells were lysed in lysis buffer [20 mM Tris–HCl, pH 7.5, 150 mM NaCl, 1 mM EDTA, 2.5 mM $Na_4P_2O_7$, 1 mM beta-glycerophosphate, 1mM $NaVO_4$, Protease Inhibitor Mixture (Sigma-Aldrich)] by using a needle. Cleared lysates (1 ml) were incubated with 30 µl of anti-FLAG-M2-agarose beads by rotating overnight at 4°C. Resin complexes were washed with different buffers WB1 (20mM Tris–HCl pH7.5, 500mM NaCl) twice, WB2 (20mM Tris–HCl pH7.5, 350mM NaCl) twice, WB3 (20mM Tris–HCl pH7.5, 150mM NaCl) six times. Proteins were eluted in WB3 with 150 ng/µl of 3× FLAG peptide) for 30 min at 4°C with shaking. Purified proteins were resolved by SDS–PAGE and stained with Coomassie Brilliant Blue to verify protein purity. Protein content was calculated by densitometry, using a standard curve with bovine serum albumin (BSA).

ATPase assay. NSF ATPase activity was quantified using the Malachite Green Assay by measuring the release of inorganic phosphate (Pi) due to the ATP hydrolysis with spectrophotometer as previously described [7]. 216 nM NSF was incubated with different ATP concentrations and 2 mM MgCl2 for 2h a 37°C. The samples were mixed with Malachite Green stock solution and the absorbance measured at 640nm. The values of absorbance were then converted into µmol of free Pi in solution using a standard curve. Kinetic constants were obtained by data fitting with the Michaelis-Menten kinetic model $Y = Vmax*S/(Km + [S])$.

Size Exclusion Chromatography (SEC) and dot blot analysis. SEC was performed as previously described [7]. Briefly, Strep-FLAG NSF WT and T465D transfected HEK-293T cells were lysed in 0.5ml of lysis buffer containing 0.06% (v/v) Triton X-100 and centrifuged. Cell lysates were separated on a Superose 6 10/300 column (Ge Healthcare, Waukesha, WI, USA) pre-equilibrated with 20mM Tris–HCl pH7.5, 150mM NaCl and 0.06% (v/v) Triton X-100. The flow rate used was 0.5ml/min. Fractions of 0.25ml were collected and spotted onto a nitrocellulose membrane and analyzed by dot blot. Densitometric analysis was performed by using ImageJ program.

Western-blotting. Protein samples were resolved on to 10-15% Tris-glycine polyacrylamide gels in SDS/Tris-glycine running buffer. Solubilized proteins were transferred to nitrocellulose or polyvinylidenedifluoride (PVDF) membranes in blotting buffer containing 10% methanol. The membrane was saturated for 1 h at RT in 5% nonfat dry milk in Tris-buffered saline and 0.1% Triton (TBS-T) and then incubated with the primary antibody in saturating solution for 90 min at RT. The unbound primary antibody was sheets was washed out in TBS-T (3x10 min) at RT and the membrane was incubated for 1 h at RT with horseradish peroxidase-conjugated anti-mouse or anti-rabbit IgGs. After 3 washes in TBS-T 10 min/each at RT, the immunoreactive proteins were visualized using enhanced chemioluminescence plus (ECL+, GE Healthcare, Little Chalfont, England). Densitometric analysis was carried out using Image J software.

Structure analysis. The Cryo-EM structure of NSF hexamer was downloaded from the PDB database, and the structural analysis was performed using the program PyMOL (*http://www.pymol.org/*). All the structural diagrams were prepared using the program PyMOL.

List of expressing vectors

HA- Ubiquitin (pcDNA3.1), HA- K48R Ubiquitin (pcDNA3.1); HA- K63R Ubiquitin (pcDNA3.1) HA- K29,48,63R Ubiquitin (pcDNA3.1) (kind gifts by Dr. Simona Polo, IFOM);

LRRK2 K1906M GFP (pcDNA3.1), LRRK2 G2019 GFP (pcDNA3.1) [described in [8];

Strep-FLAG hNSF WT (pcDNA3.1), Strep-FLAG hNSF T645A (pcDNA3.1) [described in [7]],

Strep-FLAG hNSF T645DE (pcDNA3.1) and Strep-FLAG hNSF T645D (pcDNA3.1) generated by site directed mutagenesis;

HA hNSF (pCMV HA-2) (kind gift by prof. Dario Alessi);

Strep-FLAG hNSF WT (pULTRA HOT) and Strep-FLAG hNSF T645D (pULTRA HOT) generated via cloning into NheI-BclI sites

List of primary antibodies

NSF (123 002-Synaptic System); alpha-Synuclein (D37A6- Cell Signaling); LC3 (NB100-2331- Novus Biologicals); p62 (ab109012- ABCAM); b-ACTIN (sc-47778 – Santa Cruz Biotechnology); FLAG (sc-166355- Santa Cruz Biotechnology); HA (Cat. #05-904- Merck Millipore); cleaved-caspase-3 (9H19L2- Invitrogen); TH (AB152- Merck Millipore); b3- Tubulin (ab18207- ABCAM); Synapsin-1 (D12G5- Cell Signaling); RAB 3a (107 111- Synaptic System); LRRK2 phospho S935 (UDD2 10(12) ab133450 – ABCAM); LRRK2 (MJFF2 (c41-2) ab133474 – ABCAM); LRRK2 phospho S1292 (MJFR-19-7-8 ab203181 – ABCAM)

List of secondary antibodies

Anti Rabbit IgG (H+L), made in goat, Biotinylated (BA-1000- Vector Laboratories); Anti Mouse IgG (H+L), made in horse, Biotinylated (BA-2000- Vector Laboratories)**;** Alexa Fluor® 488 AffiniPure Goat Anti-Rabbit IgG (H+L) (111-545-144 - Jackson ImmunoResearch); Goat IgG anti-Rabbit IgG (H+L)-TRITC (111-025-003 - Jackson ImmunoResearch); Peroxidase AffiniPure Goat Anti-Mouse IgG (H+L) (115-035-146 - Jackson ImmunoResearch); Peroxidase AffiniPure Goat Anti-Rabbit IgG (H+L) (115-035-003 - Jackson ImmunoResearch)

References

1. Garini Y, Vermolen BJ, Young IT. From micro to nano: recent advances in high-resolution microscopy. *Curr Opin Biotechnol*. 2005;16(1):3-12. doi:10.1016/j.copbio.2005.01.003

2. Schaefer LH, Schuster D, Schaffer J. Structured illumination microscopy: artefact analysis and reduction utilizing a parameter optimization approach. *J Microsc*. 2004;216(Pt 2):165-174. doi:10.1111/j.0022-2720.2004.01411.x

3. Meijering E, Jacob M, Sarria J-CF, Steiner P, Hirling H, Unser M. Design and validation of a tool for neurite tracing and analysis in fluorescence microscopy images. *Cytometry A*. 2004;58(2):167-176. doi:10.1002/cyto.a.20022

4. Ottaviani D, Marin O, Arrigoni G, et al. Protein kinase CK2 modulates HSJ1 function through phosphorylation of the UIM2 domain. *Hum Mol Genet*. 2017;26(3):611-623. doi:10.1093/hmg/ddw420

5. Perez Carrion M, Pischedda F, Biosa A, et al. The LRRK2 Variant E193K Prevents Mitochondrial Fission Upon MPP+ Treatment by Altering LRRK2 Binding to DRP1. *Front Mol Neurosci*. 2018;11:64. doi:10.3389/fnmol.2018.00064

6. Pischedda F, Szczurkowska J, Cirnaru MD, et al. A cell surface biotinylation assay to reveal membrane-associated neuronal cues: Negr1 regulates dendritic arborization. *Mol Cell Proteomics*. 2014;13(3):733-748. doi:10.1074/mcp.M113.031716

7. Belluzzi E, Gonnelli A, Cirnaru M-D, et al. LRRK2 phosphorylates pre-synaptic N-ethylmaleimide sensitive fusion (NSF) protein enhancing its ATPase activity and SNARE complex disassembling rate. *Mol Neurodegener*. 2016;11(1):1. doi:10.1186/s13024-015-0066-z

8. Gloeckner CJ, Kinkl N, Schumacher A, et al. The Parkinson disease causing LRRK2 mutation I2020T is associated with increased kinase activity. *Hum Mol Genet*. 2006;15:223-232.

LRRK2 G2019S kinase activity triggers neurotoxic NSF aggregation

Francesca Pischedda[1]*, Maria Daniela Cirnaru[2]*, Luisa Ponzoni[3], Michele Sandre[4], Alice Biosa[5], Maria Perez Carrion[1,6], Oriano Marin[4], Michele Morari[7], Lifeng Pan[8], Elisa Greggio[5], Rina Bandopadhyay[9], Mariaelvina Sala[3] and Giovanni Piccoli[1]#

1 CIBIO, Università degli Studi di Trento, Trento, Italy & Dulbecco Telethon Institute
2 Icahn School of Medicine at Mount Sinai, New York, USA
3 CNR, Institute of Neuroscience, Milan, Italy
4 Department of Biomedical Sciences (DSB), University of Padova, Italy
5 Department of Biology, University of Padova, Italy
6 Facultad de Farmacia, Universidad CEU San Pablo, Madrid, Spain
7 Department of Biomedical and Specialty Surgical Sciences, University of Ferrara, Italy
8 Shanghai Institute of Organic Chemistry, Shangai, China
9 Reta Lila Weston Institute of Neurological Studies and Department of Clinical and Movement Neuroscience, UCL Queen Square Institute of Neurology, London, UK

*equal contribution
corresponding author

Summary (max 150 words)

Parkinson's disease (PD) is characterized by the progressive degeneration of dopaminergic neurons within the substantia nigra pars compacta and the presence of protein aggregates in surviving neurons. LRRK2 G2019S mutation is one of the major determinants of familial PD cases and leads to late-onset PD with pleomorphic pathology, including alpha-synuclein accumulation and deposition of protein inclusions. We demonstrated that LRRK2 phosphorylates N-ethylmaleimide sensitive factor (NSF). We observed aggregates containing NSF in basal ganglia specimens from G2019S carrier PD patients and in cellular and animal models expressing the LRRK2 G2019S variant. We found that LRRK2 G2019S kinase activity induces the accumulation of NSF in toxic aggregates. Noteworthy, the induction of autophagy cleared NSF aggregation and rescued motor and cognitive impairment observed in aged hG2019S BAC mice. We suggest that LRRK2 G2019S pathological phosphorylation impacts on NSF biochemical properties~~hampers substrate catabolism~~, thus causing the formation of cytotoxic protein inclusions.

Highlights

- LRRK2 phosphorylates NSF *in vivo*
- NSF aggregates in complementary LRRK2 G2019S models
- LRRK2 G2019S kinase activity induces NSF accumulation in toxic aggregates
- Autophagy induction rescues hG2019S BAC mice motor and cognitive impairment

Introduction

Parkinson's disease (PD) is a heterogeneous movement disorder characterized by the progressive degeneration of dopaminergic neurons within the Substantia Nigra pars compacta (SNpc) and the formation of Lewy bodies containing alpha-synuclein in surviving neurons [reviewed in [1]]. Mutations in LRRK2 gene (PARK8; OMIM 609007) are linked to late-onset autosomal dominant PD, accounting for up to 13% of familial PD cases compatible with dominant inheritance [2] and 1 to 2% of sporadic PD patients [3]. Clinically and pathologically, the features of LRRK2-associated parkinsonism are often indistinguishable from idiopathic PD [reviewed in [4]]. Phylogenetically the LRRK2 kinase domain belongs to the TLK (tyrosine like kinases) and shows high similarity to Mixed lineage kinases (MLKs) [5]. Like MLKs, LRRK2 is a serine/threonine kinase with no detectable tyrosine kinase activity [6]. Disease segregating mutations in LRRK2 have been reported in the kinase domain (G2019S, I2020T), the Roc domain (N1347H, R1441C/G), and in the COR domain (Y1699C) [reviewed in [7]]. However, despite its relevance in PD, the physiological function of LRRK2 and the meaning of PD-linked mutations are yet to be completely understood. The inclusions observed in PD patients may be due to the failure of the protein clearance pathways or to aberrant precipitation of protein aggregates. LRRK2 kinase activity plays a major role in LRRK2 physiological and pathological activity [reviewed in [8]]. Few LRRK2 substrates have been characterized *in vivo*, including LRRK2 itself [9] and Rab proteins [10]. In this study, we described that LRRK2 phosphorylates NSF *in vivo*. Mice expressing hLRRK2 G019S via BAC [11] present an age-dependent motor and cognitive impairment together with the deposition of NSF aggregates. At the mechanistic level, LRRK2 phosphorylation triggers the formation of NSF toxic aggregates.

Results

hG2019S mice show an age-dependent motor and cognitive impairment

Previous studies described an age-dependent neuropathological and behavioral phenotype in hG2019S BAC (hG2019S) mice [11]. We characterized age-matched wild-type and hG2019S male mice at 3, 6, 12, and 18-months in a battery of behavioral tests, including spontaneous motor activity (figure 1A-B), balance beam, pole test, rotarod (figure 1C-G) and novel object recognition (figure 1H). Spontaneous activity did not differ between genotypes. Three-months old wild-type and hG2019S cohorts performed equally in all experiments, except in the rotarod test at 32 rpm, where hG2019S mice were significantly impaired. ~~.~~We noticed that hG2019S mice have an impairment in the motor performance at the balance beam and pole test at 6 months, in the rotarod (12 rpm) at 12 and 18 months, in the rotarod (32 rpm) at 6 and 18 months and in the rotarod resistance at 6 and 12 months. Finally, 6, 12, and 18 months old hG2019S mice scored significantly worse at the novel object recognition test in terms of mean discrimination index. These observations suggest that 6-months old hG2019S mice show motor and cognitive impairment.

G2019S mutation correlates with the deposition of NSF aggregates

Protein aggregation is an established histological hallmark of PD. LC3 decorates LB in PD and DLB patients [12,13]. We investigated the presence of proteinaceous aggregates in specimens from substantia nigra, striatum, cortex, and hippocampus obtained from 6-month old wild-type and hG2019S male mice via staining with LC3 antibody. Interestingly, we noticed the presence of a peculiar LC3 staining pattern in nigra, cortex, and hippocampus of hG2091S mice suggesting the presence of perinuclear pale bodies (supplementary figure 1) [13,14]. It has been suggested that LRRK2 mutations promote α-synuclein aggregation [15,16]. Therefore we studied the distribution of α-synuclein in different brain areas of 6-months old wild-type and hG2019S mice. However, we did not report any overt α-synuclein deposition in the hG2019S mice brain (supplementary figure 2). LB [17] and the related intranuclear inclusion bodies [18] contain more than 90 molecules, including NSF, which we described as LRRK2 functional partner [19,20]. Consequently, we analyzed the subcellular distribution of NSF in hG2019S cortical neurons. We noticed that NSF localizes in somatic structures positive for LC3 and p62 (figure 2A-B), i.e., resembling protein aggregates [21]. Protein aggregates form high molecular weight (HMW) complexes that are retained by acetate cellulose in the filter retardation assay [22]. We confirmed the presence of NSF HMW complex in the sample prepared from 6-months hG2019S mice brain (figure 2C-D) despite a similar expression of LRRK2 and NSF in the two mice lines (supplementary figure 3A-D). A well-established feature of protein aggregates is the resistance to proteinase-K digestion [23]. Thus we characterized NSF aggregates by limited proteolysis in brain homogenates gathered from 6-months old wild-type and hG2019S mice. Upon proteinase-K digestion, the 100 kDa MW band, corresponding to full-length NSF protein, gradually disappeared in samples prepared from wild-type but not from hG2019S mice (figure 2E-F). Histological analysis revealed the presence of NSF positive aggregates in nigral, striatal, hippocampal, and cortical sections prepared from 6-months hG2019S mice (figure 2G-H). NSF aggregation resulted less evident in 12-months old hG2019S mice, suggesting the existence of compensatory mechanisms (supplementary figure 4). Next, we characterized post-mortem basal ganglia specimens obtained from healthy control, idiopathic, and G2019S PD cases. The detergent solubility profile characterizes proteinaceous aggregates from the biochemical standpoint [24]. Interestingly, while Tris-buffered saline (TBS)- soluble NSF levels were comparable among the groups (figure 3A, C), the yield of NSF in the SDS soluble fraction was higher in the sample prepared from idiopathic or G2019S PD patients (figure 3B, D). Besides, we found that NSF decorates a proportion of α-synuclein positive structure in both idiopathic and G2019S PD cases (figure 3E and table 1). To directly assess the impact of G2019S mutation on the aggregation state of NSF, we analyzed dopaminergic neurons differentiated from G2019S human neuronal precursor and their respective gene-corrected line (supplementary figure 3E-F). By filter retardation assay, we noticed that NSF forms HMW complexes in samples prepared in G2019S dopaminergic neurons (figure 3F-G). Altogether this evidence suggests that LRRK2 G2019S mutation correlates with the deposition of NSF aggregates in both murine and human models.

LRRK2 G2019S kinase activity triggers NSF aggregation

Previously we have shown that NSF is an LRRK2 substrate *in vitro* [25]. To complement this finding, we generated an antibody specifically recognizing NSF phosphorylated at Thr645 (supplementary figure 5A-B). This reagent showed that NSF phosphorylation at Thr645 increased in post-mortem samples gathered from G2019S patients specimen (figure 4A-C) and in several brain areas gathered from 6-months hG2019S mice (figure 4D-E). Structural analysis of NSF (PDB ID: 3J94) revealed that the side chain of T645 is close to the ATP-binding site on the D2 domain involved in NSF oligomerization (aa 490-744) (figure 4F-G). By differential detergent solubility assay, we noticed an increased amount of NSF in the insoluble fraction gathered from hG2019S cortical neurons (figure 4H-I) and from N2A cells overexpressing hLRRK2 G2019S (supplementary figure 5C-D). This phenomenon depends on the phosphorylation on T645, given that the co-expression of hLRRK2 G2019S did not alter the solubility profile of NSF T645A (supplementary figure 5E-F). This biochemical evidence suggests that LRRK2 G2019S triggers NSF aggregation. Proteins can aggregate upon impairment of proteasome activity [26]. Accordingly, a filter retardation assay showed that the pharmacological inhibition of the proteasome induced NSF aggregation in wild-type neurons. Instead, hG2019S neurons were characterized by a high basal amount of HMW NSF that did not further increase upon MG-132 treatment (supplementary figure 5G-H). Indeed, LRRK2 G2019S might interfere with the activity of the proteasome. However, we reported a comparable UPS proteolytic activity in 6- or 12-months old wild-type and hG2019S mice (supplementary figure 5I). Therefore, we thought that other mechanisms must underline LRRK2 G2019S dependent NSF aggregation. Phosphorylation may directly affect protein folding and oligomeric state [27]. To dissect the biological consequence of NSF phosphorylation on Thr645, we generated by site-direct mutagenesis the NSF phosphomimetic variant NSF T645D. NSF T645D has an augmented ATPase activity (supplementary figure 6A-B), it is prone to aggregation independently from UPS blockade (supplementary figure 6C-D) and it forms higher-molecular weight complexes than the wild-type variant (supplementary figure 6E-F). NSF T645D is strongly enriched in the insoluble fraction, as suggested by differential detergent solubility (figure 4J-K). Strikingly, once co-expressed with HA-NSF wild-type, NSF T645D influenced the solubility of the wild-type protein (figure 4J, L). These observations suggest that phosphorylation at T645 triggers NSF aggregation. Once entrapped within aggregates, proteins get cleaved and tagged by ubiquitin [28]. Our western-blotting analysis revealed that NSF T645D undergoes proteolytic cleavage and is strongly decorated by ubiquitin (figure 4M-O). In ubiquitin chains, each monomer can be conjugated through different lysine residues, generating a code with functional consequences [reviewed in [29]]. To determine the nature of ubiquitination occurring on the two NSF variants, we expressed in HEK293 cells NSF WT and NSF T645D together with ubiquitin wild-type or with individual ubiquitin constructs missing lysine 48, 48 and 63 or 48, 63 and 29, respectively. We noticed that the degradation and the ubiquitination of the two NSF variants depend on different lysine residues (supplementary figure 6G-K). Altogether, these data suggest that LRRK2 phosphorylation at T645 alters NSF biochemical properties and promotes its aggregation.

NSF over-expression is detrimental for hG2019S neurons in an LRRK2 kinase-dependent manner. NSF plays a crucial role in neurons [30]. To investigate whether NSF aggregation may be neurotoxic, we infected wild-type and hG2019S cortical neurons with lentiviral viruses expressing mCherry alone or together with NSF wild-type, the phospho-null variant NSF T645A or the phospho-mimetic variant NSF T645D. Neurons were treated from DIV10 to DIV14 with DMSO or GSK2578215A (GSK, 0.2 μM daily) and then processed at DIV16 (figure 5A and supplementary figure 7). Neurite retraction is an established marker of neuronal damage [31]. Our morphological analyses revealed that the over-expression of either NSF wild-type or T645A had no major effect on wild-type neuron morphology. Instead, NSF T645D was detrimental to wild-type neurons.

Noteworthy, NSF wild-type over-expression caused a significant reduction of neurite number in hG2019S neurons. Such morphological phenotype was absent in hG2019S neurons over-expressing the phospho-null NSF T645A variant (figure 5B). The analysis of neuronal viability via MTT assay confirmed this outcome (figure 5C). Interestingly, the chronic treatment with the LRRK2 kinase inhibitor GSK2578215A prevented the neurite loss of hG2019S cultures expressing wild-type NSF but did not ameliorate the overall viability. Cumulatively, these data indicate that NSF is neurotoxic upon LRRK2 phosphorylation.

Trehalose treatment clears NSF aggregates

Autophagy can attenuate protein aggregation [32]. Basal autophagy resulted similar in 6-months old wild-type and hG2019S mice (supplementary figure 8A-B). We used trehalose, a well-established autophagic inducer [33], to stimulate autophagy in wild-type and hG2019S cortical neurons (supplementary figure 8C-D). The filter retardation assay suggested that trehalose treatment reduced NSF aggregation in HEK293 cell over-expressing NSF and treated with MG132 (supplementary figure 8E-F). *In vivo*, trehalose treatment reduced NSF aggregation in 6-months old hG2019S male mice (1% in the drinking water, 1-month; supplementary figure 8G-H) without significant impact on animal weight (supplementary figure 8I). Specifically, trehalose treatment reduced the number of cells decorated by NSF in substantia nigra (figure 6), striatum (figure 7), cortex, and hippocampus (supplementary figure 9) region of hG2019S mice. Caspase-3 cleavage precedes apoptotic cell death. We noticed a significant increase of cleaved caspase-3 positive cells in nigra (figure 6) and striatum (figure 7) without any overt loss of TH density. Caspase-3 positive cells were also evident in the cortex and hippocampus (supplementary figure 9) of hG2019S mice. Trehalose treatment significantly reduced the number of caspase-3 positive cells in substantia nigra (figure 6), striatum (figure 7), cortex, and hippocampus (supplementary figure 9) of hG2019S mice. Our observations suggest that trehalose treatment cleared NSF aggregation and reduced cell death in hG2019S mice brain.

Trehalose treatment ameliorates motor and cognitive phenotype in hG2019S mice

Next, we profiled the motor and cognitive performances in 6-month old hG2019S and wild-type male mice upon chronic treatment with trehalose (figure 8). We reported a robust recovery of motor and cognitive abilities in trehalose-treated animals. In particular, trehalose treatment ameliorated the performances at the 6-mm balance beam (figure 8C), at the 32-rpm rotarod (figure 8F), the rotarod resistance at 12 rpm (figure 8G) and the novel object recognition (figure 8H). We also observed a partial improvement in motor and cognitive performances (in the rotarod 32 rpm and in the novel object recognition) in 12-month old hG2019S mice treated with trehalose starting at ~~month~~ 10 months (1% in the drinking water, 2-month; supplementary figure 10~~8~~). Altogether, these observations suggest that trehalose treatment is beneficial in rescuing behavioral defects of hG2019S mice.

Discussion

LRRK2 and the proteostatic control

In the present study, we show that hG2019S mice present an age-dependent motor and cognitive impairment together with the deposition of protein aggregates containing NSF and signs of cell death in substantia nigra, striatum, cortex, and hippocampus. Post-mortem brain investigation demonstrated that LRRK2 G2019S patients often show synucleinopathy, occasionally tauopathy, suggesting a role for LRRK2 in protein inclusion pathology [34]. The description of frontotemporal ubiquitinated neuronal intranuclear inclusions in one patient carrying G2019S substitution indicates that the LRRK2 pathological impact is not restricted to the substantia nigra [35,36].

LRRK2 kinase activity leads to protein accumulation without affecting the catalytic activity of the proteasome or expression levels of proteasomal core subcomplexes [37]. Instead, LRRK2 influences the autophagic pathways at multiple levels [reviewed in [38–40]. The investigation of *LRRK2*-deficient mice revealed a biphasic alteration of autophagy in the kidney [41,42]; however, similar studies in an independent *LRRK2*-knock out mouse line demonstrated an accumulation of secondary lysosomes in the kidney without major involvement of autophagy [43]. Our understanding of the impact of LRRK2 mutations on autophagy is still limited. Many authors conclude that G2019S mutation increases autophagy in different models, including stable cell lines [44,45], fibroblasts [46], iPS derived neurons [47], *C.Elegans* [48] and mice [49]. However, other studies have reported that the same mutation reduces [50] or at least does not affect [51,52] autophagy. Such conflicting results leave unclear the impact of LRRK2 G2019S mutation on autophagy [53]. Still, increased accumulation of protein aggregates has been reported in complementary LRRK2 G2019S models [54–57]. Thus it might be possible that LRRK2 controls protein clearance acting upstream of the two main protein-clearance mechanisms.

Phosphorylation can trigger protein aggregation

Post-translational modifications regulate protein structure. In particular, phosphorylation can dictate protein folding and eventually, aggregation state. In the context of PD, phosphorylation has a severe impact on alpha-synuclein [reviewed in [58]]. While soluble, monomeric alpha-synuclein is largely not phosphorylated in physiological conditions, up to 90% of LB-synuclein is phosphorylated on Ser-129 [59]. It is still unresolved whether phosphorylation might trigger or impair alpha-synuclein aggregation or toxicity. While several reports claim that phosphorylation at Ser-129 favors protein aggregation [60,61] other authors described opposite or no effect [62,63]. However, phosphorylation at Ser-129 influences alpha-synuclein sub-cellular localization [64], suggesting that such PTM dictates alpha-synuclein function and fate. Similarly, hyperphosphorylated Tau protein precipitates in toxic aggregates and destabilizes the axonal tubulin cytoskeleton [65]. *In vitro* evidence shows that the phosphorylation of specific Tau residues modifies local folding, thus affecting global structure [66,67]. We showed that LRRK2 phosphorylates NSF on Thr-645 *in vitro* [25] as well as *in vivo* (here). Based on our structural analysis, the side chain of T645 falls in proximity to the ATP-binding site on NSF located on the D2 domain (aa 206-477). In particular, Thr-645 lies very close to the phosphate group of the bound ATP molecule. ATP binding on the D2 domain is essential for the formation of NSF hexamer [68]. We determined by complementary means that upon phosphorylation at Thr-645 NSF forms *bona fide* HMW aggregates, being insoluble to Triton-X100 [69], resistant to proteinase-K treatment [23] and decorated by ubiquitin and p62 [70].

Altogether, our data suggest that the phosphorylation of NSF at T645 promotes NSF oligomerization and eventually triggers its precipitation into protein inclusions. Indeed, we noticed that acute LRRK2 kinase inhibition was not efficacious in resolving NSF aggregation. Short-term LRRK2 inhibition may avoid the further precipitation of NSF proteins, but not yet clear the pre-existing aggregates. It would be useful evaluating whether long-lasting kinase inhibition can remove NSF aggregates. However, the toxicity observed *in vitro* prevented the assessment of the impact of chronic LRRK2 inhibition in primary cultures. It is unlikely that LRRK2-mediated phosphorylation is sufficient by itself to cause NSF aggregation. Actually, in idiopathic PD patients, we noticed that NSF is expressed at a high level and decorates a proportion of LB. This evidence may argue against a causative role for LRRK2 kinase activity. However, it has been recently postulated a role for LRRK2 in idiopathic PD [9]. It is tempting to speculate that in presence of increased NSF level even the low kinase activity characterizing wild-type LRRK2 may be sufficient to promote NSF aggregation. As reported for other aggregation-prone proteins like tau, it is conceivable that NSF has an intrinsic propensity towards aggregation that is pathologically exacerbated upon LRRK2 phosphorylation. Furthermore, accumulating evidence advocate a role in PD for NSF. Several linkage analyses nominate NSF as a robust risk factor for PD [71–75]. Our hypothesis is that different factors, including but not limited to increased NSF level and LRRK2 kinase activity, may trigger the pathological aggregation of NSF.

NSF aggregation, aging, and neuronal toxicity

NSF is a key component of presynaptic machinery, allowing the first step of SV recycling [76]. Numerous studies have shown that depletion of cytosolic NSF impair membrane fusion machinery [77] and results in the accumulation of intracellular vesicles [78,79]. Thus, NSF aggregation might affect presynaptic fusion machinery. Interestingly, it has been reported that experimental ischemia induces NSF aggregation into Triton-X100 insoluble inclusions that harm neuronal function via sequestering synaptic vesicle [80]. A presynaptic dysfunction might indeed explain the early-stage manifestation of PD observed in animal models [11,81,82] or presymptomatic LRRK2 G2019S carriers [83]. However, it is difficult to envisage how aberrant vesicle release could cause the overt neuronal death that characterizes the late phase of the disease. Neurons benefit from several pathways to effectively handle protein aggregation, but the ultimate resource to counteract proteinaceous stress is the degradative clearance of misfolded protein [84]. Nonetheless, the structure of the proteasome complex itself disfavours the removal of large oligomeric and aggregated proteins: substrates need to be unfolded to pass through the tight pore of the proteasome barrel [85]. Autophagy may help, being capable of handling large protein aggregates [86,87]. Unfortunately, both autophagy and proteasome activity pronouncedly decline with aging [88–90]. Thus, aging and pathological LRRK2 phosphorylation together may contribute to the deposition of NSF aggregates. Given the low stoichiometry that we reported for LRRK2-driven NSF phosphorylation *in vitro* [25],-it may well be that NSF phosphorylation occurs at low rate *in vivo*. However, we noticed that T465D NSF affects the detergent solubility of the unmodified protein. Thus, we may depict a model where few phosphorylated NSF molecules lead the formation of pathological seeds capable of sequestering unphosphorylated protein into large aggregates that accumulate along with aging.

Hints towards a therapy

Altogether this evidence may call for a therapeutic strategy targeting LRRK2 kinase activity. Several brain penetrant LRRK2 selective inhibitors have been identified [reviewed in [91]]; however the broad expression of LRRK2 in other organs apart from the central nervous system, including lung, kidney and the immune system raise issues about side effects [92–97]. Presently, complementary therapeutic approaches are still needed. Targeting the protein aggregates caused by LRRK2 kinase activity may be clinically relevant. It is reasonable to predict that LRRK2 kinase activity affects the biochemical profile of other substrates besides NSF. Thus, a more holistic solution is needed. The activation of autophagy may promote the clearance of toxic protein aggregates. We report that chronic treatment with trehalose reduced NSF aggregation and ameliorated motor and cognitive phenotype in aged G2019S mice. However, it affected at a certain extent wild-type mice motor and cognitive performances. Therefore, long-lasting induction of autophagy may rise safety concerns. We deem that while in mutant mice p62 positive NSF aggregates recruits the autophagic machinery, in wild-type mice a prolonged activation of this catabolic process may self-digest proteins and organelles and eventually result in cellular toxicity. Still, treatment with trehalose already demonstrated to be protective in models of Huntington disease, spinocerebellar ataxia, Machado-Joseph disease, and Parkin-PD [98–101]. However, the pharmacokinetics properties of trehalose are poor. The small intestine, kidney, and CNS expression of trehalose catalytic enzyme, trehalase, limits its bio-availability [102]. Also, dietary trehalose results in digestive issues [103] and may enhance the virulence of common nosocomial pathogen [104]. These issues severely reduce the possibility of introducing trehalose into the clinical management of PD patients. In conclusion, boosting autophagy may be a powerful therapeutic strategy in LRRK2-PD, but a clinically relevant drug is still to be discovered.

Experimental procedures

Animals

All animal protocols were approved by the University of Trento and National Ministery of Health (IACUC 793/2016-PR). The *G2019S-LRRK2* BAC mice were previously described [11] and have been backcrossed onto the C57BL/6J mice for >10 generations.

Animals were kept in a normal light/dark cycle (12 hours light/ 12 hours dark) and had free access to food and water. All procedures involving animals were approved by Institutional agencies (OPBA- Università degli Studi di Trento) and Italian Ministry of Health (Università degli Studi di Trento prot. n. 793/2016-PR). At 5 or 10 months, Wild-type and *G2019S-LRRK2* BAC male littermates were divided into trehalose and control groups. In the trehalose group, mice were offered 1% trehalose drinking water solution. The treatment solution was changed every week. In the control group, mice were given drinking water. Mice body weight was measured every week since the start of treatment. Only male mice were used in our experiments due to a strong gender effect (Pischedda et al., manuscript in preparation).

Assays in post-mortem specimen

In total, 5 idiopathic, 4 G2019S and 5 control human brain cases were used in the study which were obtained from the archives of Queen Square Brain Bank following appropriate local ethics committee approval. Demographic details of the cases have been described previously [24]. For biochemical analysis, 5µg of TBS soluble fraction and 10µg from TBS-5% SDS fractions of basal ganglia homogenates were run on 10% Bis-tris gels with MOPS as running buffer. Details of homogenisation and fractionation procedure is mentioned in a previous publication [24]. Protein from gels were transferred onto PVDF membranes and probed with NSF (SYSY, mouse monoclonal) and beta actin (Sigma, mouse monoclonal) antibodies overnight with shaking. Following incubation with appropriate HRP conjugated secondary antibodies, blots were visualized by enhanced chemiluminescence (Pierce; UK) detection. Protein expression levels were determined by densitometry and NSF results normalised to beta-actin levels. For immunohistochemical evaluation, 8µm substantia nigra sections from control, 4 iPD and 2 G2019S-LRRK2 PD were dewaxed in xylene, and pre-treated with 95% formic acid for 10min to expose antigenic sites. Standard immunohistochemistry protocol was followed using NSF (1:200 mouse monoclonal; SY-SY) and alpha-synuclein (1: 300; rabbit polyclonal, Abcam) primary antibodies with o/n incubation at 4°C. Double immunofluorescence was performed using tetramethyl rhodamine labelled secondary antibody for alpha-synuclein and NSF with the fluorescein signal amplification kit (Perkin Elmer, UK). Following adequate washes to remove background fluorescence, sections were mounted with Aquamount (Merck, UK). Control sections where primary antibody was omitted displayed no significant background staining. Fluorescent signals from sections were scanned using Leica fluorescent microscope (Leica CTR6000). Total alpha-synuclein positive LBs were counted from each section and the proportion of NSF+ve LBs were derived. Human brains were donated to the Queen Square Brain bank for neurological disorders, UCL Queen Square Institute of Neurology and stored under a research license No:12198.

Behavioural tests

Spontaneous Motor Activity. Spontaneous motor activity was evaluated in an automated activity cage (43 cm × 43 cm × 32 cm) (Ugo Basile,Varese,Italy) placed in a sound-attenuating room as previously described [105]. Cumulative horizontal and vertical beam breaks were counted for 3 hours. *Balance Beam walking.* The beam apparatus consists of 1 meter beams with a flat surface of 12 mm or 6 mm width resting 50 cm above the table top on two poles according to [106]. A black box is placed at the end of the beam as the finish point. Nesting material from home cage is placed in the black box to attract the mouse to the finish point. A lamp (with 60 watt light bulb) is used to shine light above the start point and serves as an aversive stimulus. A video camera is set on a tripod to record the performance. On training days, each mouse crosses the 12 mm beam 3 times and then the 6 mm beam 3 times. The time required to cross to the escape box at the other end (80 cm away) is measured with a stopwatch. The stopwatch is started by the nose of the mouse entering the center

80 cm, and stopped when the animal reaches the end of the 80 cm. Once the mice are in the safe box, they are allowed some time (~15 secs) to rest there before the next trial. The mice rest for 10 min in their home cages between training sessions on the two beams. On the test day, the time to cross each beam is recorded. The beams and box are cleaned of mouse droppings and wiped with towels soaked with 70% ethanol and then water before the next mouse is placed on the apparatus.

Pole test. In the vertical pole task, the mouse was placed on a vertical wire-mesh pole with its head facing upwards. Mice were habituated to the task in 2 trials per day for 2 days. On test day (third day) mice were subjected to 5 trials: the total time taken to turn the body and to descend was recorded according to [107]. A cut-off of 60 sec was given. Data were shown as mean of 5 trials evaluated during the test day.

Rotarod. The rotarod apparatus (Ugo Basile, Biological Research Apparatus, Varese, Italy) was used to measure fore and hindlimb motor coordination and balance (Dauge et al. 2001). During the training period, each mouse was placed on the rotarod at a constant speed (12 or 32 rpm) for a maximum of 120 sec, and the latency (sec) to fall off the rotarod, within this time period, was recorded. Mice received four tests/trial each day for 4 consecutive days. The fourth test of each trial was evaluated for statistical analysis. The fifth day mice were submitted to Rotarod resistance at a constant speed (12 rpm) for a maximum of 30 min and the latency (sec) to fall was measured.

Novel object recognition. The novel-object recognition test was performed over a 3-day period in an open plastic arena (60 cm x 50 cm x 30 cm), as previously described [108]. Animals were habituated to the test arena for 10 min on the first day. After 1 day of habituation, the mice were exposed to familiarization (T1) and novel-object recognition (T2). During the initial familiarization stage, two identical objects were placed in the centre of the arena equidistant from the walls and from each other. Each mouse was placed in the centre of the arena between the two objects for 20 min or until it had completed 30 s of cumulative object exploration. Object recognition was scored when the animal was within 0.5 cm of an object with its nose toward the object. Exploration was not scored if a mouse reared above the object with its nose in the air or climbed on an object. Mice were returned to the home cage after familiarization and then tested again after different delays (from 5 min to 24 h later). A novel object (never seen before) took the place of one of the two familiars. Scoring of object recognition was performed in the same manner as during the familiarization phase. From mouse to mouse the role (familiar or new object) as well as the relative position of the two objects were counterbalanced and randomly permuted. The objects for mice to discriminate consisted of white plastic cylinders and coloured plastic Lego stacks of different shapes. The arena was cleaned with 70% ethanol after each trial. An experimenter blind to the genotype group manually recorded the exploration times to the objects for each animal. Total time spent exploring the two objects during T1 and T2 was also calculated.

Cell cultures

Neuron cultures were prepared from mouse cortexes obtained from embryonic day 15.5–16.5 wild-type or hG2019S mice (C57BL/6J) as previously reported [109,110]. Briefly, after brain dissection the cortexes were mechanically dissociated after 15 min incubation with 0.25% Trypsin (Euroclone) at 37 °C in agitation. The resulting cells were counted and cryopreserved or directly plated on previously poly-D-lysine (Sigma) coated wells or cover slips, according to the desired density. High density (750–1000 cells/mm2) neuron cultures were plated on 12-well plastic tissue culture plates (Iwaki; Bibby Sterilin Staffordshire, UK) and medium-density (150–200 cells/mm2) onto 12mm diameter cover slips inserted into 24-well plastic tissue culture plates (Iwaki). The cells were grown in Neurobasal at 37°C and 5% CO_2. Neuronal transfection was carried out using Lipofectamine 2000 (Life Technologies) following the manufacture's instruction. The cells were treated with LRRK2 kinase inhibitor, GSK-2578215A (Tocris Bioscience, Bristol, UK), MG132 (Tocris Bioscience, Bristol, UK) and trehalose (Sigma) by addition to culture media at the concentrations indicated through the text.

N2A (ATCC CCL-131) and HEK293 cells (ATCC CRL-1573) were cultured in DMEM complete: Dulbecco's modified Eagle's medium (DMEM, Euroclone) supplemented with 10% fetal bovine serum (FBS, Euroclone) at 37°C and 5% CO2. HEK293 were transiently transfected using linear polyethylenimine (PEI, Polysciences) with ratio DNA: PEI 0.8:100. 4 µg of DNA were dissolved in 0.5 ml of PEI solution and vortexed for 20 sec. The DNA-PEI mix was incubated for 10 minutes at room temperature (RT) and added directly to the cells. The medium was changed after 24h and the cells were lysed 48h post transfection. Lentiviruses were produced by transient transfection of HEK293T cells (ATCC CRL-3216) according to standard protocols [111]. Primary cortical cultures were transduced at DIV4 with lentiviruses at multiplicity of infection 3 (MOI3). The 3-(4,5-dimethylthiazol-2-yl)-2,5-diphenyltetrazolium bromide (MTT) assay was performed to measure culture viability as described [112]. High density (750–1000 cells/mm2) neuronal culture were infected at DIV 4 and processed for MTT assay at DIV16. Briefly, MTT ((3-(4, 5-dimethylthiazolyl-2)-2, 5-diphenyltetrazolium bromide- Sigma Aldrich) stock solution 20X (5mg/ml in MilliQ water) was diluted in neuronal complete media and cells were were incubated with MTT mix for 30 minutes at 37°C with 5% CO2. After incubation, media was discarded, cells were resuspended in DMSO to dissolve the intracellular purple precipitates and the absorbance was measured at 570 nm with the Plate reader Infinite 200 PRO (Tecan Life Sciences). Toxicity was calculated as 1- cell viability, being cell viability expressed as fold over control.

iDA culture

Wild-type, G2019S and G2019S corrected Human iPSCs derived Neuronal Precursors Cells (NPCs) were obtained from Dr. Deleidi lab and cultured as previously reported [113]. Briefly, the cells were expanded in 50:50 DMEM F12 and Neurobasal medium with: 1% P/S, 1% B27 (without Ascorbic acid), 0,5% N2, 1%L-glutamax, 150 µM Ascorbic acid, 3 µM CHIR, 0.5 µM Purmorphamine (PMA) (NPC expansion medium). Media was changed every other day and cells were passed every week after 10 min incubation with Acutase (200ul/12 well). The cells were re-plated at a 1:10 ratio in 12-well plates pre-coated with Matrigel (1:30 from Stock) in 'NPC expansion medium' supplemented with 10 µM ROCK inhibitor for the first day after splitting. After the second passage, when the cells reached 80% of confluency, the media was changed to Ventral CNS differentiation medium (50:50 DMEM F12 and Neurobasal medium with: 1% P/S, 1% B27 (without Ascorbic acid), 0,5% N2, 1% L-glutamax, 100 ng/mL FGF8, 200 µM of Ascorbic acid and 1µM PMA. When confluent the cells were split with Acutase and re-plated in Matrigel coated 6 wells plate at a 1:1 ratio. The media was changed every other day. After 10 days the Ventral CNS differentiation medium I was changed to maturation medium (50:50 DMEM F12 and Neurobasal medium with: 1% P/S, 1% B27 (without Ascorbic acid), 0,5% N2, 1%L-glutamax, 10 ng/mL BDNF, 10 ng/mL GDNF, 1ng/mL TGF-b3, 200 µM ascorbic acid, 500 µM dbcAMP and 0,5 µM PMA). After 48h the media was changed to dopaminergic differentiation medium (50:50 DMEM F12 and Neurobasal medium with: 1% P/S, 1% B27 (without Ascorbic acid), 0,5% N2, 1%L-glutamax, 10 ng/mL BDNF, 10 ng/mL GDNF, 1ng/mL TGF-b3, 200 µM ascorbic acid, 500 µM dbcAMP). The cells were kept in dopaminergic differentiation medium until the end of the experiment and the medium was changed every 2-3 days.

Statistical analysis and guidelines

All data are plotted as box, with minimum, maximum and median indicated. The normality of data distributions was determined using the D'Agostino and Pearson omnibus normality test, followed by an unpaired Student's t test, ANOVA followed by Tuckey's post-hoc test or two-way ANOVA followed by Bonferroni or Student's t post-hoc test as appropriate. The indication of number of experiment (n) and level of significance (p) are indicated throughout the text. All methods were performed in accordance with the relevant guidelines and national regulations.

Data availability

The data that support the findings of this study are available from the corresponding author, upon reasonable request.

Further methods, including immunohistochemistry, immunofluorescence, polyclonal phospho-specific NSF antibody production and purification, biochemical assays, list of expressing vectors, list of primary antibodies, and list of secondary antibodies are described in the Supplementary experimental procedures.

Author Contributions

F.P., M.D.C, L.P., M.S., A.B., and M.P.C. performed experiments. O.M., M.M., Li.P., E.G., R.B., M.E.S., and G.P. analysed data and wrote the paper.

Acknowledgments

G.P. is supported by Fondazione Telethon (grant TDPG00514TA), MIUR (PRIN-2017ENN4FY), and Fondazione Cariplo (project 2019-3415). F.P. received support by Fondazione Caritro -(project 2019.0230). This work was supported by Fondazione Cariplo (grant 2011-0540) to G.P. and E.G. and Fondazione Telethon (grant GGP12237) to G.P., E.G. and M.M. G.P. is grateful to the Michael J. Fox Foundation, the FIRB program (grant RBFR08F82X_002) and Fondazione Grigioni per il morbo di Parkinson. R.B. is funded by the Reta Lila Weston Trust and the British Neuropathological Society. We gratefully thank Prof. Matthew Farrer and Dr. Heather Melrose for providing LRRK2 hG2019S BAC mice, to Marzia Indrigo for excellent technical advice and Giuseppe La Tona for support in animal handling.

Competing interests

The authors report no competing interests

References

1. Obeso JA, Stamelou M, Goetz CG, et al. Past, present, and future of Parkinson's disease: A special essay on the 200th Anniversary of the Shaking Palsy. *Mov Disord*. 2017;32(9):1264-1310. doi:10.1002/mds.27115

2. Paisan-Ruiz C, Nath P, Washecka N, Gibbs JR, Singleton AB. Comprehensive analysis of LRRK2 in publicly available Parkinson's disease cases and neurologically normal controls. *Hum Mutat*. 2008;29(4):485-490.

3. Taylor JP, Mata IF, Farrer MJ. LRRK2: a common pathway for parkinsonism, pathogenesis and prevention? *Trends Mol Med*. 2006;12(2):76-82.

4. Whaley NR, Uitti RJ, Dickson DW, Farrer MJ, Wszolek ZK. Clinical and pathologic features of families with LRRK2-associated Parkinson's disease. *J Neural Transm Suppl*. 2006;(70):221-229.

5. Marin I. The Parkinson disease gene LRRK2: evolutionary and structural insights. *Mol Biol Evol*. 2006;23(12):2423-2433.

6. West AB, Moore DJ, Choi C, et al. Parkinson's disease-associated mutations in LRRK2 link enhanced GTP-binding and kinase activities to neuronal toxicity. *Hum Mol Genet*. 2007;16(2):223-232.

7. Berwick DC, Heaton GR, Azeggagh S, Harvey K. LRRK2 Biology from structure to dysfunction: research progresses, but the themes remain the same. *Mol Neurodegener*. 2019;14(1):49. doi:10.1186/s13024-019-0344-2

8. Taylor M, Alessi DR. Advances in elucidating the function of leucine-rich repeat protein kinase-2 in normal cells and Parkinson's disease. *Curr Opin Cell Biol*. 2020;63:102-113. doi:10.1016/j.ceb.2020.01.001

9. Di Maio R, Hoffman EK, Rocha EM, et al. LRRK2 activation in idiopathic Parkinson's disease. *Sci Transl Med*. 2018;10(451). doi:10.1126/scitranslmed.aar5429

10. Steger M, Tonelli F, Ito G, et al. Phosphoproteomics reveals that Parkinson's disease kinase LRRK2 regulates a subset of Rab GTPases. *Elife*. 2016;5. doi:10.7554/eLife.12813

11. Melrose HL, Dächsel JC, Behrouz B, et al. Impaired dopaminergic neurotransmission and microtubule-associated protein tau alterations in human LRRK2 transgenic mice. *Neurobiol Dis*. 2010;40(3):503-517. doi:10.1016/j.nbd.2010.07.010

12. Higashi S, Moore DJ, Minegishi M, et al. Localization of MAP1-LC3 in vulnerable neurons and Lewy bodies in brains of patients with dementia with Lewy bodies. *J Neuropathol Exp Neurol*. 2011;70(4):264-280. doi:10.1097/NEN.0b013e318211c86a

13. Tanji K, Mori F, Kakita A, Takahashi H, Wakabayashi K. Alteration of autophagosomal proteins (LC3, GABARAP and GATE-16) in Lewy body disease. *Neurobiol Dis*. 2011;43(3):690-697. doi:10.1016/j.nbd.2011.05.022

14. Wakabayashi K, Tanji K, Odagiri S, Miki Y, Mori F, Takahashi H. The Lewy body in Parkinson's disease and related neurodegenerative disorders. *Mol Neurobiol*. 2013;47(2):495-508. doi:10.1007/s12035-012-8280-y

15. Cresto N, Gardier C, Gubinelli F, et al. The unlikely partnership between LRRK2 and α-synuclein in Parkinson's disease. *Eur J Neurosci*. 2019;49(3):339-363. doi:10.1111/ejn.14182

16. MacIsaac S, Quevedo Melo T, Zhang Y, Volta M, Farrer MJ, Milnerwood AJ. Neuron-autonomous susceptibility to induced synuclein aggregation is exacerbated by endogenous Lrrk2 mutations and ameliorated by Lrrk2 genetic knock-out. *Brain Commun*. 2020;2(1):fcz052. doi:10.1093/braincomms/fcz052

17. Xia Q, Liao L, Cheng D, et al. Proteomic identification of novel proteins associated with Lewy bodies. *Front Biosci*. 2008;13:3850-3856.

18. Pountney DL, Raftery MJ, Chegini F, Blumbergs PC, Gai WP. NSF, Unc-18-1, dynamin-1 and HSP90 are inclusion body components in neuronal intranuclear inclusion disease identified by anti-SUMO-1-immunocapture. *Acta Neuropathologica*. 2008;116(6):603-614. doi:10.1007/s00401-008-0437-4

19. Piccoli G, Onofri F, Cirnaru MD, et al. LRRK2 binds to neuronal vesicles through protein interactions mediated by its C-terminal WD40 domain. *Mol Cell Biol*. Published online March 31, 2014. doi:10.1128/MCB.00914-13

20. Piccoli G, Condliffe SB, Bauer M, et al. LRRK2 controls synaptic vesicle storage and mobilization within the recycling pool. *J Neurosci*. 2011;31(6):2225-2237. doi:10.1523/JNEUROSCI.3730-10.2011

21. Kopito RR. Aggresomes, inclusion bodies and protein aggregation. *Trends Cell Biol*. 2000;10(12):524-530.

22. Reid SJ, Rees MI, van Roon-Mom WMC, et al. Molecular investigation of TBP allele length: a SCA17 cellular model and population study. *Neurobiol Dis*. 2003;13(1):37-45.

23. Kheterpal I, Williams A, Murphy C, Bledsoe B, Wetzel R. Structural features of the Abeta amyloid fibril elucidated by limited proteolysis. *Biochemistry*. 2001;40(39):11757-11767.

24. Mamais A, Raja M, Manzoni C, et al. Divergent α-synuclein solubility and aggregation properties in G2019S LRRK2 Parkinson's disease brains with Lewy Body pathology compared to idiopathic cases. *Neurobiol Dis*. 2013;58:183-190. doi:10.1016/j.nbd.2013.05.017

25. Belluzzi E, Gonnelli A, Cirnaru M-D, et al. LRRK2 phosphorylates pre-synaptic N-ethylmaleimide sensitive fusion (NSF) protein enhancing its ATPase activity and SNARE complex disassembling rate. *Mol Neurodegener*. 2016;11(1):1. doi:10.1186/s13024-015-0066-z

26. Varshavsky A. The Ubiquitin System, Autophagy, and Regulated Protein Degradation. *Annu Rev Biochem*. 2017;86:123-128. doi:10.1146/annurev-biochem-061516-044859

27. Metskas LA, Rhoades E. Folding upon phosphorylation: translational regulation by a disorder-to-order transition. *Trends Biochem Sci*. 2015;40(5):243-244. doi:10.1016/j.tibs.2015.02.007

28. Olanow CW, Perl DP, DeMartino GN, McNaught KSP. Lewy-body formation is an aggresome-related process: a hypothesis. *The Lancet Neurology*. 2004;3(8):496-503. doi:10.1016/S1474-4422(04)00827-0

29. Akutsu M, Dikic I, Bremm A. Ubiquitin chain diversity at a glance. *J Cell Sci*. 2016;129(5):875-880. doi:10.1242/jcs.183954

30. Bonnycastle K, Davenport EC, Cousin MA. Presynaptic dysfunction in neurodevelopmental disorders: Insights from the synaptic vesicle life cycle. *J Neurochem*. Published online May 7, 2020. doi:10.1111/jnc.15035

31. Chernova T, Steinert JR, Guerin CJ, Nicotera P, Forsythe ID, Smith AG. Neurite Degeneration Induced by Heme Deficiency Mediated via Inhibition of NMDA Receptor-Dependent Extracellular Signal-Regulated Kinase 1/2 Activation. *Journal of Neuroscience*. 2007;27(32):8475-8485. doi:10.1523/JNEUROSCI.0792-07.2007

32. Fujikake N, Shin M, Shimizu S. Association Between Autophagy and Neurodegenerative Diseases. *Front Neurosci*. 2018;12:255. doi:10.3389/fnins.2018.00255

33. DeBosch BJ, Heitmeier MR, Mayer AL, et al. Trehalose inhibits solute carrier 2A (SLC2A) proteins to induce autophagy and prevent hepatic steatosis. *Sci Signal*. 2016;9(416):ra21. doi:10.1126/scisignal.aac5472

34. Taymans J-M, Cookson MR. Mechanisms in dominant parkinsonism: The toxic triangle of LRRK2, alpha-synuclein, and tau. *Bioessays*. 2010;32(3):227-235. doi:10.1002/bies.200900163

35. Dächsel JC, Ross OA, Mata IF, et al. Lrrk2 G2019S substitution in frontotemporal lobar degeneration with ubiquitin-immunoreactive neuronal inclusions. *Acta Neuropathol*. 2007;113(5):601-606. doi:10.1007/s00401-006-0178-1

36. Kalia LV, Lang AE, Hazrati L-N, et al. Clinical correlations with Lewy body pathology in LRRK2-related Parkinson disease. *JAMA Neurol*. 2015;72(1):100-105. doi:10.1001/jamaneurol.2014.2704

37. Lichtenberg M, Mansilla A, Zecchini VR, Fleming A, Rubinsztein DC. The Parkinson's disease protein LRRK2 impairs proteasome substrate clearance without affecting proteasome catalytic activity. *Cell Death Dis*. 2011;2:e196. doi:10.1038/cddis.2011.81

38. Manzoni C, Lewis PA. LRRK2 and Autophagy. *Adv Neurobiol*. 2017;14:89-105. doi:10.1007/978-3-319-49969-7_5

39. Albanese F, Novello S, Morari M. Autophagy and LRRK2 in the Aging Brain. *Front Neurosci*. 2019;13:1352. doi:10.3389/fnins.2019.01352

40. Cogo S, Manzoni C, Lewis PA, Greggio E. Leucine-rich repeat kinase 2 and lysosomal dyshomeostasis in Parkinson disease. *J Neurochem*. 2020;152(3):273-283. doi:10.1111/jnc.14908

41. Tong Y, Yamaguchi H, Giaime E, et al. Loss of leucine-rich repeat kinase 2 causes impairment of protein degradation pathways, accumulation of alpha-synuclein, and apoptotic cell death in aged mice. *Proc Natl Acad Sci USA*. 2010;107(21):9879-9884. doi:10.1073/pnas.1004676107

42. Tong Y, Giaime E, Yamaguchi H, et al. Loss of leucine-rich repeat kinase 2 causes age-dependent bi-phasic alterations of the autophagy pathway. *Mol Neurodegener*. 2012;7:2. doi:10.1186/1750-1326-7-2

43. Herzig MC, Kolly C, Persohn E, et al. LRRK2 protein levels are determined by kinase function and are crucial for kidney and lung homeostasis in mice. *Hum Mol Genet*. 2011;20(21):4209-4223. doi:10.1093/hmg/ddr348

44. Gómez-Suaga P, Luzón-Toro B, Churamani D, et al. Leucine-rich repeat kinase 2 regulates autophagy through a calcium-dependent pathway involving NAADP. *Hum Mol Genet*. 2012;21(3):511-525. doi:10.1093/hmg/ddr481

45. Plowey ED, Cherra SJ, Liu Y-J, Chu CT. Role of autophagy in G2019S-LRRK2-associated neurite shortening in differentiated SH-SY5Y cells. *J Neurochem*. 2008;105(3):1048-1056. doi:10.1111/j.1471-4159.2008.05217.x

46. Yakhine-Diop SMS, Bravo-San Pedro JM, Gómez-Sánchez R, et al. G2019S LRRK2 mutant fibroblasts from Parkinson's disease patients show increased sensitivity to neurotoxin 1-methyl-4-phenylpyridinium dependent of autophagy. *Toxicology*. 2014;324C:1-9. doi:10.1016/j.tox.2014.07.001

47. Bravo-San Pedro JM, Niso-Santano M, Gómez-Sánchez R, et al. The LRRK2 G2019S mutant exacerbates basal autophagy through activation of the MEK/ERK pathway. *Cell Mol Life Sci*. 2013;70(1):121-136. doi:10.1007/s00018-012-1061-y

48. Ferree A, Guillily M, Li H, et al. Regulation of physiologic actions of LRRK2: focus on autophagy. *Neurodegener Dis*. 2012;10(1-4):238-241. doi:10.1159/000332599

49. Ramonet D, Daher JPL, Lin BM, et al. Dopaminergic Neuronal Loss, Reduced Neurite Complexity and Autophagic Abnormalities in Transgenic Mice Expressing G2019S Mutant LRRK2. *PLoS ONE*. 2011;6(4):e18568. doi:10.1371/journal.pone.0018568

50. Manzoni C, Mamais A, Dihanich S, et al. Pathogenic Parkinson's disease mutations across the functional domains of LRRK2 alter the autophagic/lysosomal response to starvation. *Biochem Biophys Res Commun*. 2013;441(4):862-866. doi:10.1016/j.bbrc.2013.10.159

51. Sánchez-Danés A, Richaud-Patin Y, Carballo-Carbajal I, et al. Disease-specific phenotypes in dopamine neurons from human iPS-based models of genetic and sporadic Parkinson's disease. *EMBO Mol Med*. 2012;4(5):380-395. doi:10.1002/emmm.201200215

52. Wauters F, Cornelissen T, Imberechts D, et al. LRRK2 mutations impair depolarization-induced mitophagy through inhibition of mitochondrial accumulation of RAB10. *Autophagy*. Published online April 4, 2019. doi:10.1080/15548627.2019.1603548

53. Manzoni C. The LRRK2-macroautophagy axis and its relevance to Parkinson's disease. *Biochem Soc Trans*. 2017;45(1):155-162. doi:10.1042/BST20160265

54. Bang Y, Kim K-S, Seol W, Choi HJ. LRRK2 interferes with aggresome formation for autophagic clearance. *Mol Cell Neurosci*. 2016;75:71-80. doi:10.1016/j.mcn.2016.06.007

55. Guerreiro PS, Gerhardt E, Lopes da Fonseca T, Bähr M, Outeiro TF, Eckermann K. LRRK2 Promotes Tau Accumulation, Aggregation and Release. *Mol Neurobiol*. 2016;53(5):3124-3135. doi:10.1007/s12035-015-9209-z

56. Novello S, Arcuri L, Dovero S, et al. G2019S LRRK2 mutation facilitates α-synuclein neuropathology in aged mice. *Neurobiol Dis*. 2018;120:21-33. doi:10.1016/j.nbd.2018.08.018

57. Schapansky J, Khasnavis S, DeAndrade MP, et al. Familial knockin mutation of LRRK2 causes lysosomal dysfunction and accumulation of endogenous insoluble α-synuclein in neurons. *Neurobiol Dis*. 2018;111:26-35. doi:10.1016/j.nbd.2017.12.005

58. Tenreiro S, Eckermann K, Outeiro TF. Protein phosphorylation in neurodegeneration: friend or foe? *Front Mol Neurosci*. 2014;7:42. doi:10.3389/fnmol.2014.00042

59. Anderson JP, Walker DE, Goldstein JM, et al. Phosphorylation of Ser-129 is the dominant pathological modification of alpha-synuclein in familial and sporadic Lewy body disease. *J Biol Chem*. 2006;281(40):29739-29752. doi:10.1074/jbc.M600933200

60. Kragh CL, Lund LB, Febbraro F, et al. Alpha-synuclein aggregation and Ser-129 phosphorylation-dependent cell death in oligodendroglial cells. *J Biol Chem*. 2009;284(15):10211-10222. doi:10.1074/jbc.M809671200

61. Wu B, Liu Q, Duan C, et al. Phosphorylation of α-synuclein upregulates tyrosine hydroxylase activity in MN9D cells. *Acta Histochem*. 2011;113(1):32-35. doi:10.1016/j.acthis.2009.07.007

62. Fiske M, Valtierra S, Solvang K, et al. Contribution of Alanine-76 and Serine Phosphorylation in α-Synuclein Membrane Association and Aggregation in Yeasts. *Parkinsons Dis*. 2011;2011:392180. doi:10.4061/2011/392180

63. Sancenon V, Lee S-A, Patrick C, et al. Suppression of α-synuclein toxicity and vesicle trafficking defects by phosphorylation at S129 in yeast depends on genetic context. *Hum Mol Genet*. 2012;21(11):2432-2449. doi:10.1093/hmg/dds058

64. Gonçalves S, Outeiro TF. Assessing the subcellular dynamics of alpha-synuclein using photoactivation microscopy. *Mol Neurobiol*. 2013;47(3):1081-1092. doi:10.1007/s12035-013-8406-x

65. Alonso AD, Cohen LS, Corbo C, et al. Hyperphosphorylation of Tau Associates With Changes in Its Function Beyond Microtubule Stability. *Front Cell Neurosci*. 2018;12:338. doi:10.3389/fncel.2018.00338

66. Bibow S, Ozenne V, Biernat J, Blackledge M, Mandelkow E, Zweckstetter M. Structural impact of proline-directed pseudophosphorylation at AT8, AT100, and PHF1 epitopes on 441-residue tau. *J Am Chem Soc*. 2011;133(40):15842-15845. doi:10.1021/ja205836j

67. Inoue M, Konno T, Tainaka K, Nakata E, Yoshida H-O, Morii T. Positional effects of phosphorylation on the stability and morphology of tau-related amyloid fibrils. *Biochemistry*. 2012;51(7):1396-1406. doi:10.1021/bi201451z

68. Whiteheart SW, Schraw T, Matveeva EA. N-ethylmaleimide sensitive factor (NSF) structure and function. *Int Rev Cytol*. 2001;207:71-112.

69. Naslavsky N, Stein R, Yanai A, Friedlander G, Taraboulos A. Characterization of detergent-insoluble complexes containing the cellular prion protein and its scrapie isoform. *J Biol Chem*. 1997;272(10):6324-6331.

70. Bjørkøy G, Lamark T, Brech A, et al. p62/SQSTM1 forms protein aggregates degraded by autophagy and has a protective effect on huntingtin-induced cell death. *J Cell Biol*. 2005;171(4):603-614. doi:10.1083/jcb.200507002

71. Simón-Sánchez J, Schulte C, Bras JM, et al. Genome-wide association study reveals genetic risk underlying Parkinson's disease. *Nat Genet*. 2009;41(12):1308-1312. doi:10.1038/ng.487

72. Liu X, Cheng R, Verbitsky M, et al. Genome-wide association study identifies candidate genes for Parkinson's disease in an Ashkenazi Jewish population. *BMC Med Genet*. 2011;12:104. doi:10.1186/1471-2350-12-104

73. Pankratz N, Beecham GW, DeStefano AL, et al. Meta-analysis of Parkinson's disease: identification of a novel locus, RIT2. *Ann Neurol*. 2012;71(3):370-384. doi:10.1002/ana.22687

74. Cheng W-W, Zhu Q, Zhang H-Y. Identifying Risk Genes and Interpreting Pathogenesis for Parkinson's Disease by a Multiomics Analysis. *Genes (Basel)*. 2020;11(9). doi:10.3390/genes11091100

75. Nalls M, C B, Cl V, et al. Identification of novel risk loci, causal insights, and heritable risk for Parkinson's disease: a meta-analysis of genome-wide association studies. The Lancet. Neurology. doi:10.1016/S1474-4422(19)30320-5

76. Pallanck L, Ordway RW, Ramaswami M, Chi WY, Krishnan KS, Ganetzky B. Distinct roles for N-ethylmaleimide-sensitive fusion protein (NSF) suggested by the identification of a second Drosophila NSF homolog. *J Biol Chem*. 1995;270(32):18742-18744.

77. Rothman JE. Mechanisms of intracellular protein transport. *Nature*. 1994;372(6501):55-63. doi:10.1038/372055a0

78. Malhotra V, Orci L, Glick BS, Block MR, Rothman JE. Role of an N-ethylmaleimide-sensitive transport component in promoting fusion of transport vesicles with cisternae of the Golgi stack. *Cell*. 1988;54(2):221-227.

79. Mohtashami M, Stewart BA, Boulianne GL, Trimble WS. Analysis of the mutant Drosophila N-ethylmaleimide sensitive fusion-1 protein in comatose reveals molecular correlates of the behavioural paralysis. *J Neurochem*. 2001;77(5):1407-1417.

80. Liu C, Hu B. Alterations of N-ethylmaleimide-sensitive atpase following transient cerebral ischemia. *Neuroscience*. 2004;128(4):767-774. doi:10.1016/j.neuroscience.2004.07.025

81. Longo F, Mercatelli D, Novello S, et al. Age-dependent dopamine transporter dysfunction and Serine129 phospho-α-synuclein overload in G2019S LRRK2 mice. *Acta Neuropathol Commun*. 2017;5(1):22. doi:10.1186/s40478-017-0426-8

82. Sloan M, Alegre-Abarrategui J, Potgieter D, et al. LRRK2 BAC transgenic rats develop progressive, L-DOPA-responsive motor impairment, and deficits in dopamine circuit function. *Hum Mol Genet*. 2016;25(5):951-963. doi:10.1093/hmg/ddv628

83. Sossi V, de la Fuente-Fernández R, Nandhagopal R, et al. Dopamine turnover increases in asymptomatic LRRK2 mutations carriers. *Movement Disorders*. 2010;25(16):2717-2723. doi:10.1002/mds.23356

84. Rubinsztein DC. The roles of intracellular protein-degradation pathways in neurodegeneration. *Nature*. 2006;443(7113):780-786. doi:10.1038/nature05291

85. Verhoef LGGC, Lindsten K, Masucci MG, Dantuma NP. Aggregate formation inhibits proteasomal degradation of polyglutamine proteins. *Hum Mol Genet*. 2002;11(22):2689-2700.

86. Hara T, Nakamura K, Matsui M, et al. Suppression of basal autophagy in neural cells causes neurodegenerative disease in mice. *Nature*. 2006;441(7095):885-889. doi:10.1038/nature04724

87. Komatsu M, Waguri S, Chiba T, et al. Loss of autophagy in the central nervous system causes neurodegeneration in mice. *Nature*. 2006;441(7095):880-884. doi:10.1038/nature04723

88. Del Roso A, Vittorini S, Cavallini G, et al. Ageing-related changes in the in vivo function of rat liver macroautophagy and proteolysis. *Exp Gerontol*. 2003;38(5):519-527.

89. Graham SH, Liu H. Life and death in the trash heap: The ubiquitin proteasome pathway and UCHL1 in brain aging, neurodegenerative disease and cerebral Ischemia. *Ageing Res Rev*. 2017;34:30-38. doi:10.1016/j.arr.2016.09.011

90. Martinez-Vicente M, Sovak G, Cuervo AM. Protein degradation and aging. *Exp Gerontol*. 2005;40(8-9):622-633. doi:10.1016/j.exger.2005.07.005

91. Ding X, Ren F. Leucine-rich repeat kinase 2 inhibitors: a patent review (2014-present). *Expert Opin Ther Pat*. 2020;30(4):275-286. doi:10.1080/13543776.2020.1729354

92. Baptista MAS, Dave KD, Frasier MA, et al. Loss of leucine-rich repeat kinase 2 (LRRK2) in rats leads to progressive abnormal phenotypes in peripheral organs. *PLoS ONE*. 2013;8(11):e80705. doi:10.1371/journal.pone.0080705

93. Fuji RN, Flagella M, Baca M, et al. Effect of selective LRRK2 kinase inhibition on nonhuman primate lung. *Sci Transl Med*. 2015;7(273):273ra15. doi:10.1126/scitranslmed.aaa3634

94. Herzig MC, Kolly C, Persohn E, et al. LRRK2 protein levels are determined by kinase function and are crucial for kidney and lung homeostasis in mice. *Hum Mol Genet*. 2011;20(21):4209-4223. doi:10.1093/hmg/ddr348

95. Ness D, Ren Z, Gardai S, et al. Leucine-rich repeat kinase 2 (LRRK2)-deficient rats exhibit renal tubule injury and perturbations in metabolic and immunological homeostasis. *PLoS ONE*. 2013;8(6):e66164. doi:10.1371/journal.pone.0066164

96. Tong Y, Yamaguchi H, Giaime E, et al. Loss of leucine-rich repeat kinase 2 causes impairment of protein degradation pathways, accumulation of alpha-synuclein, and apoptotic cell death in aged mice. *Proc Natl Acad Sci USA*. 2010;107(21):9879-9884. doi:10.1073/pnas.1004676107

97. Baptista MAS, Merchant K, Barrett T, et al. LRRK2 inhibitors induce reversible changes in nonhuman primate lungs without measurable pulmonary deficits. *Sci Transl Med*. 2020;12(540). doi:10.1126/scitranslmed.aav0820

98. Rodríguez-Navarro JA, Rodríguez L, Casarejos MJ, et al. Trehalose ameliorates dopaminergic and tau pathology in parkin deleted/tau overexpressing mice through autophagy activation. *Neurobiol Dis*. 2010;39(3):423-438. doi:10.1016/j.nbd.2010.05.014

99. Sarkar S, Davies JE, Huang Z, Tunnacliffe A, Rubinsztein DC. Trehalose, a novel mTOR-independent autophagy enhancer, accelerates the clearance of mutant huntingtin and alpha-synuclein. *J Biol Chem*. 2007;282(8):5641-5652. doi:10.1074/jbc.M609532200

100. Seki T, Abe-Seki N, Kikawada T, et al. Effect of trehalose on the properties of mutant {gamma}PKC, which causes spinocerebellar ataxia type 14, in neuronal cell lines and cultured Purkinje cells. *J Biol Chem*. 2010;285(43):33252-33264. doi:10.1074/jbc.M110.146704

101. Zaltzman R, Elyoseph Z, Lev N, Gordon CR. Trehalose in Machado-Joseph Disease: Safety, Tolerability, and Efficacy. *Cerebellum*. Published online June 9, 2020. doi:10.1007/s12311-020-01150-6

102. Halbe L, Rami A. Trehalase localization in the cerebral cortex, hippocampus and cerebellum of mouse brains. *J Adv Res*. 2019;18:71-79. doi:10.1016/j.jare.2019.01.009

103. Montalto M, Gallo A, Ojetti V, Gasbarrini A. Fructose, trehalose and sorbitol malabsorption. *Eur Rev Med Pharmacol Sci*. 2013;17 Suppl 2:26-29.

104. Collins J, Robinson C, Danhof H, et al. Dietary trehalose enhances virulence of epidemic Clostridium difficile. *Nature*. 2018;553(7688):291-294. doi:10.1038/nature25178

105. Ferri ALM, Cavallaro M, Braida D, et al. Sox2 deficiency causes neurodegeneration and impaired neurogenesis in the adult mouse brain. *Development*. 2004;131(15):3805-3819. doi:10.1242/dev.01204

106. Luong TN, Carlisle HJ, Southwell A, Patterson PH. Assessment of motor balance and coordination in mice using the balance beam. *J Vis Exp*. 2011;(49). doi:10.3791/2376

107. Hickey MA, Kosmalska A, Enayati J, et al. Extensive early motor and non-motor behavioral deficits are followed by striatal neuronal loss in knock-in Huntington's disease mice. *Neuroscience*. 2008;157(1):280-295. doi:10.1016/j.neuroscience.2008.08.041

108. Pan D, Sciascia A, Vorhees CV, Williams MT. Progression of multiple behavioral deficits with various ages of onset in a murine model of Hurler syndrome. *Brain Res*. 2008;1188:241-253. doi:10.1016/j.brainres.2007.10.036

109. Pischedda F, Piccoli G. The IgLON Family Member Negr1 Promotes Neuronal Arborization Acting as Soluble Factor via FGFR2. *Front Mol Neurosci*. 2015;8:89. doi:10.3389/fnmol.2015.00089

110. Pischedda F, Montani C, Obergasteiger J, et al. Cryopreservation of Primary Mouse Neurons: The Benefit of Neurostore Cryoprotective Medium. *Front Cell Neurosci*. 2018;12:81. doi:10.3389/fncel.2018.00081

111. Wiznerowicz M, Trono D. Conditional suppression of cellular genes: lentivirus vector-mediated drug-inducible RNA interference. *J Virol*. 2003;77(16):8957-8961.

112. Mosmann T. Rapid colorimetric assay for cellular growth and survival: application to proliferation and cytotoxicity assays. *J Immunol Methods*. 1983;65(1-2):55-63.

113. Reinhardt P, Glatza M, Hemmer K, et al. Derivation and expansion using only small molecules of human neural progenitors for neurodegenerative disease modeling. *PLoS ONE*. 2013;8(3):e59252. doi:10.1371/journal.pone.0059252

Table 1

cases	n° α–syn + LBs	n° NSF + LBs	% of LBs + for NSF
iPD 1	16	6	37
iPD2	22	8	36
iPD3	10	4	40
iPD4	18	4	22
G2019S1	15	5	33
G2019S2	12	3	25

The table lists the number of α-synuclein positive structure (α-syn +), the number of α-synuclein and NSF positive structure (NSF +) and the relative percentage (%) in specimens prepared from substantia nigra region of 4 idiopathic (iPD) and 2 G2019S patients

Figure legends

Figure 1. hG2019S mice show age-dependent motor and cognitive impairment. Wild-type and hG2019S mice were profiled for motor and cognitive abilities at 3, 6, 12, and 18 months. 6 and 12 months-old hG2019S mice are characterized by impaired motor coordination and cognitive performance. In detail, we measured spontaneous motor activity in terms of the number of

horizontal (A) and vertical (B) counts in 3 hours, time to cross a 6-mm width beam (C), time to reach the ground from the top of a vertical wire-mesh pole (D), time spent on a rotarod running at 12 rpm (E) or 32 rpm (F), total resistance on a 12 rpm running rotarod (G), and ability to recognize novel object compared to the familiar one (H); n=7-18, * $p<0.05$, ** $p<0.01$, *** $p<0.001$,**** $p<0.0001$ versus aged-matched wild-type.

Figure 2. NSF aggregation in hG2019S mice. NSF accumulates in perinuclear aggregates decorated by LC-3 (A) and p62 (B) in DIV14 cortical neurons prepared from hG2019S mice. Images are shown in pseudocolor (NSF~~G~~ green, LC-3~~,~~ and p62 red, DAPI blue). Scale bar= 10µm. Brain samples ~~DIV14 cortical cultures~~ from 6 months old wild-type or hG2019S mice were assayed by filter retardation assay to isolate the high-molecular-weight form of NSF (HMW) or by dot-blot to measure total NSF protein (C). The graph~~s~~ reports NSF aggregation expressed as HMW fold-over total NSF; n=8,~~. Data are shown as mean ±SEM, n=8.~~ * $p<0.05$ versus wild-type (D). The biochemical analysis of brain homogenate shows that NSF is resistant to proteinase K degradation in samples prepared from of 6-months old hG2019S mice. The a~~A~~rrowhead indicates the band corresponding to full-length NSF (E). -The graph indicates~~s report~~ the amount of full-length NSF protein expressed as optical density after digestion with 0.5 µg/ml proteinase K; n=8,~~. Data are shown as mean ±SEM, n=8.~~ * $p<0.05$ versus wild-type (F).~~-~~ NSF accumulates in aggregates in substantia nigra and striatum (G) as well as in cortex and hippocampus (H) in 6-months hG2019S LRRK2 mice. Scale bar= 10µm.

Figure 3. NSF aggregation in human-derived samples. NSF distribution in the TBS~~Triton-X100~~ (A) or SDS (B) soluble fraction in PD specimens. The g~~G~~raphs report~~s~~ NSF optical density in the TBS~~Triton-X100~~ (C) or SDS (D) soluble fraction, normalized versus actin amount; n~~. Data are shown as mean ±SEM, n~~=4-5,~~.~~ * $p<0.05$ versus control. Post-mortem analysis of nigra specimens shows that NSF decorates α-synuclein positive Lewy bodies and Lewy neurite in G2019S PD patients. Scale bar= 10µm (E). Induced dopaminergic neurons differentiated from two independent G2019S patients (G2019S 1 and 2) as well as gene-corrected counterpart (GC 1 and 2) were assayed by filter retardation assay to isolate high-molecular-weight form of NSF (HMW) or by dot-blot to measure total NSF protein (total) (F). The graph~~s~~ reports NSF aggregation expressed as HMW fold-over total NSF; n=8,~~. Data are shown as mean ±SEM, n=8.~~ ** $p<0.001$ versus wild-type (G).

Figure 4. LRRK2 phosphorylation induces NSF aggregation. NSF is phosphorylated at Thr645 in G2019S PD-patients brains (A). The graphs report NSF phosphorylation at Thr645 fold-over total NSF (B) as well as NSF relative amount (C); n=4-5, * $p<0.05$. NSF is phosphorylated at Thr645 in hG2019S mice brain (D). The graph reports NSF phosphorylation at Thr645 fold-over total NSF; n=8, *, ** $p<0.05$, 0.01 versus wild-type (E). The combined ribbon, stick, and sphere representation showing the overall architecture of NSF hexamer structure from human (PDB ID: 3J94) as well as the positions of T645 and two bound ATP molecules in one NSF monomer. In this drawing, the six NSF monomers are shown in different colours, and the side chain of T645 is shown in the sphere mode and the bound ATP in the stick mode. The missing region between residue 456 and 479 in the NSF monomer is represented by a dashed pink line (F). The enlarged view of an NSF monomer (in blue) shows that the side chain of T645 is very close to the bound ATP molecule on the D2 domain (G). LRRK2 phosphorylation influences NSF aggregation. We assayed the solubility profile of NSF in samples prepared from DIV14 wild-type or hG2019S cortical neurons and treated with vehicle (DMSO) or the LRRK2 kinase inhibitor GSK2578215A (GSK, 0.2 μM, 18 hours). Short and long acquisition time of the ECL signal emitted by anti-NSF western-blot is reported (H). The graph reports the amount of NSF present in the Triton-X100 insoluble fraction, expressed as fold-over total NSF; n=11, ** $p<0.01$ versus wild-type DMSO (I). We assayed the solubility profile of FLAG- and HA-NSF in samples prepared from HEK293 cell over-expressing wild-type or phosphomimetic T645D Strep-FLAG-NSF isoform together with HA-NSF wild-type. Strep-FLAG NSF T465D is present in the Triton-X100 insoluble fraction and sequesters HA-NSF wild-type (J). The graphs report the amount of FLAG-NSF (K) and HA-NSF (L) present in the Triton-X100 insoluble fraction, expressed as fold-over total NSF; n=8-14, * $p<0.05$, *** $p<0.001$ versus wild-type. We transfected in HEK293 cells myc-ubiquitin together with Strep-FLAG-NSF WT or T645D. We purified on streptavidin-beads NSF protein and assessed ubiquitination level by western-blotting with anti-myc antibody. The arrowheads indicate putative NSF low molecular weight fragments detected by the anti-FLAG antibody (M). The graphs report NSF ubiquitination in presence of myc-ubiquitin wild-type, calculated as anti-myc optical density normalized versus total NSF yield (N) and NSF fragmentation, expressed as the ratio of low molecular weight NSF fragments over high molecular weight NSF optical density (O); n=7, ** $p<0.01$ versus wild-type.

Figure 5. LRRK2 phosphorylation triggers NSF toxicity. Representative images of DIV14 wild-type and hG2019S cortical neurons transduced at DIV4 with mCherry expressing viruses (control) or viruses co-expressing mCherry and wild-type Strep-FLAG NSF WT, phospho-null variant

T645A or phospho-mimetic variant T645D. Where indicated, cells were treated from DIV10 to DIV14 with DMSO or GSK2578215A (GSK, 0.2 μM, every two days); scale bar= 40um (A). The graph reports the number of neurites per neuron; n=14, *** $p<0.001$ versus NSF WT in wild-type neuron, °°° $p<0.001$ versus control infection in wild-type neuron, ## $p<0.01$ versus NSF WT in hG2019S neurons DMSO (B). Neuronal cultures were infected and treated as above and then processed for MTT assay at DIV14. The graph reports toxicity, calculated as 100- relative absorbance, where 100 is the mean MTT absorbance measured in not treated wild-type neurons (control) and the relative absorbance is the MTT absorbance measured in each culture folded over the control (C); n=18, ** $p<0.01$ versus NSF WT in wild-type neurons, # $p<0.01$ versus NSF WT in wild-type neurons DMSO,°° $p<0.001$ versus control infection in wild-type neuron.

Figure 6. Trehalose treatment rescues histochemical pathological hallmark of hG2019S mice in the substantia nigra. Representative micrographs of nigra sections from 6 months old wild-type and hG2019S mice treated with trehalose for 1 month, stained with anti-NSF, anti-TH, and anti-cleaved caspase-3 antibodies and counterstained with hematoxylin to visualize nuclei, scale bar = 50 μm (A). The graphs report the number of NSF aggregates (B), the TH optical density (C), and the number of caspase-3 positive cells (D) detected in a 0.1 mm^2 area; n=6, *** $p<0.001$ versus wild-type, same treatment, $$$ $p<0.001$ versus water, same genotype.

Figure 7. Trehalose treatment rescues the histochemical pathological hallmark of hG2019S mice in the striatum. Representative micrographs of striatal sections from 6 months old wild-type and hG2019S mice treated with trehalose for 1 month, stained with anti-NSF, anti-TH, and anti-cleaved caspase-3 antibodies and counterstained with hematoxylin to visualize nuclei, scale bar = 50 μm (A). The graphs report the number of NSF aggregates (B), the TH optical density (C) and the number of caspase-3 positive cells (D) detected in a 0.1 mm^2 area; n=6, *** $p<0.001$ versus wild-type, same treatment, $$$ $p<0.001$ versus water, same genotype.

Figure 8. Trehalose treatment rescues motor and cognitive defects of hG2019S mice. Wild-type and hG2019S mice were treated starting at 5 months with trehalose (1% in drinking water) and profiled for motor and cognitive abilities at 6 months. In detail, we measured spontaneous motor activity in terms of the number of horizontal (A) and vertical (B) counts in 3 hours, time to cross a 12- and 6-mm width beam (C), time to reach the ground from the top of a vertical wire-mesh pole (D), time spent on a rotarod running at 12 rpm (E) or 32 rpm (F), total resistance on a 12 rpm

running rotarod (G), and ability to recognize novel object compared to the familiar one (H); n=7-18, * $p<0.05$, ** $p<0.01$, *** $p<0.001$, **** $p<0.0001$ versus wild-type, same treatment, $ $p<0.05$, $$ $p<0.01$, $$$ $p<0.001$ versus water, same genotype.

Supplementary figure 1. hG2019S mice present proteinaceous aggregates. Wild-type and hG2019S mice were processed for imaging analysis at 6 months. Brain sections were stained with anti-LC-3 antibody and counterstained with hematoxylin to visualize nuclei. Scale bars = 50µm. We reported a peculiar LC3-immunoreactivity in the nigra, cortex, and hippocampus specimen prepared from hG2019S mice brain. The insets highlight differences in LC3 immunoreactivity in neurons (2X higher magnification). We noticed intense LC3 staining surrounding *bona fide* pale bodies (indicated by the asterisk) in nigra (e-f), striatum (k-l), cortex (q-r), and hippocampus (w-x).

Supplementary figure 2. Wild-type and hG2019S mice were processed for imaging analysis at 6 months. Brain sections were stained with anti alpha-synuclein antibody and counterstained with hematoxylin to visualize nuclei. Scale bars= 50µm.

Supplementary figure 3. We performed a biochemical analysis of cortical (Cx), hippocampal (Hi), and striatal (St) samples harvested from 6 months old wild-type and hG2019S mice brains (A). The graphs report LRRK2 phosphorylation at Ser935 fold-over total LRRK2 (B), relative LRRK2 (C), and relative NSF (D) amount; n=8. We performed a western-blot analysis to profile the maturation of G2019S or gene-corrected neural precursor cell to dopaminergic neurons. Anti-nestin antibody stains immature proliferating cells while TH mature DA-neurons. I: expansion media; II: ventral CNS neuron differentiation medium; III maturation medium; IV: differentiation medium (E). Immunofluorescence characterization of terminally differentiated NPC shows the expression of β-III-tubulin, synapsin I, and TH proteins. Scale bars = 10µm (F).

Supplementary figure 4. Wild-type and hG2019S mice were processed for imaging analysis at 12 months. Brain sections were stained with anti-NSF antibody and counterstained with hematoxylin to visualize nuclei. Scale bars = 50µm (A). We performed a biochemical analysis of brain samples harvested from 12 months old wild-type and hG2019S mice (B). The graphs report relative LRRK2 (C), and relative NSF (D) amount; n=4-6. We assessed by filter retardation assay NSF aggregation in brain specimens prepared from 12-months wild-type and hG2019S mice (E). The graph reports NSF aggregation expressed as the ratio of HMW over total NSF optical density; n=18, * $p<0.05$ versus wild-type (F). The biochemical analysis of brain homogenate shows NSF resistance to proteinase K degradation in samples prepared from of 12-months old wild-type and hG2019S mice. The arrowhead indicates the band corresponding to full-length NSF (G). The graph reports the amount of full-length NSF protein expressed as optical density after digestion with 0.5 µg/ml proteinase K; n=6 (H).

Supplementary figure 5. Validation of a polyclonal anti-P-Thr645 NSF antibody. HEK293 cells were transfected with LRRK2-G2019S and FLAG-tagged wild-type NSF protein. 48h post-transfection cells were treated with increasing doses of MLi-2 for 4 hours, then lysed and analyzed (40µg of proteins) by immunoblotting (A). HEK293 cells were transfected with FLAG-tagged wild-type NSF protein or NSF T645A or the phosphomimetics NSF T645E and T645D variant together with GFP or LRRK2-G2019S. Upon solubilization, lysates (40µg of proteins) were subjected to immunoblotting. Affinity-purified anti- P-Thr645-NSF was used for immunoblot at 1:1000 dilution (in 3% BSA in TBS-T), and in the presence of an excess (5X) of non-phosphorylated peptide antigen (KKAPPQGRKLLIIGTTSRKDVLQEME) (B). LRRK2 phosphorylation influences NSF aggregation. We assayed the solubility profile of NSF in samples prepared from N2A cell over-expressing LRRK2 K1906M or LRRK2 G2019S variants and treated with vehicle (DMSO) or the LRRK2 kinase inhibitor GSK2578215A (GSK, 2 µM, 18 hours) (C). The graph reports the amount of NSF present in the Triton-X100 insoluble fraction, expressed as fold-over total NSF; n=7, ** $p<0.01$ versus wild-type, same treatment; # $p<0.05$ versus G2019S DMSO (D). We assayed the solubility profile of NSF in samples prepared from HEK293 cell over-expressing NSF wild-type or T645A variant together with either LRRK2 K1906M or LRRK2 G2019S variants (E). The graph reports the amount of NSF present in the Triton-X100 insoluble fraction, expressed as fold-over LRRK2 K1906M condition; n=9, ** $p<0.01$ versus LRRK2 K1906M (F). NSF aggregates in hG2019S cellular models independently from the proteasome activity. Wild-type and hG2019S DIV14 cortical neurons were treated with 100nM MG-132 or vehicle (DMSO) for 48 hours and then assayed by filter retardation assay to isolate high molecular weight (HMW) form of NSF or by dot-blot to measure total NSF protein. NSF appears in HMW aggregates in wild-type neurons upon proteasome impairment and in vehicle-treated hG2019S neurons (G). The graph reports NSF aggregation expressed as HMW fold-over total NSF; n=8, *** p<0.001 versus wild-type, same treatment, ## p<0.01 versus DMSO, same genotype (H). We analyzed 20S proteasome activity in brain samples prepared from 6- or 12-months old mice. The graph reports relative fluorescence at 520-530 nm, n= 4 (I).

Supplementary figure 6. Inorganic phosphate (Pi) generated by ATP hydrolysis in the presence of NSF wild-type and T645D mutant was measured with the Malachite Green Assay at 120 min; n=3, ** p<0.01 Student T-test (A). Kinetic constants were obtained by data fitting with the Michaelis-Menten kinetic model Y = Vmax*S/(Km + [S]). Vmax NSF wild-type=3.6 µmol/min NSF T645D=4 µmol/min; Km NSF wild-type=188 µM Km NSF T645D=180 µM. Extra sum-of-squares F test was used for statistical analysis; n=3, *** p<0.001 (B). We analyzed HEK293 cell over-expressing Strep-FLAG-NSF wild-type or phosphomimetic T645D isoform and treated with vehicle (DMSO) or MG-132 (10 µM, 18 hours) by filter retardation assay to isolate high molecular weight (HMW) form of NSF or by dot-blot to measure total NSF protein (C). The graph reports NSF aggregation expressed as the ratio of HMW over total NSF optical density; n=5, ** p<0.01 versus wild-type, same treatment (D). Size exclusion chromatography fractions of HEK293 expressing ectopic Strep-FLAG-NSF wild-type or T645D alone spotted onto nitrocellulose membrane and probed with anti-flag antibody. Theoretical molecular weight are V0 at fraction 8.5, 669kDa at fraction 12, 449kDa at fraction 13 (E). The graph reports the intensity of each dot (fraction) normalized by the integrated intensities. The column void volume is 7.5 ml, n=3 (F). We transfected myc-ubiquitin wild-type, K48R, K63R, or K29/48/63 R together with Strep-FLAG-NSF WT or T645D in HEK293 cells. We purified on streptavidin-beads NSF protein and assessed ubiquitination level by western-blotting with anti-myc antibody. The arrowheads indicate putative NSF low molecular weight fragments detected by anti-FLAG antibody (G). The graphs H, J report NSF ubiquitination calculated as anti-myc optical density normalized versus total NSF wild-type (H) or T645D (J) yield and expressed as fold-over ubiquitin wild-type condition. The graphs I, K show NSF fragmentation, expressed as the ratio of low molecular weight NSF fragments over high molecular weight NSF wild-type (I) or T645D (K) optical density and folded over ubiquitin wild-type condition; n=7, * p<0.05, ** p<0.01 versus ubiquitin wild-type, one-sample T-test.

Supplementary figure 7. Wild-type and hG2019S cortical neurons were infected at DIV4 with mCherry expressing viruses or viruses co-expressing mCherry and wild-type Strep-FLAG NSF (NSF WT) or Thr645Ala Strep-FLAG NSF (NSF T645A). Cells were treated from DIV10 to DIV14 with DMSO or GSK2578215A (0.2 µM, every two days). Cells were then solubilized and processed for western-blotting to assess ectopic NSF expression, LRRK2 phosphorylation, and total LRRK2 level.

Supplementary figure 8. We evaluated basal autophagy in samples prepared from 6 months old wild-type and hG2019S mice brain (A). The graphs report LC3II/actin (left) and LC3II/LC3I ratio (right); n=5 (B). We treated DIV13 wild-type and hG2019S cortical neurons with vehicle (water) or trehalose (100 mM, 1 day) alone or in combination with NH4Cl (5mM, 2 hours) and then processed for western blotting to evaluate the induction of autophagy, indicated by the appearance of LC3II band (C). The graph reports the LC3II/LC3I ratio; n=8, *** $p<0.001$ versus water (D). We assayed HEK293 cells over-expressing NSF wild-type and treated with vehicle (DMSO) or MG-132 (10 µM, 18 hours) alone or in combination with trehalose (100 mM, 18 hours). We measured the presence of NSF in high molecular weight aggregates (HMW) by filter retardation assay as well as total NSF expression (total) via dot-blot on a nitrocellulose membrane (E). The graph reports NSF aggregation expressed as ratio of HMW over total NSF optical density; n=8, ** $p<0.01$ versus DMSO, # $p<0.05$ versus control treatment (F). We assessed by filter retardation assay NSF aggregation in brain specimens prepared from 6-month wild-type and hG2019S mice treated with trehalose (1% in drinking water, 1 month). Trehalose treatment reduces HMW NSF forms in cortical specimens obtained from 6 months mice (G). The graph reports NSF aggregation expressed as the ratio of HMW over total NSF optical density; n=6, * $p<0.05$ versus wild-type, same treatment, ## $p<0.01$ versus water, same genotype (H). Trehalose treatment did not influence mice weight. The graph reports mice weight along with the 4 weeks treatment, n=10 (I).

Supplementary figure 9. Trehalose treatment rescues the histochemical pathological hallmark of hG2019S mice in the cortex and hippocampus. Wild-type and hG2019S mice were treated starting at 5 months with trehalose (1% in drinking water) and processed for imaging analysis at 6 months. Brain sections encompassing cortical area or hippocampus were stained with anti-NSF and anti-cleaved caspase-3 antibodies and counterstained with hematoxylin to visualize nuclei. hG2019S mice are characterized by NSF aggregation and caspase-3 cleavage in the cortex and hippocampus. Trehalose treatment reduced NSF aggregation and cleaved-caspase 3 signal (A). The graphs report number of NSF aggregates in cortex (B) and hippocampus (D) as well as the number of caspase-3 positive cells in cortex (C) and hippocampus (E) detected in a 0.1 mm^2 area; n=5, *$p<0.05$, *** $p<0.001$ versus wild-type, same treatment, $$$ $p<0.001$ versus water, same genotype.

Supplementary figure 10. Wild-type and hG2019S mice were treated starting at 10 months with trehalose (1% in drinking water) and profiled for motor and cognitive abilities at 12 months. In detail, we measured spontaneous motor activity in terms of the number of horizontal (A) and vertical (B) counts in 3 hours, time to cross a 6-mm or 12-mm width beam (C), time to reach the ground from the top of a vertical wire-mesh pole (D), time spent on rotarod running at 12 rpm (E) or 32 rpm (F), total resistance on 12 rpm running rotarod (G) and ability to recognize a novel object (H); n=7-18, * $p<0.05$, ** $p<0.01$, *** $p<0.001$,**** $p<0.0001$ versus wild-type, same treatment, \$ $p<0.05$, \$\$\$ $p<0.001$ versus water, same genotype.

ARRIVE

The ARRIVE Guidelines Checklist

Animal Research: Reporting In Vivo Experiments

Carol Kilkenny[1], William J Browne[2], Innes C Cuthill[3], Michael Emerson[4] and Douglas G Altman[5]

[1]The National Centre for the Replacement, Refinement and Reduction of Animals in Research, London, UK, [2]School of Veterinary Science, University of Bristol, Bristol, UK, [3]School of Biological Sciences, University of Bristol, Bristol, UK, [4]National Heart and Lung Institute, Imperial College London, UK, [5]Centre for Statistics in Medicine, University of Oxford, Oxford, UK.

	ITEM	RECOMMENDATION	Section/ Paragraph
Title	1	Provide as accurate and concise a description of the content of the article as possible.	page 1
Abstract	2	Provide an accurate summary of the background, research objectives, including details of the species or strain of animal used, key methods, principal findings and conclusions of the study.	summary
INTRODUCTION			
Background	3	a. Include sufficient scientific background (including relevant references to previous work) to understand the motivation and context for the study, and explain the experimental approach and rationale. b. Explain how and why the animal species and model being used can address the scientific objectives and, where appropriate, the study's relevance to human biology.	introduction
Objectives	4	Clearly describe the primary and any secondary objectives of the study, or specific hypotheses being tested.	introduction
METHODS			
Ethical statement	5	Indicate the nature of the ethical review permissions, relevant licences (e.g. Animal [Scientific Procedures] Act 1986), and national or institutional guidelines for the care and use of animals, that cover the research.	experimental procedures/
Study design	6	For each experiment, give brief details of the study design including: a. The number of experimental and control groups. b. Any steps taken to minimise the effects of subjective bias when allocating animals to treatment (e.g. randomisation procedure) and when assessing results (e.g. if done, describe who was blinded and when). c. The experimental unit (e.g. a single animal, group or cage of animals). A time-line diagram or flow chart can be useful to illustrate how complex study designs were carried out.	experimental procedures/ Behavioural tests
Experimental procedures	7	For each experiment and each experimental group, including controls, provide precise details of all procedures carried out. For example: a. How (e.g. drug formulation and dose, site and route of administration, anaesthesia and analgesia used [including monitoring], surgical procedure, method of euthanasia). Provide details of any specialist equipment used, including supplier(s). b. When (e.g. time of day). c. Where (e.g. home cage, laboratory, water maze). d. Why (e.g. rationale for choice of specific anaesthetic, route of administration, drug dose used).	experimental procedures/ Behavioural tests
Experimental animals	8	a. Provide details of the animals used, including species, strain, sex, developmental stage (e.g. mean or median age plus age range) and weight (e.g. mean or median weight plus weight range). b. Provide further relevant information such as the source of animals, international strain nomenclature, genetic modification status (e.g. knock-out or transgenic), genotype, health/immune status, drug or test naïve, previous procedures, etc.	experimental procedures/ animals

The ARRIVE guidelines. Originally published in *PLoS Biology*, June 2010[1]

Housing and husbandry	9	Provide details of: a. Housing (type of facility e.g. specific pathogen free [SPF]; type of cage or housing; bedding material; number of cage companions; tank shape and material etc. for fish). b. Husbandry conditions (e.g. breeding programme, light/dark cycle, temperature, quality of water etc for fish, type of food, access to food and water, environmental enrichment). c. Welfare-related assessments and interventions that were carried out prior to, during, or after the experiment.	experimental procedures/ animals
Sample size	10	a. Specify the total number of animals used in each experiment, and the number of animals in each experimental group. b. Explain how the number of animals was arrived at. Provide details of any sample size calculation used. c. Indicate the number of independent replications of each experiment, if relevant.	Figures legend
Allocating animals to experimental groups	11	a. Give full details of how animals were allocated to experimental groups, including randomisation or matching if done. b. Describe the order in which the animals in the different experimental groups were treated and assessed.	experimental procedures/ Behavioural tests
Experimental outcomes	12	Clearly define the primary and secondary experimental outcomes assessed (e.g. cell death, molecular markers, behavioural changes).	experimental procedures/
Statistical methods	13	a. Provide details of the statistical methods used for each analysis. b. Specify the unit of analysis for each dataset (e.g. single animal, group of animals, single neuron). c. Describe any methods used to assess whether the data met the assumptions of the statistical approach.	experimental procedures/Statistical analysis and guidelines
RESULTS			
Baseline data	14	For each experimental group, report relevant characteristics and health status of animals (e.g. weight, microbiological status, and drug or test naïve) prior to treatment or testing. (This information can often be tabulated).	supplementary figure 6
Numbers analysed	15	a. Report the number of animals in each group included in each analysis. Report absolute numbers (e.g. 10/20, not 50%[2]). b. If any animals or data were not included in the analysis, explain why.	Figures legend
Outcomes and estimation	16	Report the results for each analysis carried out, with a measure of precision (e.g. standard error or confidence interval).	Figures legend
Adverse events	17	a. Give details of all important adverse events in each experimental group. b. Describe any modifications to the experimental protocols made to reduce adverse events.	n.a.
DISCUSSION			
Interpretation/ scientific implications	18	a. Interpret the results, taking into account the study objectives and hypotheses, current theory and other relevant studies in the literature. b. Comment on the study limitations including any potential sources of bias, any limitations of the animal model, and the imprecision associated with the results[2]. c. Describe any implications of your experimental methods or findings for the replacement, refinement or reduction (the 3Rs) of the use of animals in research.	Discussion
Generalisability/ translation	19	Comment on whether, and how, the findings of this study are likely to translate to other species or systems, including any relevance to human biology.	Discussion
Funding	20	List all funding sources (including grant number) and the role of the funder(s) in the study.	Acknowledgments

References:
1. Kilkenny C, Browne WJ, Cuthill IC, Emerson M, Altman DG (2010) Improving Bioscience Research Reporting: The ARRIVE Guidelines for Reporting Animal Research. *PLoS Biol* 8(6): e1000412. doi:10.1371/journal.pbio.1000412
2. Schulz KF, Altman DG, Moher D, the CONSORT Group (2010) CONSORT 2010 Statement: updated guidelines for reporting parallel group randomised trials. *BMJ* 340:c332.

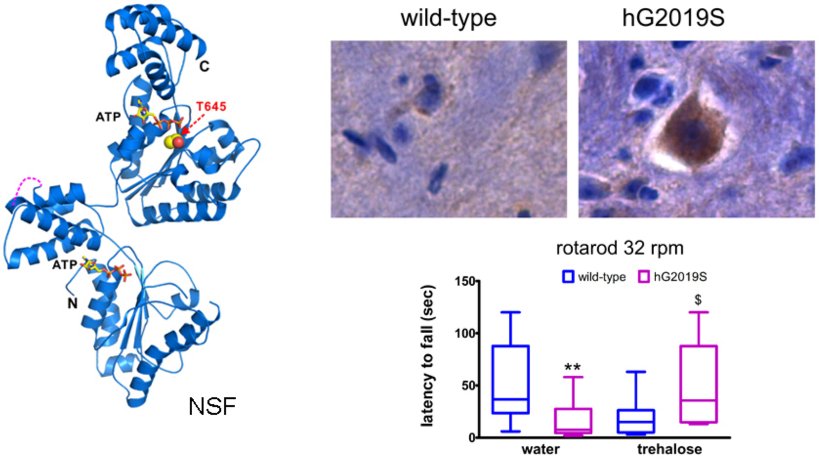

LRRK2 phosphorylation of Thr645 triggers the detrimental aggregation of NSF that can be cleared by the induction of autophagy

86x43mm (300 x 300 DPI)